

Manuscript Number: EGY-D-16-04245R2

Title: Darrieus Wind Turbine Blade Unsteady Aerodynamics: a Three-Dimensional Navier-Stokes CFD assessment

Article Type: Full length article

Keywords: Darrieus wind turbine, unsteady Navier-Stokes simulations, CFD, tip flows

Corresponding Author: Dr. Lorenzo Ferrari, Ph.D.

Corresponding Author's Institution: University of Pisa

First Author: Francesco Balduzzi

Order of Authors: Francesco Balduzzi; Jernej Drofelnik; Alessandro Bianchini; Giovanni Ferrara; Lorenzo Ferrari, Ph.D.; Michele S Campobasso

Abstract: Thanks to the recent rapid progress in high-performance computing and the growing availability of large computational resources, computational fluid dynamics now offers a cost-effective, versatile and accurate means to improve the understanding of the unsteady aerodynamics of Darrieus wind turbines, increase their efficiency and delivering more cost-effective structurally sound designs.

In this study, a Navier-Stokes CFD research code featuring a very high parallel efficiency was used to thoroughly investigate the three-dimensional unsteady aerodynamics of a one-blade Darrieus rotor. Highly spatially and temporally refined time-dependent simulations were carried out using up to 16,000 processor cores per simulation on an IBM BG/Q cluster. The study aims at providing a detailed description and quantification of the main three-dimensional effects associated with the cyclical motion of this turbine type, including tip losses, dynamic stall, vortex propagation and blade/wake interaction. On one hand, the results corroborate the findings of several carefully designed two-dimensional studies. On the other hand, they reveal that the three-dimensional flow effects affecting Darrieus rotor blades are much more complex than assumed by the conventional lower-fidelity models often used for design applications, and strongly vary during the rotor revolution.

Florence, September 20th 2016

Dear Prof. Lund,

new computational resources are thought to provide in the near future an essential contribution to an inner comprehension of complex phenomena taking place in a flow past rotating blades. As confirmed by some very interesting papers appeared in “Energy” in the last few years (all cited in the paper), particular interest is arising around Darrieus turbines due to the potential benefits of CFD in more accurately characterize some critical issues, e.g. the dynamic stall of the airfoils and aero-acoustic emissions.

In the past few years, thanks to the growth of available computational resources, 3D Navier-Stokes CFD analyses have received increasing attention, and some preliminary studies have been published. If many 2D studies showed that the minimum temporal and spatial refinement levels required to obtain grid-independent solutions is quite high, due to the aerodynamic complexity of these unsteady rotor flows, the computational cost of the simulation becomes very large when using 3D unsteady NS CFD for Darrieus rotor aerodynamics. As a result, almost all the studies presently published in the literature were constrained by limited computational resources to use of fairly coarse spatial and temporal refinements, which often did not match the requirements indicated by proper sensitivity analyses. In particular, the common approach found in the literature was to progressively coarsen the meshes when moving to 3D analyses, in order to limit the total number of cells in the range between 1,000,000 and 10,000,000.

In this study, unique simulations were run on an IBM BG/Q cluster. Thanks to the excellent parallel efficiency of the COSA code, the simulations yielding the results presented in this paper could be performed using about 16,000 cores. This required partitioning the 55,000,000 elements grid into 16384 blocks, making use of in-house utilities. Using a time-discretization of 720 steps per revolution, the simulation needed 12 revolutions to achieve a fully periodic state. The wall-clock time required for the complete simulation was about 653 hours (27.2 days). The study aims at providing a detailed description and quantification of the main three-dimensional effects associated with the cyclical motion of this turbine type, including tip losses, dynamic stall, vortex propagation and blade/wake interaction. On one hand, the results corroborate the findings of several carefully designed two-dimensional studies. On the other hand, they reveal that the three-dimensional flow effects affecting Darrieus rotor blades are much more complex than assumed by the conventional lower-fidelity models often used for design applications, and strongly vary during the rotor revolution.

In this view, we believe that the work can be of interest for many readers and contribute in reinforcing the journal position as the main reference for these analyses.

We would be then very pleased if you could consider the paper for publication in “Energy”.

Looking forward to hearing from you, best regards.

*Francesco Balduzzi
Jernej Drojelnik
Alessandro Bianchini
Giovanni Ferrara
Lorenzo Ferrari
Michele Sergio Campobasso*

Florence, Pisa, Lancaster and Glasgow
06/03/2017

Dear Prof. The,

we would like to thank again the Reviewers for their comments which have enabled us to make additional improvements to the paper, and you for your coordination of the review process.

On the basis of the reviewer's comments, a complete revision of the work has been carried out.

Many parts of the paper have been rewritten and additional data, figures and references have been added, with particular attention to the presentation of the CFD approach and to the assessment of the proposed approach validity and prospects. A further revision of the English (both grammar and style) has also been carried out to improve clarity on. To enable reviewers to more easily track the alterations in response to their questions/comments, many of these linguistic corrections have not been highlighted in blue (especially in the discussion of main results), as they did not alter the main content of the affected sentences.

Like in the first revision, our comments and responses to reviewer's comments have been highlighted in blue both in this communication and in the revised version of the paper.

We really hope that these additional modifications could make the paper worth of publication in *Energy*.

Best regards,

Francesco Balduzzi, Jernej Drofelnik, Alessandro Bianchini, Giovanni Ferrara, Lorenzo Ferrari, Michele Sergio Campobasso

ooo ooo ooo

REVIEWER #1

The paper has large improvements comparing to the previous version. Most questions have been responded in a satisfactory manner.

We would like to thank the Reviewer for his/her positive comments about the work we did on the paper with respect to the first draft.

1, It is OK using a one-bladed case for theoretical investigation. However, I still has the same question. Is that worth to spend 10 times computational effort to gain about 3 percents of accuracy (Let's suppose the results using fine mesh are more accurate)? For practical applications, i.e., two-bladed or three bladed cases, the computational effort will go to 20 or 30 times. So, according to the comparisons in this paper, actually, I have different opinion to that of the authors. If only considering the aerodynamic force, I don't think such high resolution simulations contribut much. The authors are encougrated to explore the difference of the detailed flow structure further between fine and coarse mesh results, especially for the strong 3D effect.

BTW, if the authors really talk about the sensitivity of the grid. A much more detaied grid sensitivity studing is required. However, that is not included in the main scope of energy journal.

According to the Reviewer's comment, paragraph 2.4 was further extended. Two figures were added (new Fig. 5 and 6) to show the influence of the mesh refinement on the resolution of the 3D flow features.

2,Th authors claimed that the maximum torque locating at $\theta=88.5$ is due to the onset of the stall. More explanations and pictures are required to show that clearly.

Thanks to the Reviewer comment, we understood that some sentences in the paper were misleading. We stated that "the maximum torque in the upwind portion of the revolution is located at $\theta \approx 88.5^\circ$ " and "stall in the central blade portion starts shortly before $\theta=90^\circ$ ", but we never clarified when stall actually occurs. We

have added a figure (new Fig. 8) highlighting the onset of stall, and we have modified the text to avoid any further confusion. Please refer to lines 472-482 in the revised paper.

3, The last question is not closely related to this paper. What partitioning method is used in COSA? Does the original blocks generated using ICEM CFD have the same cell number?

The original ANSYS® ICEM® grid generator provided a mesh made of 4096 blocks, almost perfectly balanced in terms of number of cells. Then, the grid was further partitioned into 16384 blocks (1 block per processor) using an in-house utility. All grid blocks had then identical number of cells to optimize the load balance of the parallel simulation.

REVIEWER #2

The revised manuscript can be considered for publication in Energy pending the raised points below:

Major comments:

a. Abstract

From the phrase, 'A comparison of the CFD integral estimates and the results of a blade-element momentum code is also presented to highlight strengths and weaknesses of low-fidelity codes for Darrieus turbine design'. Numerical simulations are usually compared or validated by means of experimental measurements. In "Results" section, not a single comparison with experimental data is presented. This reviewer still finds this as a major omission.

The authors agree with the Reviewer about the additional benefits that could be ensured by the availability of experimental data. Unfortunately, no experimental tests are presently available for the 1-blade configuration. As discussed in the paper, however, previous 2D CFD studies were carried out on the 3-blade rotor (refs. [21] and [53]), which confirmed the suitability of the proposed numerical approach and also highlighted the most appropriate numerical settings (grid refinement, timestep size, etc.) to be used.

Regarding the results of the BEM analyses, the authors would like to underline that these were not intended to be used as a means for validating the CFD analysis. Conversely, the high-fidelity 3D CFD results served the purpose of pointing out the intrinsic limitations of low-fidelity methods, such as those arising from the use of simplified models to account for tip losses).

b. Introduction

Although the authors have referred a lot of articles on both 2D and 3D VAWT rotor simulations, but still the following articles are suggested to add:

1. M. D. Bausas and L. A. M. Danao, The aerodynamics of a camber-bladed vertical axis wind turbine in unsteady wind, Energy 93 (2015) 1155-1164
2. L.A. Danao, J. Edwards, O. Eboibi, R. Howell, A numerical investigation into the influence of unsteady wind on the performance and aerodynamics of a vertical axis wind turbine, Appl. Energy 116 (2014) 111-124
3. D.W. Wekesa, C. Wang, Y. Wei, W. Zhu, Experimental and numerical study of turbulence effect on aerodynamic performance of a small-scale vertical axis wind turbine. Journal of Wind Engineering and Industrial Aerodynamics Vol. 157, 2016, 1-14.

The authors thank the Reviewer for these interesting suggestions. The three references have been added in the paper.

c. Methodology

Consider collapsing sections 2, 3 and 4 into one section (like "Methodology") while keeping the subsections.

The authors were pleased to accept the suggestion of the Reviewer. The paper is now made of 4 sections: previous sections 2, 3, and 4 were collapsed in the new Section 2 "Numerical methodology".

In line 313-316, the authors indicate that "...the blade was attached at midchord." However, the blade is usually balanced at 1/4 of the chord (0.25c) from the leading edge so consideration of the moment is taken at that point.

The Reviewer is right about the general design guidelines about the blade-spoke connection point. In the present case, however, the blade was attached at mid-chord since the case study was derived from the rotor experimentally tested in the wind tunnel (full detail is available in ref. [24]).

The rationality of the boundary conditions should be explained. The flow flux is not constant at the inlet of the computational domain. And how is the turbulent intensity 5% of inlet flow defined?

Imposed boundary conditions at far-field were those often used for this type of simulations, i.e. constant velocity magnitude and direction on inflow patches of the far-field boundary and constant static pressure on outflow patches of the far-field boundary (the density is practically constant everywhere due to low speed of the application). The turbulence intensity is the ratio of the root-mean-square of the turbulent velocity fluctuations and the mean velocity, as customary in turbulent flow analyses. The value of 5% was used to account for the high-frequency low-amplitude turbulent fluctuations occurring in a fairly stable wind regime. The investigation of the effects of large wind fluctuations of an unsteady wind regime (of the type reported in the references cited by the Reviewer at Point b) was not carried out because this is not one of the objectives of this study. It is however a very interesting topic for future extensions of the research reported in this article.

A CFD code flow solver COSA is mentioned. However, additional description of the following should be provided:

- a. Computational domain (dimensions and similarity with wind tunnel section)
- b. Boundary conditions discretization method adopted to meshing
- c. Software used to meshing
- d. Number of cells, y^+ , k_s , dimension of first cell close to the wall, wall function.

All the details indicated by the Reviewer have been added and/or clarified in the revised version of the paper (accordingly highlighted in blue colored text).

Add one title subsection where the authors describe (e.g. title: "Numerical set-up"):

- a. numerical approach (RANS, URANS, LES)
- b. turbulence model
- c. numerical schemes for the equations
- d. time step size study
- e. algorithm solver
- f. CFD code (software)
- g. calculation resource/cost

All the details indicated by the Reviewer have been added and/or clarified in the revised version of the paper (accordingly highlighted in blue colored text).

The definition and justification of the objectives have been clearly indicated. However, numerical error analysis of the methodology is not presented. In addition, there's no mesh independence and time step size studies.

A section dedicated to the grid and timestep sensitivity analysis has been provided during the first revision of the paper. However, prompted by the Reviewers' comments, we have now further improved it including new data and figures (see new Section 2.4).

d. Results and discussion

From Figure 5, the 2D simulation results over-predicts the C_m compared to the 3D, yet the overall shape of the curves is maintained. Justify this using power coefficient CP curve and offer an explanation including comparison with the literature data mentioned in section 1.

As suggested by the Reviewer, we have further extended the discussion on the comparison between the 2D and 3D curves by adding comments related to similar analyses available in the reviewed literature.

The authors assert that due to the large burden associated with running the 3D time-dependent simulation, only a single operating condition was simulated, corresponding to a tip-speed ratio (TSR) of 3.3. This can hold true for the 3D case, but for the 2D case, different tip speed ratios can be incorporated and a power coefficient curve plotted and compared with literature data to check the suitability of the numerical model. And why the choice of tip speed ratio of 3.3? I thought the choice at lower tsr with converged solution would ensure convergence at higher tsr.

Unfortunately, no experimental tests/data are presently available for this 1-blade configuration that can be used to make a comparison with CFD simulations. As discussed in the paper, however, previous 2D CFD studies were carried out on the 3-blade rotor (refs. [26] and [53]), which confirmed the suitability of the proposed numerical approach and also discussed the choice of adequate numerical settings (grid refinement, timestep size, etc.) for this type of CFD analysis.

The comment of the Reviewer is, however, very appropriate and prompted us to introduce both a discussion on why we selected TSR=3.3, and a fairly reliable power curve of the 1-blade rotor (new Fig. 3) in order to visualize the position of the selected operating condition with respect to the point of peak power coefficient. Please refer to lines 369-381 in the revised paper.

Although the authors state that the results are in agreement with previous analyses of streamlines and pressure coefficient profiles, the discussion fails to relate the findings and observations to other relevant studies in the literature. As a result, there appears to be no discussion on the implication and limitation of the findings. A discussion should be added to explain the significance/implication of the Darrieus wind turbine single blade analysis in comparison to analyses in the literature.

As suggested by the Reviewer, a new paragraph has been added in the paper to relate the findings and observations to other relevant studies in the literature, with the aim of comparing the efficiency decrease in terms of reduction of equivalent blade height. Please refer to lines 53-543 in the revised paper. Moreover, additional comments were provided on the shift of the torque peak as a function of the span position. Please refer to lines 464-471 in the revised paper.

Minor comments:

i. In the highlights, change 16.000 to 16,000
Corrected.

ii. In highlight, remove a colon in bullet 4
Removed.

iii. In the entire manuscript, change "free stream" to "free-stream"
Changed.

iv. Consider changing the section titled "Results" to "Results and discussion"
Changed.

Highlights (for review)

- Analysis of the 3D unsteady aerodynamics of a Darrieus wind turbine blade in motion
- Highly spatially and temporally refined time-dependent simulations carried out with the COSA code
- One month calculation time on more than 16.000 processors on a IBM BG/Q cluster
- Detailed description of: tip losses, dynamic stall, vortex propagation and blade/wake interaction

Darrieus Wind Turbine Blade Unsteady Aerodynamics: a Three-Dimensional Navier-Stokes CFD assessment

Francesco Balduzzi¹, Jernej Drofelnik², Alessandro Bianchini¹, Giovanni Ferrara¹,
Lorenzo Ferrari^{3*}, Michele Sergio Campobasso⁴

¹ Department of Industrial Engineering, University of Florence - Via di Santa Marta 3, 50139, Firenze, Italy -
Tel. +39 055 275 8773 - Fax +39 055 275 8755 - balduzzi@vega.de.unifi.it

² School of Engineering, University of Glasgow - James Watt Building South, University Avenue, G12 8QQ
Glasgow, UK - Tel. +44 (0)141 330 2032 - j.drofelnik.1@research.gla.ac.uk

^{3*} Department of Energy, Systems, Territory and Construction Engineering, University of Pisa - Largo Lucio
Lazzarino, 56122, Pisa, Italy - Tel. +39 050 221 7132 - Fax +39 050 221 7333 - lorenzo.ferrari@unipi.it

⁴ Department of Engineering, Lancaster University - Gillow Avenue - LA1 4YW Lancaster, UK - Tel. +44
(0)1524 594673 - Fax +44 (0)1524 381707 - m.s.campobasso@lancaster.ac.uk

* = contact author

Abstract

Energized by the recent rapid progress in high-performance computing and the growing availability of large computational resources, computational fluid dynamics (CFD) is offering a cost-effective, versatile and accurate means to improve the understanding of the unsteady aerodynamics of Darrieus wind turbines, increase their efficiency and delivering more cost-effective and structurally sound designs.

In this study, a Navier-Stokes CFD research code featuring a very high parallel efficiency was used to thoroughly investigate the three-dimensional unsteady aerodynamics of a Darrieus rotor blade. Highly spatially and temporally resolved unsteady simulations were carried out using more than 16,000 processor cores on an IBM BG/Q cluster. The study aims at providing a detailed description and quantification of the main three-dimensional effects associated with the periodic motion of this turbine type, including tip losses, dynamic stall, vortex propagation and blade/wake interaction. Presented results reveal that the three-dimensional flow effects affecting Darrieus rotor blades are significantly more complex than assumed by the lower-fidelity models often used for design applications, and strongly vary during the rotor revolution. A comparison of the CFD integral estimates and the results of a blade-element momentum code is also presented to highlight strengths and weaknesses of low-fidelity codes for Darrieus turbine design.

The reported CFD results provide a valuable and reliable benchmark for the calibration of lower-fidelity models, which are still key to industrial design due to their very high execution speed.

Keywords

Darrieus wind turbine, unsteady Navier-Stokes simulations, CFD, [tip flows](#)

42 Nomenclature

43 Latin symbols

44	AoA	angle of attack	
45	AR	aspect ratio	[-]
46	c	blade chord	[m]
47	C_t	torque coefficient	[-]
48	C_p	pressure coefficient	[-]
49	CP	power coefficient	[-]
50	BEM	Blade Element Momentum	
51	CFD	Computational Fluid Dynamics	
52	H	turbine height	[m]
53	k	turbulent kinetic energy	[m ² /s ²]
54	NS	Navier-Stokes	
55	p	static pressure	[Pa]
56	PDEs	Partial Differential Equations	
57	R	turbine radius	[m]
58	RANS	Reynolds-Averaged Navier-Stokes	
59	SST	Shear Stress Transport	
60	T	torque per unit length	[Nm]
61	TSR	tip-speed ratio	[-]
62	u, v, w	Cartesian components of local fluid velocity vector	[m/s]
63	U	magnitude of absolute wind speed	[m/s]
64	\underline{v}	local fluid velocity vector	[m/s]
65	\underline{v}_b	local grid velocity vector	[m/s]
66	VAWTs	Vertical-Axis Wind Turbines	
67	W	magnitude of relative wind speed	[m/s]
68	x, y, z	reference axes	
69	y^+	dimensionless wall distance	[-]

70

71 Greek symbols

72	ϑ	azimuthal angle	[deg]
73	μ_t	turbulent viscosity	[Kg/m/s]
74	ρ	air density	[kg/Nm ³]
75	Φ	computational domain diameter	[m]
76	Ψ	computational domain height	[m]
77	ω	specific turbulence dissipation rate	[1/s]
78	Ω	turbine revolution speed	[rad/s]

79

80 Subscripts

81	∞	value at infinity	
82	ave	averaged value	

83

84 1. Introduction

85 1.1 Background

86 After most research on vertical-axis wind turbines (VAWTs) came to a standstill in the
87 mid 90's [1], the Darrieus wind turbine [2] is receiving again increasing attention of both
88 researchers and manufacturers [3-6]. For distributed wind power generation in the built
89 environment [7], inherent advantages of this turbine type, such as performance insensitivity

90 to wind direction, generator often positioned on the ground, low noise emissions [8],
91 enhanced performance in skewed [9] or highly turbulent and unsteady flows [10-12], may
92 outweigh disadvantages, such as lower power coefficients and more difficult start-up, with
93 respect to typical horizontal axis machines. Moreover, in densely populated areas VAWTs
94 are often preferred to other turbine types because they are perceived as aesthetically more
95 pleasant and thus easier to integrate in the landscape [13]. The applicability of Darrieus wind
96 turbines for utility-scale power generation making use of floating platforms also appears to
97 present important benefits in terms of overall dynamic stability [14].

98 Historically, the aerodynamic performance analysis of these rotors has been carried out
99 with low-fidelity methods, like the Blade Element Momentum (BEM) theory [1,15-17] or
100 lifting line methods [18-19]. More recently, however, the intrinsic limitations of these models
101 made clear that higher-fidelity tools are needed in order to understand in greater depth the
102 complex unsteady aerodynamics of Darrieus rotors [20], such as the interaction of the blades
103 with macro vortices [21] or dynamic stall [22].

104 While experimental testing is often quite difficult and expensive, Navier-Stokes (NS)
105 Computational Fluid Dynamics (CFD) can be a versatile and accurate means to improve the
106 understanding of VAWT unsteady aerodynamics and achieve higher-performance,
107 structurally sound and more cost-effective Darrieus turbine designs. The use of NS CFD for
108 simulating time-dependent Darrieus turbine aerodynamics is rapidly increasing due to both
109 the ongoing development and deployment of more powerful high-performance computing
110 hardware, such as large clusters of multi- and many-core processors [23], and also the
111 development of computationally more efficient algorithms.

112 113 *1.2 Previous CFD studies on Darrieus VAWTs*

114 Early use of the Reynolds-Averaged Navier-Stokes (RANS) CFD technology for
115 Darrieus rotor aerodynamics for investigating the complex fluid mechanics of these machines
116 was based mostly on two-dimensional (2D) simulations (e.g. [24]). An extensive literature
117 review of 2D RANS CFD studies is provided by Balduzzi et al. [25], along with an overview
118 of the numerical settings frequently used for Darrieus rotor RANS studies and guidelines for
119 the optimal set-up of these simulations. Two-dimensional RANS analyses, suitably corrected
120 for three-dimensional (3D) effects, such as struts resistive torque and blade tip losses, have
121 been used to estimate the turbine overall performance [26] and predominantly 2D
122 phenomena, like virtual camber [27] and virtual incidence [28] effects, the influence of
123 unsteady wind conditions on turbine aerodynamics [29], the evolution of the flow field at
124 start-up [30], and turbine/wake interactions [31].

125 However, the use of 2D simulations to analyse the flow field past real rotors may result
126 in significant uncertainties, due to the difficulty of reliably quantifying complex 3D
127 aerodynamic features such as blade tip flows, their dependence on the blade tip geometry and
128 their impact on the overall efficiency as a function of the blade aspect ratio. Moreover, most
129 3D aerodynamic features of Darrieus rotor flows vary not only spatially (e.g. dynamic stall
130 decreases from midspan to the blade tips, as shown below), but also temporally during each
131 revolution. It is difficult to develop corrections to improve the predictions of time-dependent
132 2D CFD analyses, and the resulting uncertainty on unsteady loads may severely impair both
133 aerodynamic and structural (e.g. fatigue) assessments. Therefore 3D CFD simulations are key
134 to characterizing and quantifying the aforementioned 3D aerodynamic phenomena. This is
135 important for reducing the uncertainty associated with modeling such phenomena on the basis
136 of a relatively small amount of data referring to existing turbines, and assumptions based on
137 overly simplistic analytical models. However, large computational resources are needed for
138 such simulations, due to the high temporal and spatial grid refinement needed for accurately
139 resolving all design-driving aerodynamic phenomena.

140 Comparisons of 2D and 3D simulations are sometimes carried out considering test
141 cases for which experimental data are available, as in Howell et al. [32] and Lam et al. [33].
142 In [32] the use of 2D RANS CFD led to relatively poor agreement with experiments: a
143 maximum power coefficient CP of 0.371 at a tip-speed ratio (TSR) of 2.4 was predicted
144 against a measured maximum CP of 0.186 at TSR=1.85. Using 3D simulations, the
145 maximum power coefficient was instead correctly predicted, although the shape of computed
146 and measured power curves presented significant differences. The $k-\varepsilon$ re-normalization group
147 turbulence model [34] was used for all simulations, but no detailed information on the mesh
148 size was provided, except for the indication of a high dimensionless wall distance ($y^+ \approx 10$)
149 which required the use of wall functions. Also in [35] notable discrepancies between the
150 results of 2D and 3D RANS simulations were observed: the 2D simulations predicted a
151 maximum power coefficient of 0.43 at TSR=4.5 against a maximum CP of 0.27 at TSR=1.85
152 predicted by the 3D analyses. A fairly coarse grid, consisting of 2.95 million elements was
153 used for the 3D simulations of the considered two-blade rotor, and the $k-\omega$ Shear Stress
154 Transport (SST) turbulence model [36] was used.

155 Gosselin et al. [37] used 2D and 3D RANS simulations with the $k-\omega$ SST turbulence
156 model to investigate the dependence of 3D effects on the blade aspect ratio, finding that an
157 aspect ratio of 7 led to a relative efficiency drop of 60 percent with respect to the 2D analysis.
158 Although the simulations were performed with very refined meshes (up to 700 nodes on each
159 airfoil), the article reports that no rigorous mesh-independence was obtained. Joo et al. [38]
160 analysed the aerodynamic characteristics of a two-blade rotor as a function of design
161 parameters such as solidity and optimal TSR using the 3D RANS model coupled to a
162 realizable $k-\varepsilon$ turbulence model. They used a computational mesh of 1.2 million elements
163 and compared their baseline results with available experimental data: a general
164 overestimation of the power curve was noticed, with a 10% discrepancy at the peak power.
165 Moreover, significant shape differences of computed and measured power curves were
166 observed, particularly in the right branch of such curves (i.e. for high TSR values), with the
167 measured curve being steeper than the computed one. A two-blade Darrieus rotor with
168 straight blades was analysed by Li et al. [35,39] by means of wind tunnel experiments and 3D
169 RANS simulations using the $k-\omega$ SST turbulence model. Numerical results compared
170 favourably to experimental data in the left branch (i.e. low TSR values) of the power curve,
171 but CFD significantly overestimated power for higher TSR, possibly due to excessively small
172 distance between the rotor and the farfield boundaries of the physical domain (about 2 rotor
173 diameters from the rotor center). The simulations used a grid with about 5 million elements,
174 and predicted a peak power coefficient of 0.24 at TSR=2.09 whereas experiments showed a
175 peak CP of 0.18 at TSR=2.18.

176 Alaimo et al. [40] carried out a comparative study of the aerodynamic performance of
177 three-blade Darrieus rotors using straight and helical blades. For the three-blade rotors they
178 analysed, they found that blade tip vortex flows significantly reduced the rotor performance
179 and that the use of helical blades significantly reduces this power loss. The largest grids used
180 for those 3D RANS analyses had about 10 million elements, and turbulence was modelled
181 using the $k-\varepsilon$ turbulence model with wall functions to enable the use of relatively coarse grids
182 and enhance numerical stability. De Marco et al. [41] performed 3D RANS simulations to
183 analyse the influence of the geometry of the blade supporting arms on the turbine
184 performance. Using grids featuring between 4 and 18 million elements and the $k-\omega$ SST
185 model, they found that inclined and aerodynamically shaped supporting arms can
186 significantly increase the mean power coefficient. Using computational meshes with up to 12
187 million elements and the $k-\omega$ SST model, Zamani et al. [42] characterized with 3D RANS
188 simulations the impact of J-shaped blades on Darrieus rotor torque and power characteristics
189 at low and medium TSR values, finding that this blade shape significantly increases the rotor

190 performance in these regimes, resulting in improved start-up characteristics. Orlandi et al.
191 [43] used 3D RANS simulations and the $k-\omega$ SST model to study the influence of skewed
192 wind conditions on the aerodynamic characteristics of a two-blade Darrieus turbine; to limit
193 the computational burden of the 3D analyses, grids with about 10 million elements were used.

194 A recent Navier-Stokes CFD study of a three-blade Darrieus rotor using pitching blades
195 to further improve the aerodynamic performance has made use of a Large Eddy Simulation
196 [44], an approach that can yield more accurate results than the RANS method. However,
197 resolved LES analyses require computational grids far larger than those needed for grid-
198 independent RANS analyses, and this makes the use of resolved 3D LES simulations even
199 more difficult than that of grid-independent 3D RANS analyses.

200 The aforementioned 3D CFD analyses highlighted new important aerodynamic
201 phenomena, but in almost all cases limited availability of computational resources imposed
202 the use of fairly coarse spatial and temporal refinement, and this may result in uncertainty due
203 to lack of complete grid-independence of the CFD solutions. Recent parametric analyses
204 investigating the impact of several numerical parameters on the computationally less
205 demanding 2D CFD analysis of Darrieus rotors [25,45-47] showed that the analysis reliability
206 - in terms of accuracy of both performance prediction and resolution of important flow
207 structures - is tremendously affected by the quality of the meshing and time-stepping
208 strategies. These studies highlighted that the minimum temporal and spatial refinement
209 required to obtain grid-independent solutions is quite high, due to the aerodynamic
210 complexity of these unsteady flows. Because of these constraints, the computational cost of
211 reliable 3D unsteady NS analyses of Darrieus rotor flows is extremely large due to the
212 necessity of maintaining the high temporal resolution indicated by the 2D parametric studies
213 and a high level of spatial refinement both in the grid planes normal to the rotor axis and the
214 3rd direction orthogonal to such planes. Refinement in the 3rd direction is essential to reliably
215 resolving 3D flow features. For example, the parametric study of [25] showed that temporal
216 and spatial grid-independent 2D RANS analyses of a three-blade rotor require grids with at
217 least 400,000 elements. To preserve the same accuracy level in a 3D RANS simulation of the
218 same turbine (modelling only half of the rotor making use of symmetry boundary conditions
219 on the plane at rotor midspan and ensuring adequate refinement in the tip region) the mesh
220 would consist of at least 90 million elements, which is almost ten times the size of the finest
221 meshes used in the 3D RANS studies of Darrieus rotor flows published to date. Failing to
222 maintain these refinement levels may reduce the benefits achievable by using 3D RANS
223 simulations to improve Darrieus rotor design.

224

225 *1.3 Study aim*

226 In this study, the COSA RANS research code, which features a very high parallel
227 efficiency, is used to investigate in great detail the 3D flow features of a rotating Darrieus
228 rotor blade and the impact of flow three-dimensionality on power generation efficiency. More
229 specifically, the study aims at providing a highly accurate analysis of the main 3D
230 phenomena occurring during each revolution of the considered one-blade rotor, including tip
231 vortices, dynamic stall and downstream vortex propagation, and to assess the impact of these
232 phenomena on the overall performance of this rotor. The use of a single rotating blade for the
233 type of analyses reported herein is not uncommon (see for example [40]). This set-up enables
234 a better understanding of individual key fluid mechanics phenomena adversely impacting
235 loads and energy efficiency of Darrieus rotors, and this information constitutes the first
236 knowledge level required to improve the design of these machines. Follow-on studies will
237 focus on additional 3D fluid mechanic aspects resulting from the multi-blade environment
238 making use of computational resources larger than those used in the present study.

239 To maximize the analysis reliability, a time-dependent 3D simulation using very high
 240 levels of spatial and temporal refinement is carried out using a large 98,304-core IBM BG/Q
 241 cluster.

242 The presented test case is expected to be highly valuable to other research groups both
 243 to verify new CFD approaches and to calibrate lower-fidelity models (e.g. model based on
 244 lifting line theory and free vortex methods), which are key to industrial design due to their
 245 extremely low computational cost.

246 The paper is organized as follows. [Section 2](#) presents the numerical methodology that
 247 has been followed in the study: sub-section 2.1 reports the governing equations solved by the
 248 COSA CFD code for the analysis of Darrieus rotor flows, sub-section 2.2 summarizes the
 249 main numerical features and previous work carried out with this code, and sub-section 2.3
 250 provides the main features of the case study and describes the adopted numerical set-up.
 251 [Section 3](#) presents the main results of the 3D CFD analysis and compares them to those of the
 252 2D analysis of the same case study, to highlight the impact of 3D effects. In [Section 3](#) the
 253 results of the RANS CFD analyses are also compared with those of the blade element
 254 momentum theory to highlight strengths and weaknesses of this engineering approach. A
 255 summary of the study and concluding remarks are finally provided in [Section 4](#).
 256

277 [2. Numerical methodology](#)

278 [2.1 Governing equations](#)

279 The compressible NS equations are a system of 5 nonlinear partial differential
 280 equations (PDEs) expressing the conservation of mass, momentum and energy in a viscous
 281 fluid flow. Averaging these equations on the longest time-scales of turbulence yields the so-
 282 called RANS equations, which feature additional terms depending on the Reynolds stress
 283 tensor. Making use of Boussinesq approximation, this tensor has an expression similar to that
 284 of the laminar or molecular stress tensor, with the molecular viscosity replaced by a turbulent
 285 or eddy viscosity [48-49]. [In the COSA CFD code, the eddy viscosity is computed by means](#)
 286 [of the two-equation \$k\$ - \$\omega\$ SST turbulence model \[36\]](#). Thus, turbulent flows are determined by
 287 solving a system of 7 PDEs.

288 Given a moving time-dependent control volume $C(t)$ with time-dependent boundary
 289 $S(t)$, the Arbitrary Lagrangian–Eulerian integral form of the system of the time-dependent
 290 RANS and SST equations in an absolute frame of reference is:

$$271 \quad \frac{\partial}{\partial t} \left(\int_{C(t)} \mathbf{U} dC \right) + \oint_{S(t)} (\underline{\Phi}_c - \underline{\Phi}_d) \cdot d\underline{S} - \int_{C(t)} \mathbf{S} dC = 0 \quad (1)$$

272 where \mathbf{U} is the array of conservative variables defined as:

$$273 \quad \mathbf{U} = [\rho \quad \rho \underline{v}' \quad \rho E \quad \rho k \quad \rho \omega]'; \quad (2)$$

274 The symbols ρ , \underline{v} , E , k and ω denote respectively fluid density, flow velocity vector of
 275 Cartesian components (u, v, w) , total energy per unit mass, turbulent kinetic energy per unit
 276 mass and specific dissipation rate of turbulent energy, and the superscript ' denotes the
 277 transpose operator. The total energy is defined as $E = e + (\underline{v} \cdot \underline{v})/2 + k$, where e denotes the
 278 internal energy per unit mass; the perfect gas law is used to express the static pressure p as a
 279 function of ρ , E , k and the mean flow kinetic energy per unit mass $(\underline{v} \cdot \underline{v})/2$. The generalized
 280 convective flux vector is defined as:

$$281 \quad \underline{\Phi}_c = \underline{E}_c \underline{i} + \underline{F}_c \underline{j} + \underline{G}_c \underline{k} - \underline{v}_b \mathbf{U} \quad (3)$$

282 where \mathbf{E}_c , \mathbf{F}_c and \mathbf{G}_c are respectively the x-, y- and z-component of $\underline{\Phi}_c$ and are given by:

$$\begin{cases}
 \mathbf{E}_c = [\rho u \quad \rho u^2 + p \quad \rho uv \quad \rho uw \quad \rho uH \quad \rho uk \quad \rho u\omega] \\
 \mathbf{F}_c = [\rho v \quad \rho uv \quad \rho v^2 + p \quad \rho vw \quad \rho vH \quad \rho vk \quad \rho v\omega] \\
 \mathbf{G}_c = [\rho w \quad \rho uw \quad \rho vw \quad \rho w^2 + p \quad \rho wH \quad \rho wk \quad \rho w\omega]
 \end{cases} \quad (4)$$

284 in which $H=E+p/\rho$ is the total enthalpy per unit mass. The vector \underline{v}_b is the velocity of the
 285 boundary S, and the flux term $-\underline{v}_b \mathbf{U}$ is its contribution of the boundary motion to the overall
 286 flux balance.

287 The expressions of the diffusive fluxes $\underline{\Phi}_c$ and the turbulent source term S appearing in
 288 Eq. (1) can be found in [48] and [50].

289

290 2.2 COSA CFD code

291 COSA is a compressible density-based finite volume code that solves the system of
 292 PDEs corresponding to Eq. (1) using structured multi-block grids. The code features a steady
 293 flow solver, a time-domain (TD) solver for the solution of general unsteady problems [48-
 294 49], and a harmonic balance solver for the rapid solution of periodic flows [50-52]. The
 295 second-order space discretization of the convective fluxes of both the RANS and the SST
 296 equations uses an upwind scheme based on Van Leer's MUSCL extrapolations and Roe's
 297 flux difference splitting. The second order discretization of all diffusive fluxes is instead
 298 based on central finite-differencing. The space-discretized RANS and SST equations are
 299 integrated in a fully-coupled fashion with an explicit solution strategy based on full
 300 approximation scheme multigrid featuring a four-stage Runge-Kutta smoother. Convergence
 301 acceleration is achieved by means of local time-stepping and implicit residual smoothing. For
 302 general time-dependent problems, the TD equations are integrated using a second order
 303 accurate dual time-stepping approach.

304 Comprehensive information on the numerical methods used by COSA and thorough
 305 validation analyses are reported in [50,52] and other references cited therein. For unsteady
 306 problems involving oscillating wings and cross-flow open rotors such as the Darrieus
 307 turbines, COSA solves the governing equations in the absolute frame of reference using
 308 body-fitted grids. In the case of Darrieus rotors in open field operation this implies that the
 309 entire computational grid rotates about the rotational axis of the turbine. The suitability of
 310 COSA for the simulation of Darrieus wind turbines has been recently assessed through
 311 comparative analyses with both commercial CFD codes and experimental data [53-54].

312

313 2.3 Case study and computational model

314 The selected case study is a one-blade H-Darrieus rotor using the NACA 0021 airfoil.
 315 The blade chord ($c=0.0858$ m), the blade length ($H=1.5$ m) and the rotor radius ($R=0.515$ m)
 316 were set equal to those used in the case-study of [24]; the blade was attached to the spoke at
 317 midchord according to the original 3-blade model of [24]. The decision of simulating a single
 318 blade was based both on physical considerations and on hardware limitations. First, a one-
 319 blade model is sufficient to investigate all the desired 3D flow structures that lead to an
 320 efficiency reduction of a finite blade. At the same time, the use of a single blade allows one to
 321 isolate and analyze fundamental aerodynamic phenomena of finite-length blade
 322 aerodynamics, removing additional aerodynamic effects due to multiple blade/wake
 323 interactions occurring in a multi-blade rotor. From a practical viewpoint, the need of ensuring
 324 an adequate level of spatial refinement both in the grid planes normal to the rotor axis and in

325 the axial direction would have required a grid with more than 100 million elements for a
326 three-blade rotor, which was beyond the resources available for this project.

327 To further reduce the computational cost of the 3D simulation, the central symmetry of
328 H-Darrieus rotors was exploited, enabling to simulate only one half of the rotor flow, thus
329 halving computational costs. Consequently, the aspect ratio (AR) of the simulated blade
330 portion is 8.74 which is half that of the actual blade. The modeled blade portion was
331 contained in a cylindrical domain (Fig. 1) of radius $\Phi=240R$, a value chosen to guarantee a
332 full development of the wake, based on the sensitivity analyses reported in [53]. The domain
333 height was set to $\Psi=2.53H$, corresponding to half the height of the wind tunnel where the
334 original 3-blade model was tested [24,54]; measured data from these tests were previously
335 used for validating the robustness of the RANS CFD methodology [26,53] also used in the
336 present study.

337 The 3D structured multi-block grid (2D and 3D views are reported in Fig. 2) was
338 obtained with the software ANSYS[®] ICEM[®] by first generating a 2D mesh past the airfoil
339 using the optimal mesh settings identified in [47,49], and then extruding this mesh in the
340 spanwise (z) direction and filling up with grid cells the volume between the blade tip and the
341 upper (circular) farfield boundary. The far-field boundary condition enforced on the lateral
342 (cylindrical) boundary and the upper boundary of the domain is based on suitable
343 combinations of one-dimensional Riemann invariants and user-given freestream data, namely
344 pressure, density and velocity components. The sub-set of these far-field data combined with
345 suitable Riemann invariants depends on whether the fluid stream enters or leaves the
346 computational domain at the considered boundary point (the code detects automatically
347 inflow and outflow points of the boundaries at each iteration). The complete definition of this
348 far-field boundary condition is provided in [55]. On the blade surface, a no-slip condition is
349 enforced. Since the equations are solved in the absolute frame of reference, this requires
350 imposing that the fluid velocity at the blade surface equals the velocity of the blade surface
351 itself at the considered wall point, where pressure and density are extrapolated from the
352 interior domain. The 2D grid section normal to the z-axis and containing the airfoil (Fig. 2(a))
353 consisted of 4.3×10^5 quadrilateral cells. The airfoil was discretized with 580 nodes and the
354 first element height was set to $5.8 \times 10^{-5}c$ to guarantee a dimensionless wall distance y^+ lower
355 than 1 throughout the revolution. As recommended in [25], a fairly high mesh refinement of
356 both leading and trailing edge regions was adopted (Fig. 2(b)), and a high refinement in the
357 airfoil region within one chord from the airfoil surface was also used to resolve the separated
358 flow regions at high angle of attack (AoA) [27]. After extrusion in the z direction, 80 grid
359 layers in the half-blade span were formed (Fig. 2(c)), with progressive grid clustering from
360 midspan to tip to ensure an accurate description of tip flows. A fairly high grid refinement
361 was also adopted in the whole tip region above the blade in order to capture the flow
362 separation and the tip vortices. The final mesh consisted of 64 million hexahedral cells.

363 The rotor flow field was computed by solving the system of governing equations
364 corresponding to Eq. (1), that is by solving the RANS and SST equations in the absolute
365 frame of reference. In such frame, the entire body-fitted grid rotates past the rotor axis, the
366 additional flux components due to the grid motion is accounted for by the term $-\underline{v}_b \mathbf{U}$
367 appearing in Eq. (3), and no sliding surface is required.

368 To keep computational costs within the limits of the available resources, only one
369 operating condition was simulated, corresponding to a tip-speed ration (TSR) of 3.3. This
370 condition corresponds to the same revolution speed already analyzed by some of the authors
371 for the 3-blade turbine in [53]. For a 1-blade rotor, this TSR corresponds to a different point
372 of the rotor power curve. The operating condition corresponding to this TSR, however, was
373 considered of particular interest also for the 1-blade rotor because, also in this case, a) it
374 corresponds to fairly high efficiency and thus a regime at which the rotor is expected to work

375 more often than at other TSRs, and b) it features several complex aerodynamic phenomena
376 (e.g. stall and strong tip vortices) posing a significant modelling challenge for the CFD
377 analysis. Figure 3 displays the power coefficient at $TSR=3.3$ evaluated with the CFD analysis
378 reported below on the expected power curve, which was calculated with a computationally
379 more affordable code based on Lifting Line Theory coupled to a free vortex wake model. The
380 model was successfully tuned on this case-study in [56] and thus it is expected to provide a
381 power curve prediction fairly consistent with the CFD analysis reported below.

382 The free-stream wind speed was $U=9.0$ m/s. The turbulence farfield boundary
383 conditions were a turbulent kinetic energy (k) based on 5% turbulence intensity and a
384 characteristic length of 0.07 m.

385 The 3D and 2D simulations reported below were performed with the time-domain
386 solver of COSA. The 3D simulation was run on an IBM BG/Q cluster [57] featuring 8,144
387 16-core nodes for a total of 98,304 cores. Exploiting the outstanding parallel efficiency of
388 COSA, the simulation could be carried out using about 16,000 cores. This required
389 partitioning the grid into 16384 blocks using in-house utilities, and this operation was
390 performed starting from a grid with fewer blocks generated with the ANSYS® ICEM® grid
391 generator. All grid blocks had identical number of cells to optimize the load balance of the
392 parallel simulation. Using a time-discretization yielding 720 steps per revolution, the
393 simulation needed 12 revolutions to achieve a fully periodic state. The flow field was
394 considered periodic once the difference between the mean torque values of the last two
395 revolutions was smaller than 0.1% of the mean torque in the revolution before the last. The
396 wall-clock time required for this 3D simulation was about 653 hours (27.2 days).

397

398 **2.4 Grid and time-step sensitivity analyses**

399 One of the key elements of this study is that the 3D calculation was carried out using a
400 high level of spatial and temporal resolution. The 3D grid used to carry out the analyses
401 reported in Section 3 was obtained by extruding in the third direction the 4.3×10^5 -element 2D
402 grid described above, and such grid was shown to provide accurate and grid-independent
403 results in [53].

404 To assess the impact of using coarser spatial and temporal refinement on the computed
405 solution, the considered flow regime was also simulated using only 360 steps per revolution
406 and a coarser 3D grid with 8 million elements, obtained from the 64million element fine grid
407 by removing every second line in all three directions.

408 The periodic profiles of the instantaneous torque coefficient C_t obtained with the coarse
409 and fine grids are compared in Fig. 4, and the definition of C_t is provided by Eq. (5), in which
410 T denotes the instantaneous torque on the entire blade, U_∞ and ρ_∞ denote respectively the far-
411 field wind speed and the air density, c is the blade chord, and H is the overall blade length.
412 The angular position $\vartheta=0^\circ$ corresponds to the blade leading edge facing the oncoming wind
413 and entering the upwind half of its revolution.

414

$$C_t = \frac{T}{\frac{1}{2} \rho_\infty U_\infty^2 c^2 H} \quad (5)$$

415 The comparison shows that differences between the two predictions occur over most
416 parts of the period, particularly around the maximum values of C_t . These discrepancies are
417 caused by differences in the prediction of strength and timing of stall on the airfoils and
418 under-resolved wakes and wake/blade interactions when using the coarse grid. The position
419 of the curve peak (maximum C_t in the upwind region of rotor trajectory) predicted by the
420 coarse grid has an error of about 3 degrees in azimuthal coordinates, leading to a shift of the

421 curve in the range between $\vartheta=90^\circ$ and $\vartheta=300^\circ$. Such discrepancies, reported in Fig. 4 also as
 422 the difference between the coarse and fine grid profiles normalized by the revolution-
 423 averaged mean torque of the fine grid (curve labeled “% variation”) result in the mean torque
 424 coefficient obtained with the coarse grid being 3.2 percent higher than that obtained with the
 425 fine grid. As discussed in the following, this difference corresponds to nearly 40 percent of
 426 the energy efficiency loss due to finite blade length effects. This highlights the importance of
 427 using a fine grid for this type of analyses.

428 The impact of the mesh refinement on the resolution of some of the 3D flow
 429 phenomena occurring during the revolution are examined in Fig. 5. This figure shows the
 430 extent of the vortices generated at the blade tip at $\vartheta=80^\circ$ predicted with the two meshes. The
 431 red and blue vortices represent the regions of ascending and descending flow, respectively.
 432 The higher dissipation of the coarse mesh leads to an under-prediction of the downstream
 433 propagation of the vortex, which is reduced from about three chords (Fig 5(b)) to less than
 434 two chords (Fig 5(a)). The coarse grid under-estimation of the tip effects contributes to the
 435 overestimation of the torque highlighted in Fig. 4. The vorticity contours at midspan when
 436 the blade is at $\vartheta=315^\circ$ are compared in Fig. 6 to assess the resolution of the free convection of
 437 vorticity in the downstream region. With the finer mesh the wake is resolved more sharply,
 438 thus fulfilling essential prerequisites for adequately resolving blade-wake interactions in the
 439 downwind part of the revolution. The under-resolution of the wake in the downwind rotor
 440 region contributes to the higher torque produced by the blade when interacting with the wake
 441 shed in the upstream trajectory. The impact of all these vortical phenomena on the rotor
 442 performance is even higher in multi-blade rotors, due to higher number of interactions (and
 443 thus energy loss events) per revolution.

444 3. Results and discussion

446 Figure 7(a) reports the instantaneous torque coefficient per unit length (C_{tz}) at different
 447 span lengths along the blade (0 percent and 100 percent correspond to midspan and tip,
 448 respectively). The instantaneous torque coefficient per unit length C_{tz} is defined by Eq. (6).
 449 Here T_z denotes the instantaneous torque per unit blade length at the considered spanwise
 450 position.

$$451 \quad C_{tz} = \frac{T_z}{\frac{1}{2} \rho_\infty U_\infty^2 c^2} \quad (6)$$

452 Figure 7(b) reports three torque profiles. The profile labelled 2D refers to the results of
 453 a 2D simulation of the same rotor, and corresponds to the “ideal” torque of a blade with
 454 infinite span, i.e. without any secondary effects at the blade tip. This 2D simulation was
 455 carried out using a mesh equal to the midspan section of the 3D fine mesh and the same
 456 numerical parameters of the 3D simulations. The torque profile labelled “0%” is the torque
 457 per unit blade length at midspan of the finite-length rotor, whereas the torque profile labelled
 458 3D is the overall torque coefficient C_t of the 3D rotor defined in Eq. (7). The result obtained
 459 by using this definition is identical to that obtained by using Eq. (5).

$$460 \quad C_t = \frac{2}{H} \int_0^{\frac{H}{2}} C_{tz} dz \quad (7)$$

461 Examination of these profiles reveals several important facts. Firstly, the ideal 2D
 462 torque and the 3D torque profiles are characterized by similar patterns, including the

463 occurrence of two relative maxima, one in the upwind the other in the downwind regions, and
464 also similar azimuthal positions of both maxima: the maximum torque in the upwind portion
465 of the revolution is located at $\vartheta \approx 88.5^\circ$ and the maximum torque in the downwind portion of
466 the revolution is located at $\vartheta \approx 257^\circ$ in both cases. This behaviour is in line with the analyses
467 of both Lam [33] and Alaimo [40], which showed that the periodic torque profiles obtained
468 with 2D and 3D simulations differ significantly for their amplitudes but have comparable
469 shapes. Figure 7(b) also highlights that the differences between the 2D torque profile and that
470 at midspan of the 3D rotor are negligible, highlighting that 3D flow effects due to tip flows
471 do not reach this position.

472 Examination of all profiles of Fig. 7(b) shows that the effects of blade finite-length
473 effects are very small when the blade loading is low, i.e. when the angle of attack is low
474 ($0^\circ < \vartheta < 40^\circ$ and $130^\circ < \vartheta < 210^\circ$): in these portions of the revolution, the 2D and both 3D curves
475 are almost superimposed. When the incidence increases, the blade load also increases and the
476 blade starts experiencing stall. Figure 8 reports the top view of the vorticity contours at
477 midspan at three azimuthal positions to examine the onset of stall in the upwind zone. At
478 $\vartheta = 70^\circ$ a small separation region forms on the suction side of the blade. At $\vartheta = 80^\circ$ the blade
479 stall has become significant, since the flow is detached from the blade. At the position of
480 torque peak a large region of the suction surface is affected by stall. Consequently, the torque
481 loss due to tip effects also increases because the strength of tip vortex flow increases with the
482 flow incidence. The same behaviour can be seen also in the downwind zones. Closer
483 inspection of the 2D and mean 3D CP curves shows that these effects are strongest in the
484 upwind region of the period, where a maximum difference of 9.7 percent between the torque
485 peaks occurs.

486 Examining the torque profiles at the spanwise positions considered in Fig. 4(a), some
487 additional observations can be made:

- 488 • The torque profiles of the blade sections at 20%, 40% and 50% semispan are almost
489 identical, indicating that at least half of the blade is characterized by a predominantly
490 2D flow with negligible impact of tip flow effects;
- 491 • The torque profiles of the blade sections at 60%, 70% and 80% show a progressive
492 reduction of the torque peak, down to -14 percent with respect to the midspan section.
493 The remainder of the torque curve is less affected, especially in the downwind zone;
- 494 • The torque profiles of the blade sections at 90%, 95% and 97.5% show that at these
495 positions, 3D effects are strong throughout the whole revolution. Notably, in the
496 regions of positive torque production, the efficiency is remarkably reduced;
- 497 • In proximity of the blade tip (99%), almost no positive contribution to the torque output
498 is given, due to the large load reduction;
- 499 • The azimuthal position of the torque peak occurs later in the cycle as one moves
500 towards the tip, with a 5° shift between the 0% and 97.5% sections. This can be
501 explained with a reduction of the incidence angle (downwash), as shown below. The
502 experiments of Li et al. [35] highlight the same trend and show that the aforementioned
503 shift is even more pronounced for a turbine with a very low aspect ratio (AR=4.5).

504 To compare the CFD prediction of the impact of finite blade effects on turbine
505 performance to that of the widespread low-fidelity BEM theory, Fig. 9 compares the 2D and
506 mean 3D torque profiles obtained with NS CFD and the corresponding estimates obtained
507 with the VARDAR research code, a state-of-the-art BEM code developed at the University of
508 Florence [6,17-18] using the ubiquitous Leicester-Prandtl model for the finite-wing
509 correction [58]. The two BEM profiles of Fig. 9 differ in that one includes tip flow corrections
510 and the other does not. Examination of these profiles shows that the reduction of the torque
511 peak in the upwind portion of the revolution predicted by the CFD analyses is in good
512 agreement with that estimated with the simplified tip flow model included in the BEM

513 theory, and the shapes of the CFD and BEM torque profiles are in a qualitatively good
514 agreement. Conversely, the patterns of the torque curves in the downwind portion of the
515 revolution predicted by the BEM and CFD analyses are significantly different, and the torque
516 reduction due to blade finite length predicted by the BEM analysis is higher than predicted by
517 CFD. This comparative analysis highlights the potential of using CFD also for further
518 improving the predictions of low-fidelity engineering tools, which are key to Darrieus rotor
519 industrial design due to their extremely small computational requirements.

520 To provide a different quantitative perspective of the impact of tip losses, Fig. 10
521 compares the CFD and BEM profiles of mean torque coefficient per unit length. For each
522 blade height the mean value is obtained by averaging the profiles of Fig. 4(a) over one
523 revolution. The figure also reports the constant mean torque values of the 2D and 3D
524 simulations for both the CFD and BEM models. All curves are normalized with respect to the
525 mean 2D torque coefficient. One sees that the mean blade performance is almost unaffected
526 by tip-effects up to approximately 70% semispan. More specifically, it is found that tip flow
527 effects adversely affect the performance of the blade for a span length of approximately $2.6c$
528 (yellow zone in Fig. 10). In terms of aggregate data, the tip effects yield a reduction of the
529 rotor torque of 8.6% with respect to the 2D calculation with virtually infinite span. This can
530 be seen as an equivalent reduction of the actual blade's height of $0.75c$ for each half blade
531 (red colored zone in Fig. 10). Such a correction factor needs to be accounted for when
532 estimating the turbine performance by means of 2D simulations.

533 The observations above are in accordance with the findings of Li et al. [35] in terms of
534 performance drop as a function of the distance from the tip. Their experiments showed that at
535 55% semispan, corresponding to a distance of $1.0c$ from the tip, the torque peak is greatly
536 reduced. At this blade height, they found a CP reduction of 40% over the midspan value at
537 $TSR=2.2$ and 60% at $TSR=2.5$, corresponding to an equivalent reduction of the actual blade's
538 height by $1.8c$ and $2.7c$, respectively. Other analyses focused on estimating the mean power
539 reduction due to finite blade length effects through comparisons of 2D and 3D CFD analyses
540 [32,33,37,40], but their results are not directly comparable with the present study due to the
541 use of different aspect ratio, rotor solidity, TSR, airfoil geometry and number blades..
542 Overall, the equivalent height reduction can vary from $0.8c$ for a NACA 0022 three-blade
543 rotor at $TSR=1.3$ [32] up to $5c$ for a NACA 0018 two-blade rotor at $TSR=4.5$ [33].

544 To investigate in greater detail the 3D phenomena accounting for energy efficiency
545 reduction, the Mach contours and streamlines at the angular position of maximum separation
546 ($\vartheta=120^\circ$) are examined in Fig. 11(a). Different spanwise sections are considered to analyse
547 the flow pattern alterations from midspan to the blade tip.

548 In the central portion of the blade (from midspan to about 70% semispan) the
549 streamlines are contained in planes orthogonal to the blade axis, indicating a predominantly
550 2D flow character, and a fairly large region of separated flow in the rear of the suction side.
551 Closer to the tip (90% semispan) the downwash due to the tip flow reduces the effective AoA
552 with respect to that at midspan, and the extension of the stall region is thus reduced. The skin
553 friction lines and contours of the z velocity component (w) on the blade suction surface
554 reported in Fig. 11(b) show the extension of the region affected by downwash. Near the tip,
555 the flow on the pressure side is no longer able to follow the blade profile, and travels over the
556 tip due to the pressure difference between the pressure side and the suction side. The tip
557 vortex flow is responsible for the downwash velocity component and therefore for the
558 incidence variation along the span, in accordance with the theory of finite wings [58]. It is
559 noted that the finite wing effects occurring in Darrieus rotors are more complex than those
560 encountered in fixed finite wings. This is primarily because of the flow curvature associated
561 with the circular trajectory of the blade, and also the flow nonlinearities due to dynamic stall.

562 To quantify the impact of these effects, it is convenient to examine the curves of the
563 torque coefficient per unit length at midspan and 90% semispan (Fig. 12). The percentage
564 difference between the two curves (i.e. the torque coefficient difference between the curves at
565 each azimuthal angle divided by the revolution-averaged torque coefficient at midspan) is
566 also reported to quantify the dependence of the torque variation on the azimuthal position. A
567 notable torque reduction occurs in the interval $40^\circ < \vartheta < 130^\circ$. In addition, a large and sudden
568 torque reduction occurs towards the end of the revolution, in the interval $315^\circ < \vartheta < 340^\circ$, a
569 range in which the AoA is decreasing and goes below the value yielding stall. Also, an
570 inversion in the expected trend is noticed close to $\vartheta=150^\circ$, where the tip section performs
571 better than the midspan section: the torque of the section at 90% semispan is about 10 percent
572 higher than that at midspan. According to the finite wing theory, the lift should be in fact
573 always reduced in proximity of the tip. Therefore, the inversion at $\vartheta=150^\circ$ cannot be
574 explained with this theory alone. This occurrence and the sudden torque loss of the tip section
575 towards the end of the revolution are analysed in further detail below.

576 To investigate the origin of the sudden torque reduction at the blade tip in the interval
577 $315^\circ < \vartheta < 340^\circ$, isosurfaces of the turbulent kinetic energy field at selected azimuthal positions
578 are examined in Fig. 13. The color scale is based on the intensity of the velocity component
579 along the z-axis (w). Three azimuthal positions of the blade are considered: $\vartheta=60^\circ$, $\vartheta=180^\circ$
580 and $\vartheta=315^\circ$. During the upwind half of the revolution ($\vartheta=60^\circ$) the tip vortex is strong, since
581 the vertical component of velocity is fairly high. A high turbulence region is then generated
582 from the blade tip. At $\vartheta=180^\circ$, the region of high turbulent kinetic energy corresponding to
583 the tip vortex is increased in size and length, and is still associated with large values of w .
584 This strong vortex detaches from the blade, is convected by the wind, and is re-encountered
585 by the blade at $\vartheta=315^\circ$. The blade interaction with this vortex induces a more pronounced
586 reduction of the torque with respect to the 2D case, where this effect is absent.

587 To investigate the reasons for the higher torque of the 90% section over the midspan
588 section at $\vartheta=150^\circ$, top views of the streamlines at $\vartheta=150^\circ$ and $\vartheta=48^\circ$ are examined in Fig. 14.
589 The position $\vartheta=48^\circ$ is selected because this is the other angular position of the upwind half of
590 the revolution experiencing the same AoA of $\vartheta=150^\circ$. Streamlines on both the pressure and
591 suction sides of the blade are visualized at four different span locations. At $\vartheta=48^\circ$ the
592 downwash effect is visible: moving from midspan to the tip, the incidence of the oncoming
593 flow decreases and the air stream after the trailing edge is more aligned to the airfoil chord.
594 This phenomenon is not very pronounced due to the low loading on the blade at this angular
595 position. At $\vartheta=150^\circ$, moving from midspan to the tip, the incidence of the oncoming flow is
596 progressively reduced similarly to what seen at $\vartheta=48^\circ$. However, the flow pattern on the
597 suction side of the central portion of the blade is significantly different from that at $\vartheta=48^\circ$,
598 despite the fact that the AoA is similar in the two cases. A large separation region exists at
599 $\vartheta=150^\circ$ due to stall. Due to the finite wing length, a strong modification of this flow pattern is
600 observed moving towards the tip: from 70% semispan, the flow is attached due to lower
601 downwash-induced loading and is more aligned to the airfoil chord after the trailing edge.

602 The observations above can be explained by a combined effect of downwash and
603 dynamic stall. From $\vartheta=0^\circ$ to $\vartheta=90^\circ$ the AoA increases and stall in the central blade portion
604 occurs between $\vartheta=70^\circ$ and $\vartheta=80^\circ$. The dominant effect is that of the downwash which
605 reduces the AoA to the outer portion of the blade. When the AoA reaches its maximum
606 towards $\vartheta=90^\circ$, the central portion of the blade experiences high level of stall. From $\vartheta=90^\circ$ to
607 $\vartheta=180^\circ$ the AoA decreases but the central portion of the blade remains stalled due to delay of
608 the flow in readjusting to the decreasing incidence (a distinctive feature of dynamic stall).
609 However, the outer sections of the blade remain stall-free, and this is the reason why at
610 $\vartheta=150^\circ$ the torque of the tip sections is higher than that of the midspan section, whereas the
611 opposite is observed at $\vartheta=48^\circ$.

612 Fig. 15 presents an analysis of the same type of that of Fig. 14 for the angular positions
 613 $\vartheta=210^\circ$ and $\vartheta=300^\circ$. Both positions belong to the downwind portion of the rotor trajectory
 614 and are characterized by a comparable AoA. However at $\vartheta=210^\circ$ the AoA is increasing
 615 whereas at $\vartheta=300^\circ$ the AoA is decreasing. One notices that the streamline pattern at $\vartheta=210^\circ$ is
 616 similar to that at $\vartheta=48^\circ$. At $\vartheta=300^\circ$ the streamline patterns from midspan to tip are the same
 617 as those at $\vartheta=210^\circ$. The similarity of the flow patterns at these two positions is due to the fact
 618 that no stall occurs in the downwind portion of the rotor trajectory.

619 Fig. 16 depicts the blade streamlines at $\vartheta=315^\circ$, the position at which the tip vortex
 620 interacts with the outboard portion of the blade in its downwind trajectory, as highlighted in
 621 Fig. 13. One observes a sudden deviation of the oncoming flow in the tip region with respect
 622 to the flow direction at midspan. Such deviation is due to the blade-vortex interaction, which
 623 prevails over the effects due to downwash.

624 All aforementioned results can be more quantitatively described by evaluating the
 625 pressure coefficient (C_p) distributions and the vorticity contours along the blade. The pressure
 626 coefficient used in this study is defined by Eq. (7), where p denotes the static pressure at the
 627 airfoil surface. Due to the difficulty of properly defining the actual relative wind speed at
 628 each blade height, the relative flow velocity w_{th} used to calculate C_p neglects the induced
 629 velocity and is computed using the vectorial sum of the absolute free-stream velocity and
 630 entrainment velocity ΩR .

631 Fig. 17 reports the C_p profiles at different blade heights for three key angular positions:
 632 maximum loading ($\vartheta=80^\circ$), inversion of torque of midspan and tip sections ($\vartheta=150^\circ$) and
 633 maximum loading in the downwind half of the revolution ($\vartheta=240^\circ$). The objective of this
 634 analysis is to highlight the impact of downwash and stall at different angular positions.

$$635 \quad C_p = \frac{P - P_\infty}{\frac{1}{2} \rho_\infty w_{th}^2} \quad (7)$$

636 At $\vartheta=80^\circ$ the blade is subject to high loading (high AoA and high relative speed). The
 637 top subplot of Fig. 17 confirms that, in these conditions, 3D flow effects affect almost 40
 638 percent of the blade (from the tip to 60% semispan), since moving from midspan to the tip,
 639 the C_p profile at 60% already shows a slight loading reduction with respect to midspan.
 640 Closer to the tip, the suction side of the blade is characterized by an almost constant pressure,
 641 indicating that this blade portion generates a small lift. As a result, the torque of the tip
 642 sections is substantially lower than that of the midspan section, and the torque becomes
 643 negative at 97.5% midspan, as shown in Fig. 7. At $\vartheta=240^\circ$ (middle subplot of Fig. 16) the
 644 AoA is high but the relative speed magnitude is lower than at $\vartheta=80^\circ$. In these conditions 3D
 645 flow effects affect only the last 20 percent of the semispan (i.e. from 80% semispan to tip):
 646 significant differences in the C_p profiles with respect to the midspan values are observed only
 647 on the last 10 percent of the blade, where the loading becomes significantly smaller than at
 648 midspan. Unlike at the two angular positions just discussed, a strong flow separation due to
 649 stall occurs at $\vartheta=150^\circ$ (bottom subplot of Fig. 17). This is highlighted by the pressure profiles
 650 at 0% and 60% semispan, which feature a fairly shallow slope on the suction side. In this
 651 circumstance, the lower AoA at the tip sections induced by the tip vortex-related downwash
 652 results in the flow past such tip sections remaining attached and these sections outperforming
 653 the midspan region of the blade.

654 The evolution of the vorticity contours at different blade span heights is presented in
 655 Fig. 18. In the upwind half of the revolution, the two positions $\vartheta=40^\circ$ and $\vartheta=140^\circ$ are of
 656 particular interest. Although at these two positions the torque profiles along the blade are
 657 comparable (see Fig. 7(a) and Fig. 7(b)), the vorticity patterns and thus the flow field are
 658 remarkably different. On the other hand, moving to the downwind half of the revolution, one

659 sees that the vorticity patterns around the blade are quite similar at all azimuthal positions.
660 These patterns are in line with the previous analyses of streamlines and pressure coefficient
661 profiles.

662 Figure 19 reports the top view of the vorticity contours at four different span locations
663 at the two aforementioned azimuthal positions and highlights the vorticity differences in
664 greater detail. At $\vartheta=40^\circ$ the vorticity contours are very similar, moving from midspan to tip,
665 whereas at $\vartheta=140^\circ$ the large separation region due to stall is clearly visible along a large
666 central portion of the blade.

667

668 4. Conclusions

669 A 3D time-accurate Reynolds-averaged Navier-Stokes CFD analysis of an aspect ratio
670 17.5 blade rotating in Darrieus-like motion has been presented. Special attention was paid to
671 the description of 3D flow effects and their impact on the energy efficiency of Darrieus rotor
672 blades. This was accomplished also by comparative analyses of 3D and 2D CFD analyses.
673 The presented 3D CFD results were obtained with a highly refined analysis using a grid with
674 64 million elements and time-marching the flow field to a periodic state using 720 time-steps
675 per revolution. A 3D mesh sensitivity analysis was also presented. The main outcomes of the
676 analysis can be summarized as follows:

- 677 a) 3D flow effects due to finite blade length reduce the mean power of the considered
678 17.5 aspect ratio blade by 8.6 percent with respect to the torque of the
679 corresponding infinite blade. Such mean torque reduction corresponds to a
680 reduction of the effective blade length of $1.5c$ ($0.75c$ for each half blade).
- 681 b) A strong interaction between the tip-vortex released in the upwind portion of the
682 blade revolution and the blade traveling in the downwind region occurs at $\vartheta=315^\circ$,
683 and this yields an additional reduction of the outboard blade sections in this region
684 of the revolution.
- 685 c) Finite blade length effects do not modify significantly the overall shape of the blade
686 torque profile over the revolution with respect to the torque profile of the
687 corresponding infinite blade;
- 688 d) For given azimuthal position, the torque profile along the blade height varies
689 substantially from midspan to tip, and the pattern of these variations strongly
690 depends on the azimuthal position; i.e. on the magnitude of the relative velocity of
691 the oncoming flow and its local angle of attack;
- 692 e) The mean torque reduction predicted by the 3D CFD analysis and that of a state-of-
693 the-art BEM analysis using tip loss corrections is comparable, but the profiles of the
694 blade torque in the downwind portion of the revolution differ significantly. The
695 reliability of BEM analyses may be improved by using 3D CFD results to develop
696 azimuthal position-dependent tip loss corrections;
- 697 f) The 3D grid sensitivity analysis highlighted that the use of a coarser grid, with size
698 comparable to those used in most 3D Darrieus studies to date, may yield uncertainty
699 levels in the prediction of tip vortex flows, blade/wake/tip vortex interactions, and
700 dynamic stall timings and strength. All these phenomena affect torque and power
701 generation. The mean power predicted by a typical coarse grid and the fine grid of
702 this study differed by more than 3 percent. and significantly larger differences are
703 expected for multi-blade rotors due to higher number of blade/wake/tip vortex
704 encounters per revolution.

705 Future work will include investigating 3D flow effects at different tip-speed ratios,
706 particularly the lower ones, at which the impact of dynamic stall is expected to be more
707 pronounced than at the considered regime, and extending this analysis to multi-blade

708 turbines, to assess in detail all aspects of wake/blade interactions. This type of high-fidelity
709 analyses provides valuable data for validating and further improving the reliability of low-
710 fidelity tools such as BEM codes and codes based on lifting line theory and free vortex
711 transport methods. Due to their extremely high execution speeds, these engineering tools are
712 of crucial importance to improving the design of future small and large Darrieus turbines.

713

714 **Acknowledgements**

715 We acknowledge use of Hartree Centre resources in this work. The STFC Hartree
716 Centre is a research collaboratory in association with IBM providing High Performance
717 Computing platforms funded by the UK's investment in e-Infrastructure. The Centre aims to
718 develop and demonstrate next generation software, optimised to take advantage of the move
719 towards exa-scale computing. Part of the reported simulations were also performed on two
720 other clusters. One is POLARIS, part of the N8 HPC facilities provided and funded by the N8
721 consortium and EPSRC (Grant No.EP/K000225/1). The Centre is co-ordinated by the
722 Universities of Leeds and Manchester. The other resource is the HEC cluster of Lancaster
723 University, which is also kindly acknowledged. Finally, thanks are due to Prof. Ennio
724 Antonio Carnevale of the Università degli Studi di Firenze for supporting this research.

725

726 **References**

- 727 [1] Paraschivoiu I. Wind turbine design with emphasis on Darrieus concept. Polytechnic
728 International Press: Montreal (Canada), 2002.
- 729 [2] Darrieus GJM. Turbine having its rotating shaft transverse to the flow of the current.
730 US Patent No.01835018, 1931.
- 731 [3] Tjiu W, Marnoto T, Mat S, Ruslan MH, Sopian K. Darrieus vertical axis wind turbine
732 for power generation I: Assessment of Darrieus VAWT configurations. *Renewable*
733 *Energy* 2015; 75(March 2015): 50-67. DOI: 10.1016/j.renene.2014.09.038
- 734 [4] Tjiu W, Marnoto T, Mat S, Ruslan MH, Sopian K. Darrieus vertical axis wind turbine
735 for power generation II: Challenges in HAWT and the opportunity of multi-megawatt
736 Darrieus VAWT development. *Renewable Energy* 2015; 75(March 2015):560-571.
737 DOI: 10.1016/j.renene.2014.10.039
- 738 [5] Bianchini A, Ferrara G, Ferrari L. Design guidelines for H-Darrieus wind turbines:
739 Optimization of the annual energy yield. *Energy Conversion and Management*
740 2015;89:690-707. DOI: 10.1016/j.enconman.2014.10.038
- 741 [6] Bianchini A, Ferrari L, Magnani S. Energy-yield-based optimization of an H-Darrieus
742 wind turbine. *Proceedings of the ASME Turbo Expo 2012, Copenhagen (Denmark),*
743 *June 11-15, 2012.* DOI: 10.1115/GT2012-69892
- 744 [7] Balduzzi F, Bianchini A, Carnevale EA, Ferrari L, Magnani S. Feasibility analysis of a
745 Darrieus vertical-axis wind turbine installation in the rooftop of a building. *Applied*
746 *Energy* 2012; 97: 921–929. DOI: 10.1016/j.apenergy.2011.12.008
- 747 [8] Mohamed MH. Aero-acoustics noise evaluation of H-rotor Darrieus wind turbines.
748 *Energy* 2014; 65(1): 596-604. DOI: 10.1016/j.energy.2013.11.031.
- 749 [9] Bianchini A, Ferrara G, Ferrari L, Magnani S. An improved model for the performance
750 estimation of an H-Darrieus wind turbine in skewed flow. *Wind Engineering* 2012;
751 36(6): 667-686. DOI: 10.1260/0309-524X.36.6.667

- 752 [10] Bausas MD, Danao LAM. The aerodynamics of a camber-bladed vertical axis wind
753 turbine in unsteady wind. *Energy* 2015; 93: 1155-1164. DOI:
754 10.1016/j.energy.2015.09.120
- 755 [11] Danao LA, Edwards J, Eboibi O, Howell R. A numerical investigation into the
756 influence of unsteady wind on the performance and aerodynamics of a vertical axis
757 wind turbine. *Applied Energy* 2014; 116: 111-124. DOI:
758 10.1016/j.apenergy.2013.11.045
- 759 [12] Wekesa DW, Wang C, Wei Y, Zhu E. Experimental and numerical study of turbulence
760 effect on aerodynamic performance of a small-scale vertical axis wind turbine. *Journal*
761 *of Wind Engineering and Industrial Aerodynamics* 2016; 157: 1-14. DOI:
762 10.1016/j.jweia.2016.07.018
- 763 [13] Mertens S. *Wind Energy in the Built Environment*. Multi-Science: Brentwood (UK),
764 2006.
- 765 [14] Borg M, Collu M, Brennan FP. Offshore floating vertical axis wind turbines:
766 advantages, disadvantages, and dynamics modelling state of the art. *Marine & Offshore*
767 *Renewable Energy Congress*, London (UK), 26-27 September, 2012.
- 768 [15] Brahimi M, Allet A, Paraschivoiu I. Aerodynamic analysis models for vertical-axis
769 wind turbines. *International Journal of Rotating Machinery* 1995; 2(1): 15-21. DOI:
770 10.1155/S1023621X95000169
- 771 [16] Paraschivoiu I, Delclaux F. Double Multiple Streamtube Model with Recent
772 Improvements. *Journal of Energy* 1983, 7(3), pp. 250-255.
- 773 [17] Bianchini A, Ferrari L, Carnevale EA. A model to account for the Virtual Camber
774 Effect in the Performance Prediction of an H-Darrieus VAWT Using the Momentum
775 Models. *Wind Engineering* 2011; 35(4): 465-482. DOI: 10.1260/0309-524X.35.4.465
- 776 [18] Marten D, Bianchini A, Pechlivanoglou G, Balduzzi F, Nayeri CN, Ferrara G,
777 Paschereit CO, Ferrari L. Effects of airfoil's polar data in the stall region on the
778 estimation of Darrieus wind turbines performance. *J. of Engineering for Gas Turbines*
779 *and Power* 2016; 139(2): 022606-022606-9. DOI: 10.1115/1.4034326.
- 780 [19] Marten D, Lennie M, Pechlivanoglou G, Nayeri CD, Paschereit CO. Implementation,
781 Optimization and Validation of a Nonlinear Lifting Line Free Vortex Wake Module
782 within the Wind Turbine Simulation Code QBlade. *Proc. of the ASME Turbo Expo*
783 *2015, Montréal, Canada, June 15-19, 2015*.
- 784 [20] Deglaire P. *Analytical Aerodynamic Simulation Tools for Vertical Axis Wind*
785 *Turbines*. Digital Comprehensive Summaries of Uppsala Dissertations from the Faculty
786 of Science and Technology 2010, 704, ISSN 1651-6214.
- 787 [21] Amet E, Maitre T, Pellone C, Achard JL. 2D Numerical Simulations of Blade-Vortex
788 Interaction in a Darrieus Turbine. *Journal of Fluids Engineering* 2009; 131: 111103.1-
789 111103.15. DOI: 10.1115/1.4000258
- 790 [22] Simao-Ferreira C, van Zuijlen A, Bijl H, van Bussel G, van Kuik G. Simulating
791 dynamic stall on a two-dimensional vertical-axis wind turbine: verification and
792 validation with particle image velocimetry data. *Wind Energy* 2010; 13: 1-17. DOI:
793 10.1002/we.330

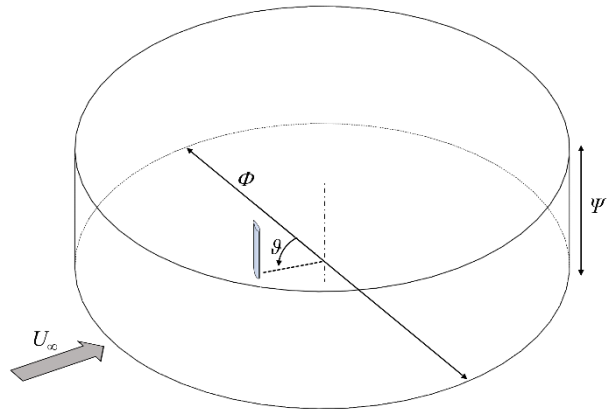
- 794 [23] Salvatore F, Bernardini M, Botti M. GPU accelerated flow solver for direct numerical
795 simulation of turbulent flows. *Journal of Computational Physics* 2013; 235: 129-142.
796 DOI: 10.1016/j.jcp.2012.10.012
- 797 [24] Raciti Castelli M, Englaro A, Benini E. The Darrieus wind turbine: Proposal for a new
798 performance prediction model based on CFD. *Energy* 2011; 36: 4919-4934. DOI:
799 10.1016/j.energy.2011.05.036
- 800 [25] Balduzzi F, Bianchini A, Maleci R, Ferrara G, Ferrari L. Critical issues in the CFD
801 simulation of Darrieus wind turbines. *Renewable Energy* 2016; 85(01): 419-435. DOI:
802 10.1016/j.renene.2015.06.048
- 803 [26] Bianchini A, Balduzzi F, Ferrara G, Ferrari L. Aerodynamics of Darrieus Wind
804 Turbines Airfoils: The Impact of Pitching Moment. *J. Eng. Gas Turbines Power*
805 2016;139(4):042602-042602-12. DOI:10.1115/1.4034940
- 806 [27] Rainbird J, Bianchini A, Balduzzi F, Peiro J, Graham JMR, Ferrara G, Ferrari L. On the
807 Influence of Virtual Camber Effect on Airfoil Polars for Use in Simulations of Darrieus
808 Wind Turbines. *Energy Conversion and Management* 2015;106:373-384. DOI:
809 10.1016/j.enconman.2015.09.053
- 810 [28] Bianchini A, Balduzzi F, Ferrara G, Ferrari L. Virtual incidence effect on rotating
811 airfoils in Darrieus wind turbines. *Energy Conversion and Management* 2016;111(1
812 March 2016):329-338. DOI: 10.1016/j.enconman.2015.12.056
- 813 [29] Bausasa MD, Danao LAM. The aerodynamics of a camber-bladed vertical axis wind
814 turbine in unsteady wind. *Energy* 2015;93(Part 1, 15 December 2015):1155–1164.
815 DOI: 10.1016/j.energy.2015.09.120
- 816 [30] Asra MT, Nezhad EZ, Mustapha F, Surjatin Wiriadidjajac. Study on start-up
817 characteristics of H-Darrieus vertical axis wind turbines comprising NACA 4-digit
818 series blade airfoils. *Energy* 2016;112(1 October 2016):528–537. DOI:
819 10.1016/j.energy.2016.06.059
- 820 [31] Zuo W, Wang X, Kang S. Numerical simulations on the wake effect of H-type vertical
821 axis wind turbines. *Energy* 2016;104(1 June 2016):295–307. DOI:
822 10.1016/j.energy.2016.02.127
- 823 [32] Howell R, Qin N, Edwards J, Durrani N. Wind tunnel and numerical study of a small
824 vertical axis wind turbine. *Renewable Energy* 2010; 35: 412-422. DOI:
825 10.1016/j.renene.2009.07.025
- 826 [33] Lam HF, Peng HY. Study of wake characteristics of a vertical axis wind turbine by
827 two- and three-dimensional computational fluid dynamics simulations. *Renewable*
828 *Energy* 2016; 90(May 2016): 386-398. DOI: 10.1016/j.renene.2016.01.011
- 829 [34] Yakhot V, Orszag SA, Thangam S, Gatski TB, Speziale CG. Development of
830 turbulence models for shear flows by a double expansion technique. *Physics of Fluids*
831 1992;4(7):1510-1525.
- 832 [35] Li Q, Maeda T, Kamada Y, Murata J, Kawabata T, Shimizu K, Ogasawara T, Nakai A,
833 Kasuya T. Wind tunnel and numerical study of a straight-bladed vertical axis wind
834 turbine in three-dimensional analysis (Part I: For predicting aerodynamic loads and
835 performance). *Energy* 2016; 106(1 July 2016):443–452. DOI:
836 10.1016/j.energy.2016.03.089

- 837 [36] Menter FR. Two-equation Turbulence-models for Engineering Applications. AIAA
838 Journal 1994; 32(8): 1598-1605. DOI: 10.2514/3.12149
- 839 [37] Gosselin R, Dumas G, Boudreau M. Parametric study of H-Darrieus vertical-axis
840 turbines using uRANS simulations. Proc. of the 21st Annual Conference of the CFD
841 Society of Canada, May 6-9, Sherbrooke (Canada), 2013
- 842 [38] Joo S, Choi H, Lee J. Aerodynamic characteristics of two-bladed H-Darrieus at various
843 solidities and rotating speeds. Energy 2015;90(Part 1 - October 2015):439–451. DOI:
844 10.1016/j.energy.2015.07.051
- 845 [39] Li Q, Maeda T, Kamada Y, Murata J, Kawabata T, Shimizu K, Ogasawara T, Nakai A,
846 Kasuya T. Wind tunnel and numerical study of a straight-bladed Vertical Axis Wind
847 Turbine in three-dimensional analysis (Part II: For predicting flow field and
848 performance). Energy 2016; 104(1 June 2016):295-307. DOI:
849 10.1016/j.energy.2016.03.129
- 850 [40] Alaimo A, Esposito A, Messineo A, Orlando C, Tumino D. 3D CFD Analysis of a
851 Vertical Axis Wind Turbine. Energies 2015; 8: 3013-3033. DOI: 10.3390/en8043013
- 852 [41] De Marco A, Coiro DP, Cucco D, Nicolosi F. A Numerical Study on a Vertical-Axis
853 Wind Turbine with Inclined Arms. International Journal of Aerospace Engineering
854 2014; 2014: 1-14. DOI: 10.1155/2014/180498
- 855 [42] Zamani M, Nazari S, Moshizi SA, Maghrebi MJ. Three dimensional simulation of J-
856 shaped Darrieus vertical axis wind turbine. Energy 2016;116(Part 1 - 1 December
857 2016):1243–1255. DOI: 10.1016/j.energy.2016.10.031
- 858 [43] Orlandi A, Collu M, Zanforlin S, Shires A. 3D URANS analysis of a vertical axis wind
859 turbine in skewed flows. Journal of Wind Engineering and Industrial Aerodynamics
860 2015; 147(December 2015): 77-84. DOI: 10.1016/j.jweia.2015.09.010
- 861 [44] Elkhoury M, Kiwata T, Aoun E. Experimental and numerical investigation of a three-
862 dimensional vertical-axis wind turbine with variable-pitch. J. Wind Eng. Ind. Aerodyn.
863 2015;139:111–123. DOI: 10.1016/j.jweia.2015.01.004
- 864 [45] Balduzzi F, Bianchini A, Ferrara G, Ferrari L. Dimensionless numbers for the
865 assessment of mesh and timestep requirements in CFD simulations of Darrieus wind
866 turbines. Energy 2016;97(15 February 2016):246-261. DOI:
867 10.1016/j.energy.2015.12.111
- 868 [46] Almohammadi KM, Ingham DB, Ma L, Pourkashan M. Computational fluid dynamics
869 (CFD) mesh independency techniques for a straight blade vertical axis wind turbine.
870 Energy 2013; 58(1 September 2013): 483-493. DOI: 10.1016/j.energy.2013.06.012
- 871 [47] Daróczy L, Janiga G, Petrasch K, Webner M, Thévenin D. Comparative analysis of
872 turbulence models for the aerodynamic simulation of H-Darrieus rotors. Energy 2015;
873 90(1 October 2015): 680-690. DOI: 10.1016/j.energy.2015.07.102
- 874 [48] Campobasso MS, Piskopakis A, Drofelnik J, Jackson A. Turbulent Navier-Stokes
875 Analysis of an Oscillating Wing in a Power Extraction Regime Using the Shear Stress
876 Transport Turbulence Model. Computers and Fluids 2013; 88: 136-155. DOI:
877 10.1016/j.compfluid.2013.08.016
- 878 [49] Drofelnik J and Campobasso MS, Comparative Turbulent Three-Dimensional Navier-
879 Stokes Hydrodynamic Analysis and Performance Assessment of Oscillating Wings for

- 880 Renewable Energy Applications, International Journal of Marine Energy, Vol. 16,
881 2016, pp. 100-115
- 882 [50] Campobasso MS, Gigante F, Drofelnik J. Turbulent Unsteady Flow Analysis of
883 Horizontal Axis Wind Turbine Airfoil Aerodynamics Based on the Harmonic Balance
884 Reynolds-Averaged Navier-Stokes Equations. ASME paper GT2014-25559, Proc. of
885 the ASME Turbo Expo 2014, Düsseldorf (Germany), 2014. DOI:10.1115/GT2014-
886 25559.
- 887 [51] Campobasso MS, Drofelnik J, Gigante F, Comparative Assessment of the Harmonic
888 Balance Navier-Stokes Technology for Horizontal and Vertical Axis Wind Turbine
889 Aerodynamics, Computers and Fluids, Vol. 136, 2016, pp. 354-370.
- 890 [52] Campobasso MS, Baba-Ahmadi MH. Analysis of Unsteady Flows Past Horizontal Axis
891 Wind Turbine Airfoils Based on Harmonic Balance Compressible Navier-Stokes
892 Equations with Low-Speed Preconditioning. ASME Journal of Turbomachinery 2012;
893 134(6): 061020-1-13. DOI: 10.1115/1.4006293.
- 894 [53] Balduzzi F, Bianchini A, Gigante FA, Ferrara G, Campobasso MS, Ferrari L.
895 Parametric and Comparative Assessment of Navier-Stokes CFD Methodologies for
896 Darrieus Wind Turbine Performance Analysis. Proc. of the ASME Turbo Expo 2015,
897 Montreal, Canada, June 15-19, 2015. DOI: 10.1115/GT2015-42663
- 898 [54] Dossena V, Persico G, Paradiso B, Battisti L, Dell'Anna S, Brighenti A, Benini E. An
899 Experimental Study of the Aerodynamics and Performance of a Vertical Axis Wind
900 Turbine in a Confined and Non-Confined Environment. Proc. of the ASME Turbo
901 Expo 2015, Montreal, Canada, June 15-19, 2015
- 902 [55] Jameson A, Baker TJ. Solution of the Euler equations for complex configurations.
903 AIAA paper 83-1929, July 1983. 6th AIAA computational fluid dynamics conference,
904 Danvers, Massachusetts.
- 905 [56] Balduzzi, F., Bianchini, A., Marten, D., Drofelnik, J., Pechlivanoglou, G., Nayeri, C.N.,
906 Ferrara, G., Paschereit, C.O., Campobasso M.S. and Ferrari, L., 2017, "Three-
907 dimensional aerodynamic analysis of a Darrieus wind turbine blade using
908 computational fluid dynamics and lifting line theory", Proc. of the ASME Turbo Expo
909 2017, Charlotte, USA, June 26-30, 2017
- 910 [57] <http://community.hartree.stfc.ac.uk/wiki/site/admin/resources.html>, last
911 10/05/2016.
- 912 [58] Abbott IH, Von Doenhoff AE. Theory of Wing Sections. New York, USA: Dover
913 Publications Inc.; 1959.

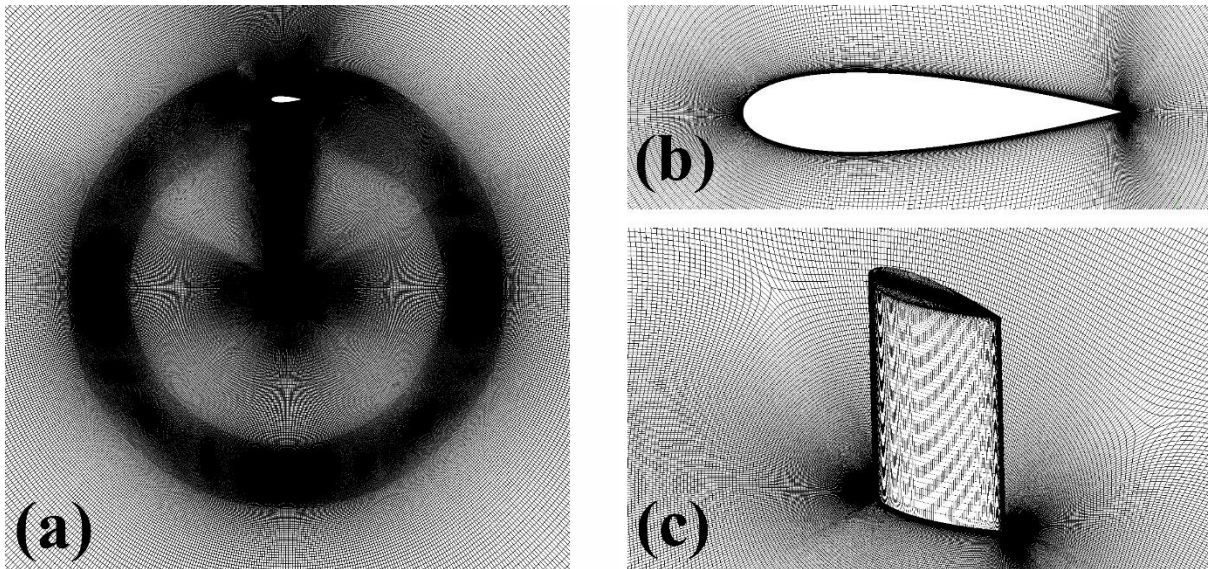
914
915

FIGURES



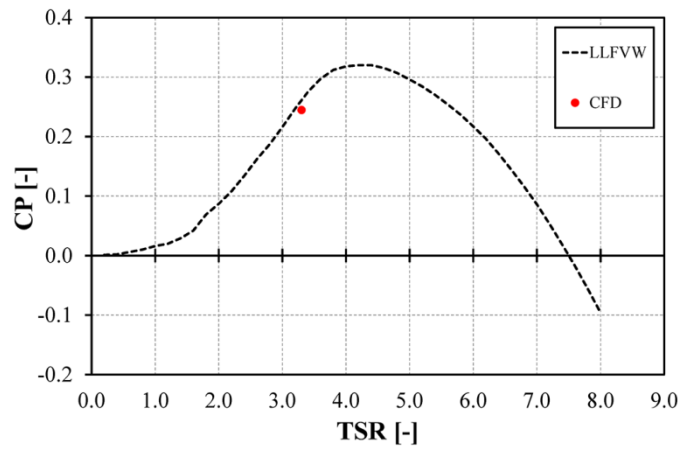
916
917
918

Figure 1 - Computational domain.



919
920
921

Figure 2 - Some details of the computational mesh.



922
923
924

Figure 3 - Attended power curve of the 1-blade model.

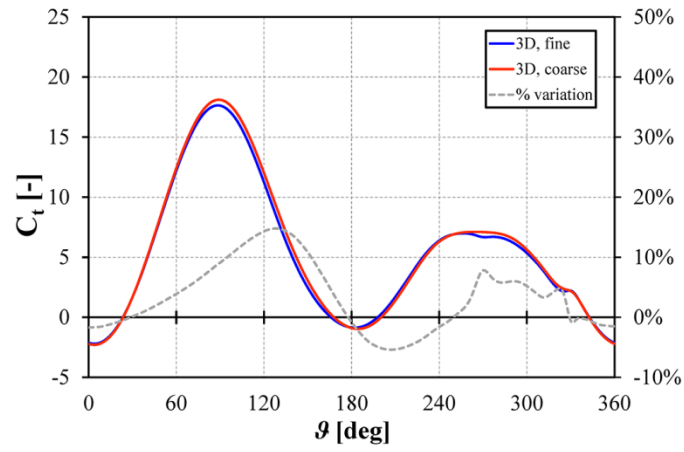


Figure 4 - Differences in the torque profile between the selected mesh and a coarser one.

925
926
927

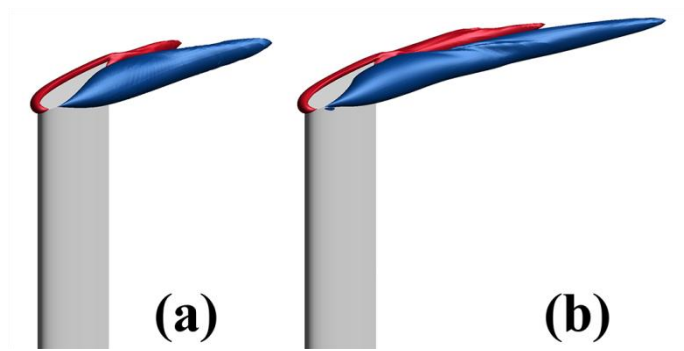
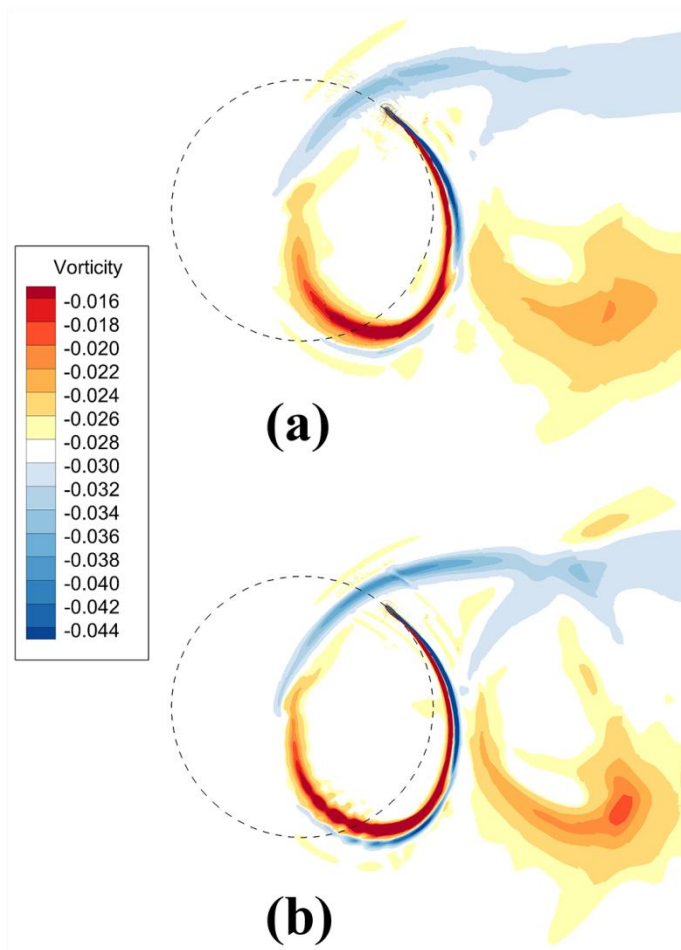


Figure 5 – Tip vortices generated at $\theta=80^\circ$: (a) coarse mesh; (b) selected mesh.

928
929
930



931
 932
 933

Figure 6 - Vorticity contours at midspan at $\beta=315^\circ$: (a) coarse mesh; (b) selected mesh.

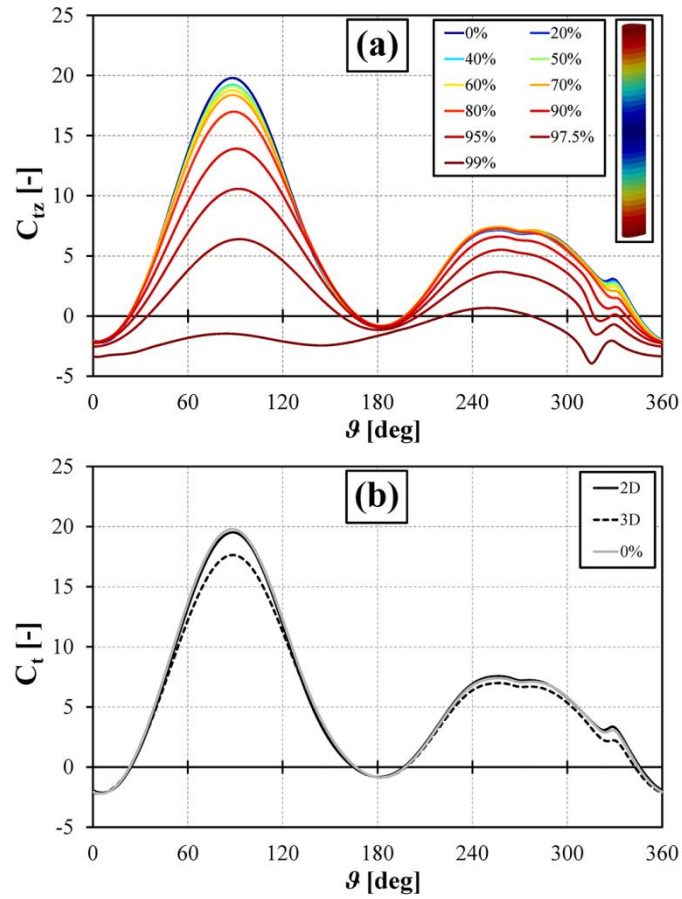


Figure 7 - Torque coefficient vs azimuthal angle: (a) variation at different span lengths; (b) 2D simulations compared to the 3D profile at midspan and average 3D profile.

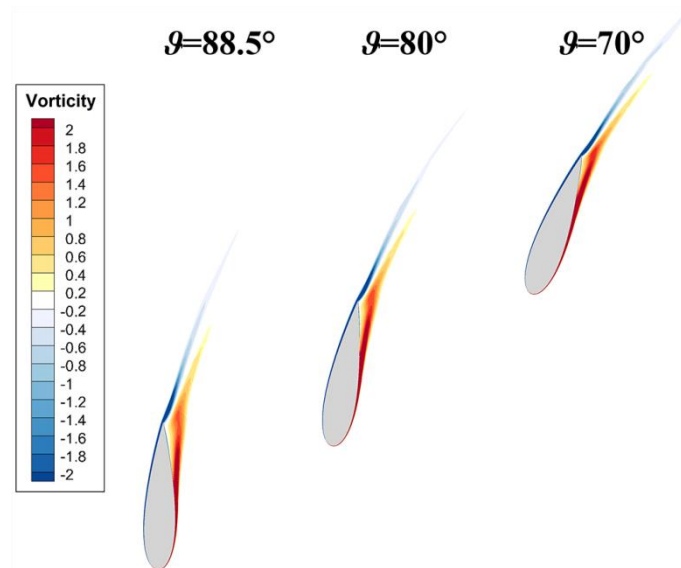
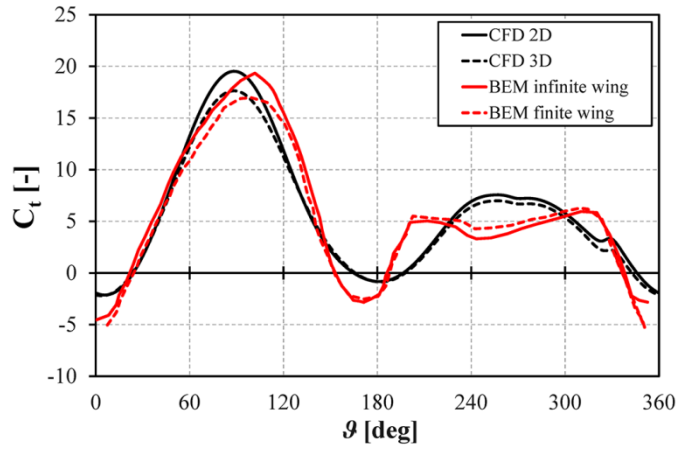


Figure 8 - Vorticity contours at midspan: $\vartheta=70^\circ$, $\vartheta=80^\circ$ and $\vartheta=88.5^\circ$.

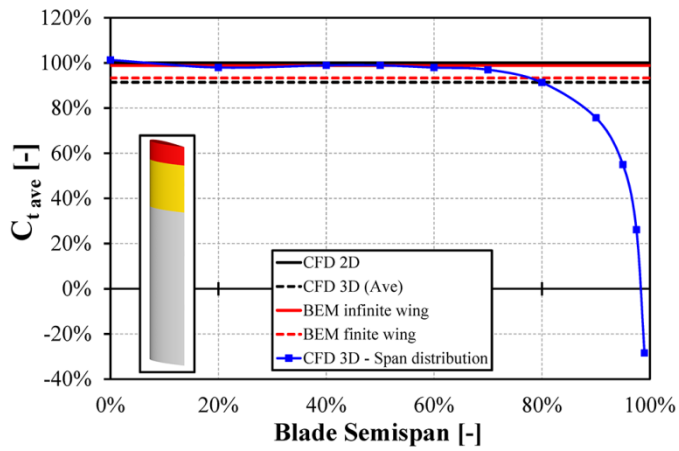
934
935
936
937

938
939
940



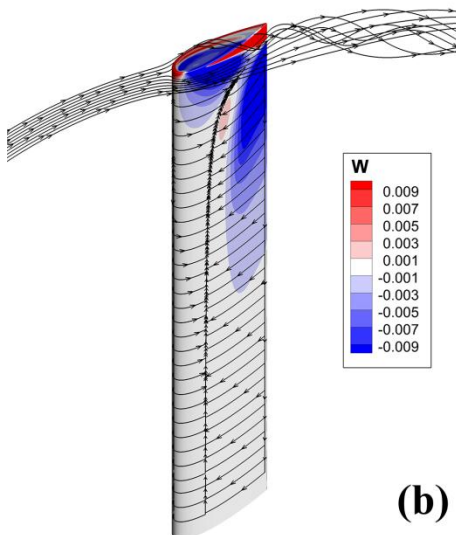
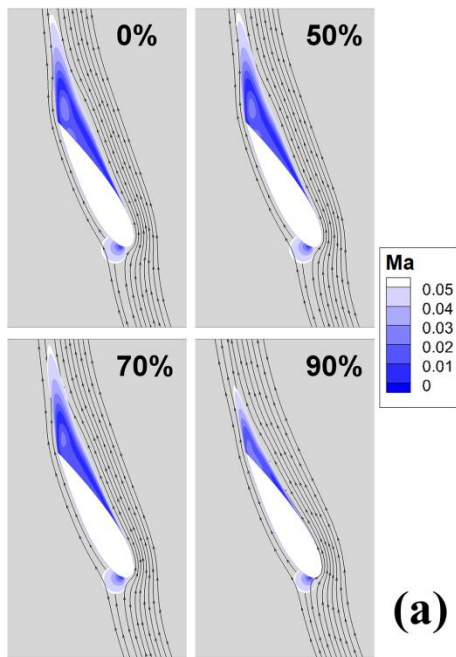
941
942
943
944

Figure 9 - Torque coefficient profiles: 2D and 3D CFD data vs. BEM simulations either including or neglecting the finite-wind effects.



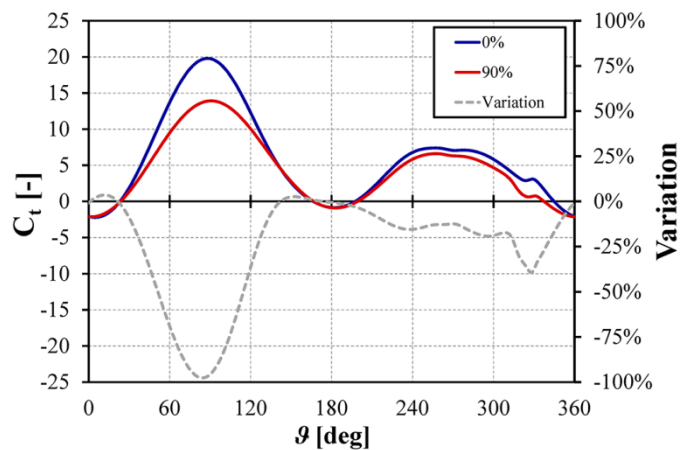
945
946
947

Figure 10 - Torque coefficient distribution along the semispan.



948
949
950
951
952

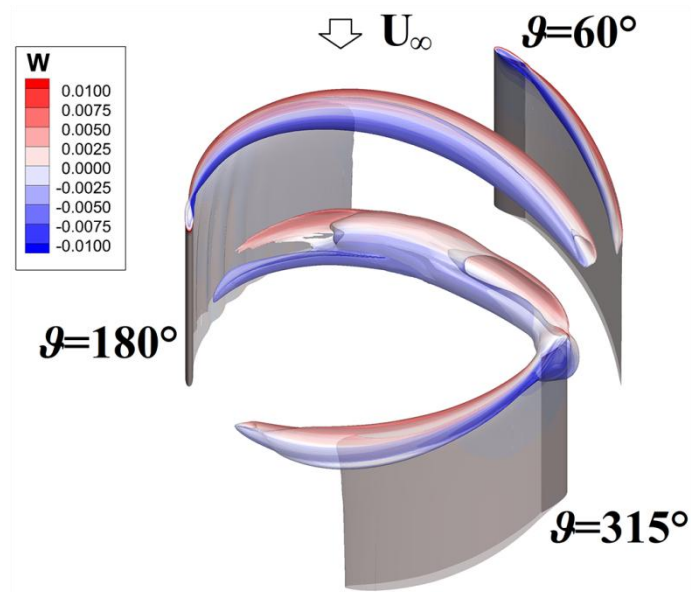
Figure 11 – Downwash effect at $\beta=120^\circ$: (a) Mach contours and streamlines at different semispan locations; (b) flow streamlines in the tip region, skin friction lines and z velocity component on the blade suction surface.



953
954

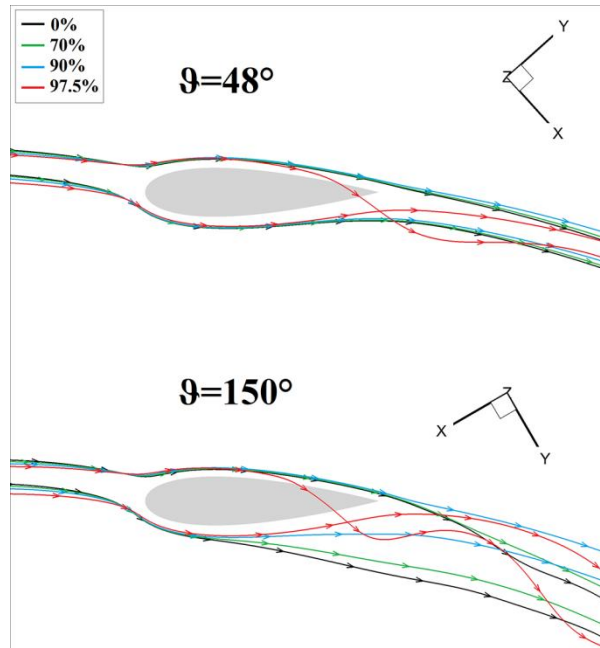
Figure 12 - Comparison of torque coefficient curves at 0 and 90 percent semispan.

955



956
957
958

Figure 13 - Isosurfaces of turbulent kinetic energy k colored with the contour of w .



959
960

Figure 14- Streamlines at different span lengths: $\vartheta=48^\circ$ and $\vartheta=150^\circ$.

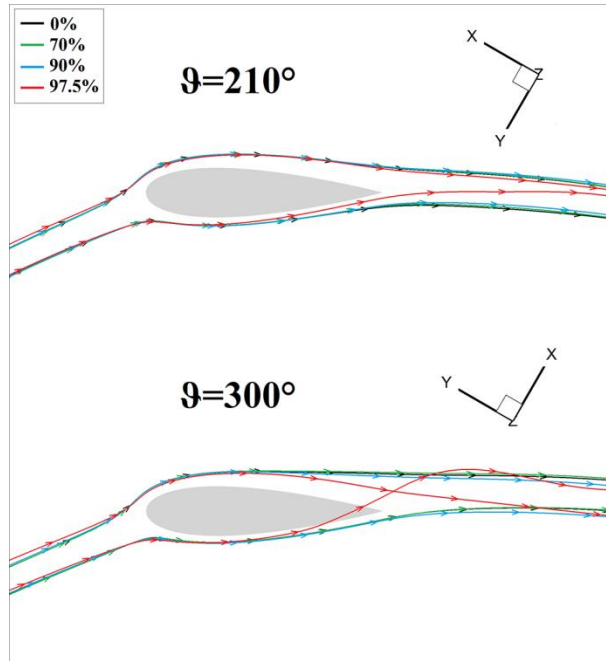


Figure 15 - Streamlines at different span lengths: $\theta = 210^\circ$ and $\theta = 300^\circ$.

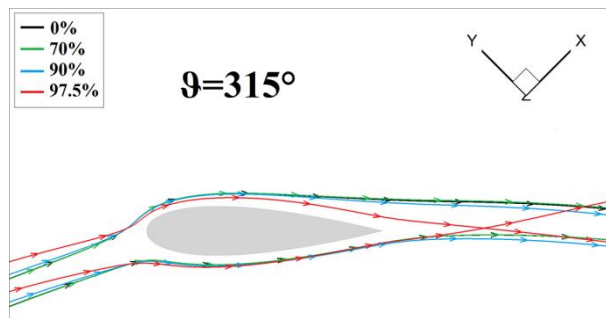


Figure 16 - Streamlines at different span lengths: $\theta = 315^\circ$.

961
962
963

964
965
966

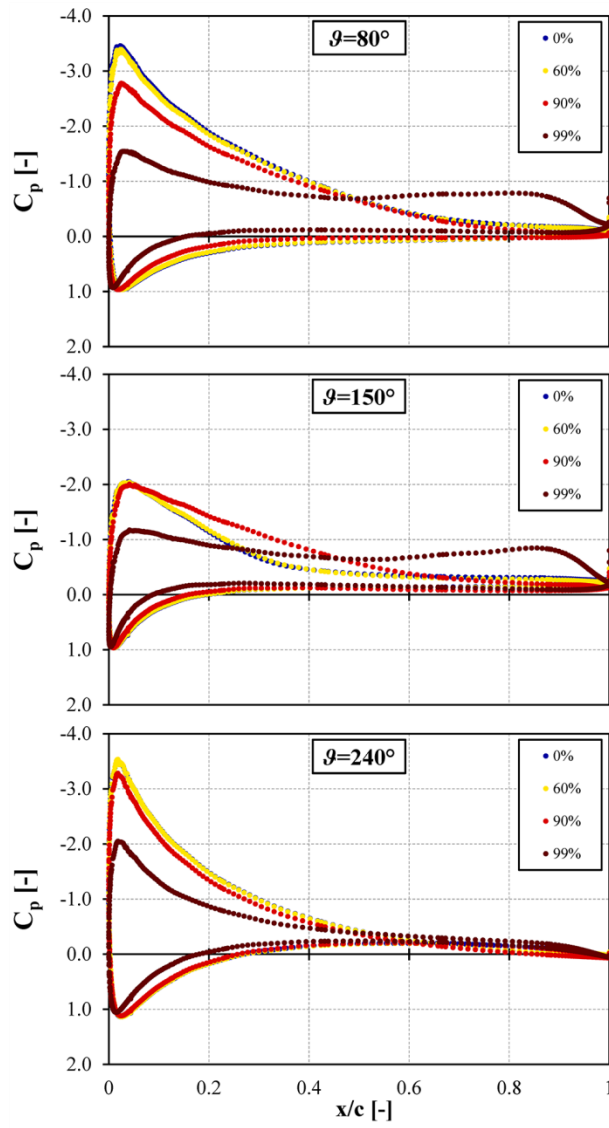


Figure 17 - Pressure coefficient profiles at different span lengths: $\theta = 80^\circ$, $\theta = 150^\circ$ and $\theta = 240^\circ$.

967
968
969

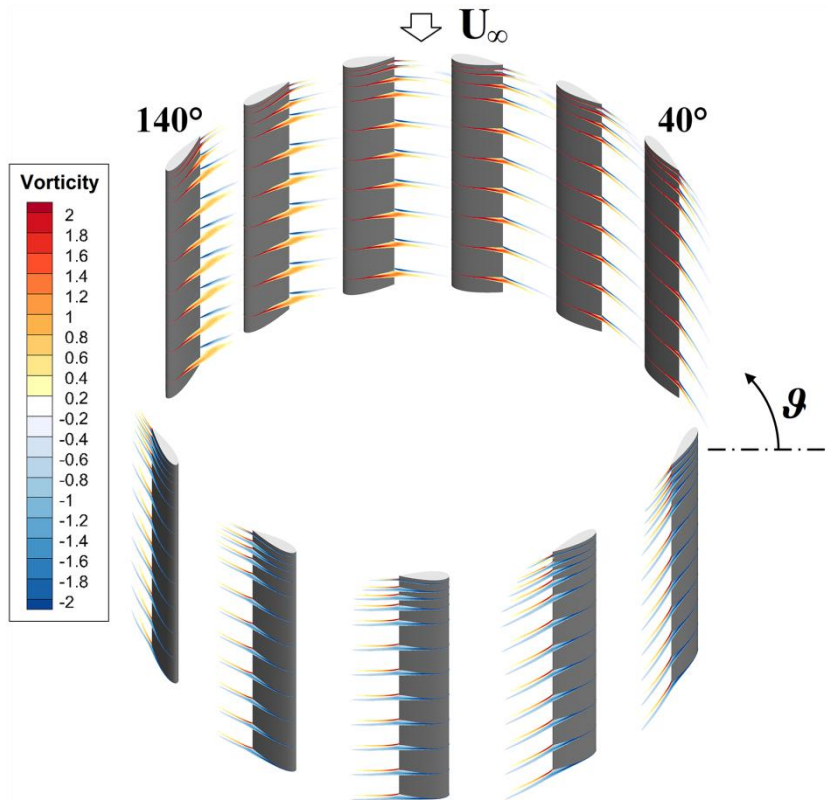
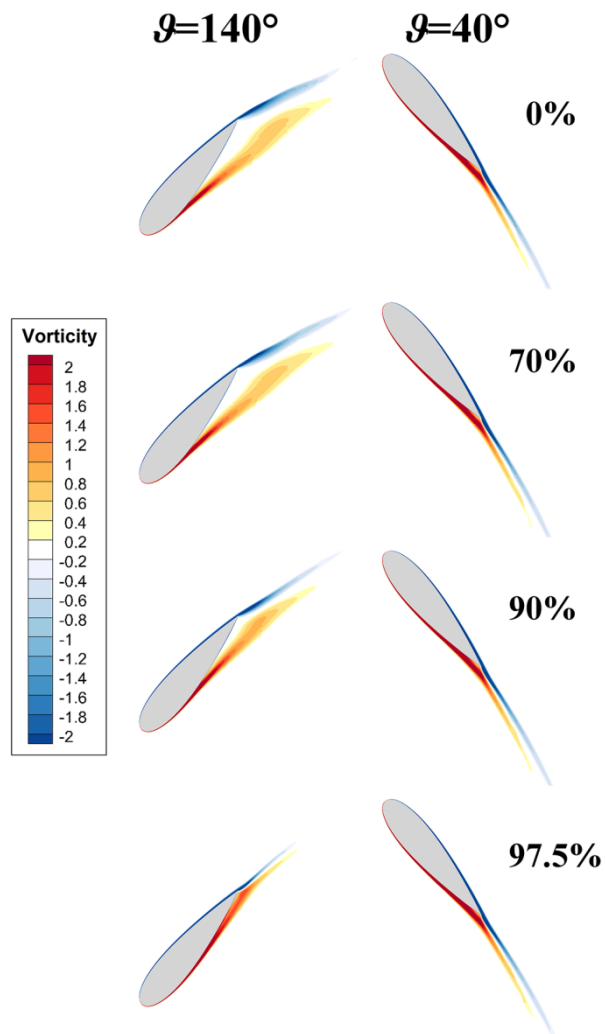


Figure 18 - Vorticity contours at different span lengths during the revolution.

970
971
972



973
974

Figure 19 - Vorticity contours at different semispan locations: $\beta=40^\circ$ and $\beta=140^\circ$.

Darrieus Wind Turbine Blade Unsteady Aerodynamics: a Three-Dimensional Navier-Stokes CFD assessment

Francesco Balduzzi¹, Jernej Drofelnik², Alessandro Bianchini¹, Giovanni Ferrara¹,
Lorenzo Ferrari^{3*}, Michele Sergio Campobasso⁴

¹ Department of Industrial Engineering, University of Florence - Via di Santa Marta 3, 50139, Firenze, Italy -
Tel. +39 055 275 8773 - Fax +39 055 275 8755 - balduzzi@vega.de.unifi.it

² School of Engineering, University of Glasgow - James Watt Building South, University Avenue, G12 8QQ
Glasgow, UK - Tel. +44 (0)141 330 2032 - j.drofelnik.1@research.gla.ac.uk

^{3*} Department of Energy, Systems, Territory and Construction Engineering, University of Pisa - Largo Lucio
Lazzarino, 56122, Pisa, Italy - Tel. +39 050 221 7132 - Fax +39 050 221 7333 - lorenzo.ferrari@unipi.it

⁴ Department of Engineering, Lancaster University - Gillow Avenue - LA1 4YW Lancaster, UK - Tel. +44
(0)1524 594673 - Fax +44 (0)1524 381707 - m.s.campobasso@lancaster.ac.uk

* = contact author

Abstract

Energized by the recent rapid progress in high-performance computing and the growing availability of large computational resources, computational fluid dynamics (CFD) is offering a cost-effective, versatile and accurate means to improve the understanding of the unsteady aerodynamics of Darrieus wind turbines, increase their efficiency and delivering more cost-effective and structurally sound designs.

In this study, a Navier-Stokes CFD research code featuring a very high parallel efficiency was used to thoroughly investigate the three-dimensional unsteady aerodynamics of a Darrieus rotor blade. Highly spatially and temporally resolved unsteady simulations were carried out using more than 16,000 processor cores on an IBM BG/Q cluster. The study aims at providing a detailed description and quantification of the main three-dimensional effects associated with the periodic motion of this turbine type, including tip losses, dynamic stall, vortex propagation and blade/wake interaction. Presented results reveal that the three-dimensional flow effects affecting Darrieus rotor blades are significantly more complex than assumed by the lower-fidelity models often used for design applications, and strongly vary during the rotor revolution. A comparison of the CFD integral estimates and the results of a blade-element momentum code is also presented to highlight strengths and weaknesses of low-fidelity codes for Darrieus turbine design.

The reported CFD results provide a valuable and reliable benchmark for the calibration of lower-fidelity models, which are still key to industrial design due to their very high execution speed.

Keywords

Darrieus wind turbine, unsteady Navier-Stokes simulations, CFD, tip flows

42 Nomenclature

43 Latin symbols

44	AoA	angle of attack	
45	AR	aspect ratio	[-]
46	c	blade chord	[m]
47	C_t	torque coefficient	[-]
48	C_p	pressure coefficient	[-]
49	CP	power coefficient	[-]
50	BEM	Blade Element Momentum	
51	CFD	Computational Fluid Dynamics	
52	H	turbine height	[m]
53	k	turbulent kinetic energy	[m ² /s ²]
54	NS	Navier-Stokes	
55	p	static pressure	[Pa]
56	PDEs	Partial Differential Equations	
57	R	turbine radius	[m]
58	RANS	Reynolds-Averaged Navier-Stokes	
59	SST	Shear Stress Transport	
60	T	torque per unit length	[Nm]
61	TSR	tip-speed ratio	[-]
62	u, v, w	Cartesian components of local fluid velocity vector	[m/s]
63	U	magnitude of absolute wind speed	[m/s]
64	\underline{v}	local fluid velocity vector	[m/s]
65	\underline{v}_b	local grid velocity vector	[m/s]
66	VAWTs	Vertical-Axis Wind Turbines	
67	W	magnitude of relative wind speed	[m/s]
68	x, y, z	reference axes	
69	y^+	dimensionless wall distance	[-]

70

71 Greek symbols

72	ϑ	azimuthal angle	[deg]
73	μ_t	turbulent viscosity	[Kg/m/s]
74	ρ	air density	[kg/Nm ³]
75	Φ	computational domain diameter	[m]
76	Ψ	computational domain height	[m]
77	ω	specific turbulence dissipation rate	[1/s]
78	Ω	turbine revolution speed	[rad/s]

79

80 Subscripts

81	∞	value at infinity	
82	ave	averaged value	

83

84 1. Introduction

85 1.1 Background

86 After most research on vertical-axis wind turbines (VAWTs) came to a standstill in the
87 mid 90's [1], the Darrieus wind turbine [2] is receiving again increasing attention of both
88 researchers and manufacturers [3-6]. For distributed wind power generation in the built
89 environment [7], inherent advantages of this turbine type, such as performance insensitivity

90 to wind direction, generator often positioned on the ground, low noise emissions [8],
91 enhanced performance in skewed [9] or highly turbulent and unsteady flows [10-12], may
92 outweigh disadvantages, such as lower power coefficients and more difficult start-up, with
93 respect to typical horizontal axis machines. Moreover, in densely populated areas VAWTs
94 are often preferred to other turbine types because they are perceived as aesthetically more
95 pleasant and thus easier to integrate in the landscape [13]. The applicability of Darrieus wind
96 turbines for utility-scale power generation making use of floating platforms also appears to
97 present important benefits in terms of overall dynamic stability [14].

98 Historically, the aerodynamic performance analysis of these rotors has been carried out
99 with low-fidelity methods, like the Blade Element Momentum (BEM) theory [1,15-17] or
100 lifting line methods [18-19]. More recently, however, the intrinsic limitations of these models
101 made clear that higher-fidelity tools are needed in order to understand in greater depth the
102 complex unsteady aerodynamics of Darrieus rotors [20], such as the interaction of the blades
103 with macro vortices [21] or dynamic stall [22].

104 While experimental testing is often quite difficult and expensive, Navier-Stokes (NS)
105 Computational Fluid Dynamics (CFD) can be a versatile and accurate means to improve the
106 understanding of VAWT unsteady aerodynamics and achieve higher-performance,
107 structurally sound and more cost-effective Darrieus turbine designs. The use of NS CFD for
108 simulating time-dependent Darrieus turbine aerodynamics is rapidly increasing due to both
109 the ongoing development and deployment of more powerful high-performance computing
110 hardware, such as large clusters of multi- and many-core processors [23], and also the
111 development of computationally more efficient algorithms.

112 113 *1.2 Previous CFD studies on Darrieus VAWTs*

114 Early use of the Reynolds-Averaged Navier-Stokes (RANS) CFD technology for
115 Darrieus rotor aerodynamics for investigating the complex fluid mechanics of these machines
116 was based mostly on two-dimensional (2D) simulations (e.g. [24]). An extensive literature
117 review of 2D RANS CFD studies is provided by Balduzzi et al. [25], along with an overview
118 of the numerical settings frequently used for Darrieus rotor RANS studies and guidelines for
119 the optimal set-up of these simulations. Two-dimensional RANS analyses, suitably corrected
120 for three-dimensional (3D) effects, such as struts resistive torque and blade tip losses, have
121 been used to estimate the turbine overall performance [26] and predominantly 2D
122 phenomena, like virtual camber [27] and virtual incidence [28] effects, the influence of
123 unsteady wind conditions on turbine aerodynamics [29], the evolution of the flow field at
124 start-up [30], and turbine/wake interactions [31].

125 However, the use of 2D simulations to analyse the flow field past real rotors may result
126 in significant uncertainties, due to the difficulty of reliably quantifying complex 3D
127 aerodynamic features such as blade tip flows, their dependence on the blade tip geometry and
128 their impact on the overall efficiency as a function of the blade aspect ratio. Moreover, most
129 3D aerodynamic features of Darrieus rotor flows vary not only spatially (e.g. dynamic stall
130 decreases from midspan to the blade tips, as shown below), but also temporally during each
131 revolution. It is difficult to develop corrections to improve the predictions of time-dependent
132 2D CFD analyses, and the resulting uncertainty on unsteady loads may severely impair both
133 aerodynamic and structural (e.g. fatigue) assessments. Therefore 3D CFD simulations are key
134 to characterizing and quantifying the aforementioned 3D aerodynamic phenomena. This is
135 important for reducing the uncertainty associated with modeling such phenomena on the basis
136 of a relatively small amount of data referring to existing turbines, and assumptions based on
137 overly simplistic analytical models. However, large computational resources are needed for
138 such simulations, due to the high temporal and spatial grid refinement needed for accurately
139 resolving all design-driving aerodynamic phenomena.

140 Comparisons of 2D and 3D simulations are sometimes carried out considering test
141 cases for which experimental data are available, as in Howell et al. [32] and Lam et al. [33].
142 In [32] the use of 2D RANS CFD led to relatively poor agreement with experiments: a
143 maximum power coefficient CP of 0.371 at a tip-speed ratio (TSR) of 2.4 was predicted
144 against a measured maximum CP of 0.186 at TSR=1.85. Using 3D simulations, the
145 maximum power coefficient was instead correctly predicted, although the shape of computed
146 and measured power curves presented significant differences. The $k-\varepsilon$ re-normalization group
147 turbulence model [34] was used for all simulations, but no detailed information on the mesh
148 size was provided, except for the indication of a high dimensionless wall distance ($y^+ \approx 10$)
149 which required the use of wall functions. Also in [35] notable discrepancies between the
150 results of 2D and 3D RANS simulations were observed: the 2D simulations predicted a
151 maximum power coefficient of 0.43 at TSR=4.5 against a maximum CP of 0.27 at TSR=1.85
152 predicted by the 3D analyses. A fairly coarse grid, consisting of 2.95 million elements was
153 used for the 3D simulations of the considered two-blade rotor, and the $k-\omega$ Shear Stress
154 Transport (SST) turbulence model [36] was used.

155 Gosselin et al. [37] used 2D and 3D RANS simulations with the $k-\omega$ SST turbulence
156 model to investigate the dependence of 3D effects on the blade aspect ratio, finding that an
157 aspect ratio of 7 led to a relative efficiency drop of 60 percent with respect to the 2D analysis.
158 Although the simulations were performed with very refined meshes (up to 700 nodes on each
159 airfoil), the article reports that no rigorous mesh-independence was obtained. Joo et al. [38]
160 analysed the aerodynamic characteristics of a two-blade rotor as a function of design
161 parameters such as solidity and optimal TSR using the 3D RANS model coupled to a
162 realizable $k-\varepsilon$ turbulence model. They used a computational mesh of 1.2 million elements
163 and compared their baseline results with available experimental data: a general
164 overestimation of the power curve was noticed, with a 10% discrepancy at the peak power.
165 Moreover, significant shape differences of computed and measured power curves were
166 observed, particularly in the right branch of such curves (i.e. for high TSR values), with the
167 measured curve being steeper than the computed one. A two-blade Darrieus rotor with
168 straight blades was analysed by Li et al. [35,39] by means of wind tunnel experiments and 3D
169 RANS simulations using the $k-\omega$ SST turbulence model. Numerical results compared
170 favourably to experimental data in the left branch (i.e. low TSR values) of the power curve,
171 but CFD significantly overestimated power for higher TSR, possibly due to excessively small
172 distance between the rotor and the farfield boundaries of the physical domain (about 2 rotor
173 diameters from the rotor center). The simulations used a grid with about 5 million elements,
174 and predicted a peak power coefficient of 0.24 at TSR=2.09 whereas experiments showed a
175 peak CP of 0.18 at TSR=2.18.

176 Alaimo et al. [40] carried out a comparative study of the aerodynamic performance of
177 three-blade Darrieus rotors using straight and helical blades. For the three-blade rotors they
178 analysed, they found that blade tip vortex flows significantly reduced the rotor performance
179 and that the use of helical blades significantly reduces this power loss. The largest grids used
180 for those 3D RANS analyses had about 10 million elements, and turbulence was modelled
181 using the $k-\varepsilon$ turbulence model with wall functions to enable the use of relatively coarse grids
182 and enhance numerical stability. De Marco et al. [41] performed 3D RANS simulations to
183 analyse the influence of the geometry of the blade supporting arms on the turbine
184 performance. Using grids featuring between 4 and 18 million elements and the $k-\omega$ SST
185 model, they found that inclined and aerodynamically shaped supporting arms can
186 significantly increase the mean power coefficient. Using computational meshes with up to 12
187 million elements and the $k-\omega$ SST model, Zamani et al. [42] characterized with 3D RANS
188 simulations the impact of J-shaped blades on Darrieus rotor torque and power characteristics
189 at low and medium TSR values, finding that this blade shape significantly increases the rotor

190 performance in these regimes, resulting in improved start-up characteristics. Orlandi et al.
191 [43] used 3D RANS simulations and the $k-\omega$ SST model to study the influence of skewed
192 wind conditions on the aerodynamic characteristics of a two-blade Darrieus turbine; to limit
193 the computational burden of the 3D analyses, grids with about 10 million elements were used.

194 A recent Navier-Stokes CFD study of a three-blade Darrieus rotor using pitching blades
195 to further improve the aerodynamic performance has made use of a Large Eddy Simulation
196 [44], an approach that can yield more accurate results than the RANS method. However,
197 resolved LES analyses require computational grids far larger than those needed for grid-
198 independent RANS analyses, and this makes the use of resolved 3D LES simulations even
199 more difficult than that of grid-independent 3D RANS analyses.

200 The aforementioned 3D CFD analyses highlighted new important aerodynamic
201 phenomena, but in almost all cases limited availability of computational resources imposed
202 the use of fairly coarse spatial and temporal refinement, and this may result in uncertainty due
203 to lack of complete grid-independence of the CFD solutions. Recent parametric analyses
204 investigating the impact of several numerical parameters on the computationally less
205 demanding 2D CFD analysis of Darrieus rotors [25,45-47] showed that the analysis reliability
206 - in terms of accuracy of both performance prediction and resolution of important flow
207 structures - is tremendously affected by the quality of the meshing and time-stepping
208 strategies. These studies highlighted that the minimum temporal and spatial refinement
209 required to obtain grid-independent solutions is quite high, due to the aerodynamic
210 complexity of these unsteady flows. Because of these constraints, the computational cost of
211 reliable 3D unsteady NS analyses of Darrieus rotor flows is extremely large due to the
212 necessity of maintaining the high temporal resolution indicated by the 2D parametric studies
213 and a high level of spatial refinement both in the grid planes normal to the rotor axis and the
214 3rd direction orthogonal to such planes. Refinement in the 3rd direction is essential to reliably
215 resolving 3D flow features. For example, the parametric study of [25] showed that temporal
216 and spatial grid-independent 2D RANS analyses of a three-blade rotor require grids with at
217 least 400,000 elements. To preserve the same accuracy level in a 3D RANS simulation of the
218 same turbine (modelling only half of the rotor making use of symmetry boundary conditions
219 on the plane at rotor midspan and ensuring adequate refinement in the tip region) the mesh
220 would consist of at least 90 million elements, which is almost ten times the size of the finest
221 meshes used in the 3D RANS studies of Darrieus rotor flows published to date. Failing to
222 maintain these refinement levels may reduce the benefits achievable by using 3D RANS
223 simulations to improve Darrieus rotor design.

224

225 *1.3 Study aim*

226 In this study, the COSA RANS research code, which features a very high parallel
227 efficiency, is used to investigate in great detail the 3D flow features of a rotating Darrieus
228 rotor blade and the impact of flow three-dimensionality on power generation efficiency. More
229 specifically, the study aims at providing a highly accurate analysis of the main 3D
230 phenomena occurring during each revolution of the considered one-blade rotor, including tip
231 vortices, dynamic stall and downstream vortex propagation, and to assess the impact of these
232 phenomena on the overall performance of this rotor. The use of a single rotating blade for the
233 type of analyses reported herein is not uncommon (see for example [40]). This set-up enables
234 a better understanding of individual key fluid mechanics phenomena adversely impacting
235 loads and energy efficiency of Darrieus rotors, and this information constitutes the first
236 knowledge level required to improve the design of these machines. Follow-on studies will
237 focus on additional 3D fluid mechanic aspects resulting from the multi-blade environment
238 making use of computational resources larger than those used in the present study.

239 To maximize the analysis reliability, a time-dependent 3D simulation using very high
 240 levels of spatial and temporal refinement is carried out using a large 98,304-core IBM BG/Q
 241 cluster.

242 The presented test case is expected to be highly valuable to other research groups both
 243 to verify new CFD approaches and to calibrate lower-fidelity models (e.g. model based on
 244 lifting line theory and free vortex methods), which are key to industrial design due to their
 245 extremely low computational cost.

246 The paper is organized as follows. Section 2 presents the numerical methodology that
 247 has been followed in the study: sub-section 2.1 reports the governing equations solved by the
 248 COSA CFD code for the analysis of Darrieus rotor flows, sub-section 2.2 summarizes the
 249 main numerical features and previous work carried out with this code, and sub-section 2.3
 250 provides the main features of the case study and describes the adopted numerical set-up.
 251 Section 3 presents the main results of the 3D CFD analysis and compares them to those of the
 252 2D analysis of the same case study, to highlight the impact of 3D effects. In Section 3 the
 253 results of the RANS CFD analyses are also compared with those of the blade element
 254 momentum theory to highlight strengths and weaknesses of this engineering approach. A
 255 summary of the study and concluding remarks are finally provided in Section 4.
 256

257 2. Numerical methodology

258 2.1 Governing equations

259 The compressible NS equations are a system of 5 nonlinear partial differential
 260 equations (PDEs) expressing the conservation of mass, momentum and energy in a viscous
 261 fluid flow. Averaging these equations on the longest time-scales of turbulence yields the so-
 262 called RANS equations, which feature additional terms depending on the Reynolds stress
 263 tensor. Making use of Boussinesq approximation, this tensor has an expression similar to that
 264 of the laminar or molecular stress tensor, with the molecular viscosity replaced by a turbulent
 265 or eddy viscosity [48-49]. In the COSA CFD code, the eddy viscosity is computed by means
 266 of the two-equation k - ω SST turbulence model [36]. Thus, turbulent flows are determined by
 267 solving a system of 7 PDEs.

268 Given a moving time-dependent control volume $C(t)$ with time-dependent boundary
 269 $S(t)$, the Arbitrary Lagrangian–Eulerian integral form of the system of the time-dependent
 270 RANS and SST equations in an absolute frame of reference is:

$$271 \quad \frac{\partial}{\partial t} \left(\int_{C(t)} \mathbf{U} dC \right) + \oint_{S(t)} (\underline{\Phi}_c - \underline{\Phi}_d) \cdot d\underline{S} - \int_{C(t)} \mathbf{S} dC = 0 \quad (1)$$

272 where \mathbf{U} is the array of conservative variables defined as:

$$273 \quad \mathbf{U} = [\rho \quad \rho \underline{v}' \quad \rho E \quad \rho k \quad \rho \omega]'; \quad (2)$$

274 The symbols ρ , \underline{v} , E , k and ω denote respectively fluid density, flow velocity vector of
 275 Cartesian components (u, v, w) , total energy per unit mass, turbulent kinetic energy per unit
 276 mass and specific dissipation rate of turbulent energy, and the superscript $'$ denotes the
 277 transpose operator. The total energy is defined as $E = e + (\underline{v} \cdot \underline{v})/2 + k$, where e denotes the
 278 internal energy per unit mass; the perfect gas law is used to express the static pressure p as a
 279 function of ρ , E , k and the mean flow kinetic energy per unit mass $(\underline{v} \cdot \underline{v})/2$. The generalized
 280 convective flux vector is defined as:

$$281 \quad \underline{\Phi}_c = \underline{\mathbf{E}}_c \underline{i} + \underline{\mathbf{F}}_c \underline{j} + \underline{\mathbf{G}}_c \underline{k} - \underline{v}_b \mathbf{U} \quad (3)$$

282 where \mathbf{E}_c , \mathbf{F}_c and \mathbf{G}_c are respectively the x-, y- and z-component of $\underline{\Phi}_c$ and are given by:

$$\begin{cases}
 \mathbf{E}_c = [\rho u \quad \rho u^2 + p \quad \rho uv \quad \rho uw \quad \rho uH \quad \rho uk \quad \rho u\omega] \\
 \mathbf{F}_c = [\rho v \quad \rho uv \quad \rho v^2 + p \quad \rho vw \quad \rho vH \quad \rho vk \quad \rho v\omega] \\
 \mathbf{G}_c = [\rho w \quad \rho uw \quad \rho vw \quad \rho w^2 + p \quad \rho wH \quad \rho wk \quad \rho w\omega]
 \end{cases} \quad (4)$$

284 in which $H=E+p/\rho$ is the total enthalpy per unit mass. The vector \underline{v}_b is the velocity of the
 285 boundary S , and the flux term $-\underline{v}_b \mathbf{U}$ is its contribution of the boundary motion to the overall
 286 flux balance.

287 The expressions of the diffusive fluxes $\underline{\Phi}_c$ and the turbulent source term S appearing in
 288 Eq. (1) can be found in [48] and [50].

289

290 2.2 COSA CFD code

291 COSA is a compressible density-based finite volume code that solves the system of
 292 PDEs corresponding to Eq. (1) using structured multi-block grids. The code features a steady
 293 flow solver, a time-domain (TD) solver for the solution of general unsteady problems [48-
 294 49], and a harmonic balance solver for the rapid solution of periodic flows [50-52]. The
 295 second-order space discretization of the convective fluxes of both the RANS and the SST
 296 equations uses an upwind scheme based on Van Leer's MUSCL extrapolations and Roe's
 297 flux difference splitting. The second order discretization of all diffusive fluxes is instead
 298 based on central finite-differencing. The space-discretized RANS and SST equations are
 299 integrated in a fully-coupled fashion with an explicit solution strategy based on full
 300 approximation scheme multigrid featuring a four-stage Runge-Kutta smoother. Convergence
 301 acceleration is achieved by means of local time-stepping and implicit residual smoothing. For
 302 general time-dependent problems, the TD equations are integrated using a second order
 303 accurate dual time-stepping approach.

304 Comprehensive information on the numerical methods used by COSA and thorough
 305 validation analyses are reported in [50,52] and other references cited therein. For unsteady
 306 problems involving oscillating wings and cross-flow open rotors such as the Darrieus
 307 turbines, COSA solves the governing equations in the absolute frame of reference using
 308 body-fitted grids. In the case of Darrieus rotors in open field operation this implies that the
 309 entire computational grid rotates about the rotational axis of the turbine. The suitability of
 310 COSA for the simulation of Darrieus wind turbines has been recently assessed through
 311 comparative analyses with both commercial CFD codes and experimental data [53-54].

312

313 2.3 Case study and computational model

314 The selected case study is a one-blade H-Darrieus rotor using the NACA 0021 airfoil.
 315 The blade chord ($c=0.0858$ m), the blade length ($H=1.5$ m) and the rotor radius ($R=0.515$ m)
 316 were set equal to those used in the case-study of [24]; the blade was attached to the spoke at
 317 midchord according to the original 3-blade model of [24]. The decision of simulating a single
 318 blade was based both on physical considerations and on hardware limitations. First, a one-
 319 blade model is sufficient to investigate all the desired 3D flow structures that lead to an
 320 efficiency reduction of a finite blade. At the same time, the use of a single blade allows one to
 321 isolate and analyze fundamental aerodynamic phenomena of finite-length blade
 322 aerodynamics, removing additional aerodynamic effects due to multiple blade/wake
 323 interactions occurring in a multi-blade rotor. From a practical viewpoint, the need of ensuring
 324 an adequate level of spatial refinement both in the grid planes normal to the rotor axis and in

325 the axial direction would have required a grid with more than 100 million elements for a
326 three-blade rotor, which was beyond the resources available for this project.

327 To further reduce the computational cost of the 3D simulation, the central symmetry of
328 H-Darrieus rotors was exploited, enabling to simulate only one half of the rotor flow, thus
329 halving computational costs. Consequently, the aspect ratio (AR) of the simulated blade
330 portion is 8.74 which is half that of the actual blade. The modeled blade portion was
331 contained in a cylindrical domain (Fig. 1) of radius $\Phi=240R$, a value chosen to guarantee a
332 full development of the wake, based on the sensitivity analyses reported in [53]. The domain
333 height was set to $\Psi=2.53H$, corresponding to half the height of the wind tunnel where the
334 original 3-blade model was tested [24,54]; measured data from these tests were previously
335 used for validating the robustness of the RANS CFD methodology [26,53] also used in the
336 present study.

337 The 3D structured multi-block grid (2D and 3D views are reported in Fig. 2) was
338 obtained with the software ANSYS[®] ICEM[®] by first generating a 2D mesh past the airfoil
339 using the optimal mesh settings identified in [47,49], and then extruding this mesh in the
340 spanwise (z) direction and filling up with grid cells the volume between the blade tip and the
341 upper (circular) farfield boundary. The far-field boundary condition enforced on the lateral
342 (cylindrical) boundary and the upper boundary of the domain is based on suitable
343 combinations of one-dimensional Riemann invariants and user-given freestream data, namely
344 pressure, density and velocity components. The sub-set of these far-field data combined with
345 suitable Riemann invariants depends on whether the fluid stream enters or leaves the
346 computational domain at the considered boundary point (the code detects automatically
347 inflow and outflow points of the boundaries at each iteration). The complete definition of this
348 far-field boundary condition is provided in [55]. On the blade surface, a no-slip condition is
349 enforced. Since the equations are solved in the absolute frame of reference, this requires
350 imposing that the fluid velocity at the blade surface equals the velocity of the blade surface
351 itself at the considered wall point, where pressure and density are extrapolated from the
352 interior domain. The 2D grid section normal to the z-axis and containing the airfoil (Fig. 2(a))
353 consisted of 4.3×10^5 quadrilateral cells. The airfoil was discretized with 580 nodes and the
354 first element height was set to $5.8 \times 10^{-5}c$ to guarantee a dimensionless wall distance y^+ lower
355 than 1 throughout the revolution. As recommended in [25], a fairly high mesh refinement of
356 both leading and trailing edge regions was adopted (Fig. 2(b)), and a high refinement in the
357 airfoil region within one chord from the airfoil surface was also used to resolve the separated
358 flow regions at high angle of attack (AoA) [27]. After extrusion in the z direction, 80 grid
359 layers in the half-blade span were formed (Fig. 2(c)), with progressive grid clustering from
360 midspan to tip to ensure an accurate description of tip flows. A fairly high grid refinement
361 was also adopted in the whole tip region above the blade in order to capture the flow
362 separation and the tip vortices. The final mesh consisted of 64 million hexahedral cells.

363 The rotor flow field was computed by solving the system of governing equations
364 corresponding to Eq. (1), that is by solving the RANS and SST equations in the absolute
365 frame of reference. In such frame, the entire body-fitted grid rotates past the rotor axis, the
366 additional flux components due to the grid motion is accounted for by the term $-\underline{v}_b \mathbf{U}$
367 appearing in Eq. (3), and no sliding surface is required.

368 To keep computational costs within the limits of the available resources, only one
369 operating condition was simulated, corresponding to a tip-speed ration (TSR) of 3.3. This
370 condition corresponds to the same revolution speed already analyzed by some of the authors
371 for the 3-blade turbine in [53]. For a 1-blade rotor, this TSR corresponds to a different point
372 of the rotor power curve. The operating condition corresponding to this TSR, however, was
373 considered of particular interest also for the 1-blade rotor because, also in this case, a) it
374 corresponds to fairly high efficiency and thus a regime at which the rotor is expected to work

375 more often than at other TSRs, and b) it features several complex aerodynamic phenomena
376 (e.g. stall and strong tip vortices) posing a significant modelling challenge for the CFD
377 analysis. Figure 3 displays the power coefficient at $TSR=3.3$ evaluated with the CFD analysis
378 reported below on the expected power curve, which was calculated with a computationally
379 more affordable code based on Lifting Line Theory coupled to a free vortex wake model. The
380 model was successfully tuned on this case-study in [56] and thus it is expected to provide a
381 power curve prediction fairly consistent with the CFD analysis reported below.

382 The free-stream wind speed was $U=9.0$ m/s. The turbulence farfield boundary
383 conditions were a turbulent kinetic energy (k) based on 5% turbulence intensity and a
384 characteristic length of 0.07 m.

385 The 3D and 2D simulations reported below were performed with the time-domain
386 solver of COSA. The 3D simulation was run on an IBM BG/Q cluster [57] featuring 8,144
387 16-core nodes for a total of 98,304 cores. Exploiting the outstanding parallel efficiency of
388 COSA, the simulation could be carried out using about 16,000 cores. This required
389 partitioning the grid into 16384 blocks using in-house utilities, and this operation was
390 performed starting from a grid with fewer blocks generated with the ANSYS[®] ICEM[®] grid
391 generator. All grid blocks had identical number of cells to optimize the load balance of the
392 parallel simulation. Using a time-discretization yielding 720 steps per revolution, the
393 simulation needed 12 revolutions to achieve a fully periodic state. The flow field was
394 considered periodic once the difference between the mean torque values of the last two
395 revolutions was smaller than 0.1% of the mean torque in the revolution before the last. The
396 wall-clock time required for this 3D simulation was about 653 hours (27.2 days).

397

398 **2.4 Grid and time-step sensitivity analyses**

399 One of the key elements of this study is that the 3D calculation was carried out using a
400 high level of spatial and temporal resolution. The 3D grid used to carry out the analyses
401 reported in Section 3 was obtained by extruding in the third direction the 4.3×10^5 -element 2D
402 grid described above, and such grid was shown to provide accurate and grid-independent
403 results in [53].

404 To assess the impact of using coarser spatial and temporal refinement on the computed
405 solution, the considered flow regime was also simulated using only 360 steps per revolution
406 and a coarser 3D grid with 8 million elements, obtained from the 64million element fine grid
407 by removing every second line in all three directions.

408 The periodic profiles of the instantaneous torque coefficient C_t obtained with the coarse
409 and fine grids are compared in Fig. 4, and the definition of C_t is provided by Eq. (5), in which
410 T denotes the instantaneous torque on the entire blade, U_∞ and ρ_∞ denote respectively the far-
411 field wind speed and the air density, c is the blade chord, and H is the overall blade length.
412 The angular position $\vartheta=0^\circ$ corresponds to the blade leading edge facing the oncoming wind
413 and entering the upwind half of its revolution.

414

$$C_t = \frac{T}{\frac{1}{2} \rho_\infty U_\infty^2 c^2 H} \quad (5)$$

415 The comparison shows that differences between the two predictions occur over most
416 parts of the period, particularly around the maximum values of C_t . These discrepancies are
417 caused by differences in the prediction of strength and timing of stall on the airfoils and
418 under-resolved wakes and wake/blade interactions when using the coarse grid. The position
419 of the curve peak (maximum C_t in the upwind region of rotor trajectory) predicted by the
420 coarse grid has an error of about 3 degrees in azimuthal coordinates, leading to a shift of the

421 curve in the range between $\vartheta=90^\circ$ and $\vartheta=300^\circ$. Such discrepancies, reported in Fig. 4 also as
 422 the difference between the coarse and fine grid profiles normalized by the revolution-
 423 averaged mean torque of the fine grid (curve labeled “% variation”) result in the mean torque
 424 coefficient obtained with the coarse grid being 3.2 percent higher than that obtained with the
 425 fine grid. As discussed in the following, this difference corresponds to nearly 40 percent of
 426 the energy efficiency loss due to finite blade length effects. This highlights the importance of
 427 using a fine grid for this type of analyses.

428 The impact of the mesh refinement on the resolution of some of the 3D flow
 429 phenomena occurring during the revolution are examined in Fig. 5. This figure shows the
 430 extent of the vortices generated at the blade tip at $\vartheta=80^\circ$ predicted with the two meshes. The
 431 red and blue vortices represent the regions of ascending and descending flow, respectively.
 432 The higher dissipation of the coarse mesh leads to an under-prediction of the downstream
 433 propagation of the vortex, which is reduced from about three chords (Fig 5(b)) to less than
 434 two chords (Fig 5(a)). The coarse grid under-estimation of the tip effects contributes to the
 435 overestimation of the torque highlighted in Fig. 4. The vorticity contours at midspan when
 436 the blade is at $\vartheta=315^\circ$ are compared in Fig. 6 to assess the resolution of the free convection of
 437 vorticity in the downstream region. With the finer mesh the wake is resolved more sharply,
 438 thus fulfilling essential prerequisites for adequately resolving blade-wake interactions in the
 439 downwind part of the revolution. The under-resolution of the wake in the downwind rotor
 440 region contributes to the higher torque produced by the blade when interacting with the wake
 441 shed in the upstream trajectory. The impact of all these vortical phenomena on the rotor
 442 performance is even higher in multi-blade rotors, due to higher number of interactions (and
 443 thus energy loss events) per revolution.

444 3. Results and discussion

446 Figure 7(a) reports the instantaneous torque coefficient per unit length (C_{tz}) at different
 447 span lengths along the blade (0 percent and 100 percent correspond to midspan and tip,
 448 respectively). The instantaneous torque coefficient per unit length C_{tz} is defined by Eq. (6).
 449 Here T_z denotes the instantaneous torque per unit blade length at the considered spanwise
 450 position.

$$451 \quad C_{tz} = \frac{T_z}{\frac{1}{2} \rho_\infty U_\infty^2 c^2} \quad (6)$$

452 Figure 7(b) reports three torque profiles. The profile labelled 2D refers to the results of
 453 a 2D simulation of the same rotor, and corresponds to the “ideal” torque of a blade with
 454 infinite span, i.e. without any secondary effects at the blade tip. This 2D simulation was
 455 carried out using a mesh equal to the midspan section of the 3D fine mesh and the same
 456 numerical parameters of the 3D simulations. The torque profile labelled “0%” is the torque
 457 per unit blade length at midspan of the finite-length rotor, whereas the torque profile labelled
 458 3D is the overall torque coefficient C_t of the 3D rotor defined in Eq. (7). The result obtained
 459 by using this definition is identical to that obtained by using Eq. (5).

$$460 \quad C_t = \frac{2}{H} \int_0^{\frac{H}{2}} C_{tz} dz \quad (7)$$

461 Examination of these profiles reveals several important facts. Firstly, the ideal 2D
 462 torque and the 3D torque profiles are characterized by similar patterns, including the

463 occurrence of two relative maxima, one in the upwind the other in the downwind regions, and
464 also similar azimuthal positions of both maxima: the maximum torque in the upwind portion
465 of the revolution is located at $\vartheta \approx 88.5^\circ$ and the maximum torque in the downwind portion of
466 the revolution is located at $\vartheta \approx 257^\circ$ in both cases. This behaviour is in line with the analyses
467 of both Lam [33] and Alaimo [40], which showed that the periodic torque profiles obtained
468 with 2D and 3D simulations differ significantly for their amplitudes but have comparable
469 shapes. Figure 7(b) also highlights that the differences between the 2D torque profile and that
470 at midspan of the 3D rotor are negligible, highlighting that 3D flow effects due to tip flows
471 do not reach this position.

472 Examination of all profiles of Fig. 7(b) shows that the effects of blade finite-length
473 effects are very small when the blade loading is low, i.e. when the angle of attack is low
474 ($0^\circ < \vartheta < 40^\circ$ and $130^\circ < \vartheta < 210^\circ$): in these portions of the revolution, the 2D and both 3D curves
475 are almost superimposed. When the incidence increases, the blade load also increases and the
476 blade starts experiencing stall. Figure 8 reports the top view of the vorticity contours at
477 midspan at three azimuthal positions to examine the onset of stall in the upwind zone. At
478 $\vartheta = 70^\circ$ a small separation region forms on the suction side of the blade. At $\vartheta = 80^\circ$ the blade
479 stall has become significant, since the flow is detached from the blade. At the position of
480 torque peak a large region of the suction surface is affected by stall. Consequently, the torque
481 loss due to tip effects also increases because the strength of tip vortex flow increases with the
482 flow incidence. The same behaviour can be seen also in the downwind zones. Closer
483 inspection of the 2D and mean 3D CP curves shows that these effects are strongest in the
484 upwind region of the period, where a maximum difference of 9.7 percent between the torque
485 peaks occurs.

486 Examining the torque profiles at the spanwise positions considered in Fig. 4(a), some
487 additional observations can be made:

- 488 • The torque profiles of the blade sections at 20%, 40% and 50% semispan are almost
489 identical, indicating that at least half of the blade is characterized by a predominantly
490 2D flow with negligible impact of tip flow effects;
- 491 • The torque profiles of the blade sections at 60%, 70% and 80% show a progressive
492 reduction of the torque peak, down to -14 percent with respect to the midspan section.
493 The remainder of the torque curve is less affected, especially in the downwind zone;
- 494 • The torque profiles of the blade sections at 90%, 95% and 97.5% show that at these
495 positions, 3D effects are strong throughout the whole revolution. Notably, in the
496 regions of positive torque production, the efficiency is remarkably reduced;
- 497 • In proximity of the blade tip (99%), almost no positive contribution to the torque output
498 is given, due to the large load reduction;
- 499 • The azimuthal position of the torque peak occurs later in the cycle as one moves
500 towards the tip, with a 5° shift between the 0% and 97.5% sections. This can be
501 explained with a reduction of the incidence angle (downwash), as shown below. The
502 experiments of Li et al. [35] highlight the same trend and show that the aforementioned
503 shift is even more pronounced for a turbine with a very low aspect ratio (AR=4.5).

504 To compare the CFD prediction of the impact of finite blade effects on turbine
505 performance to that of the widespread low-fidelity BEM theory, Fig. 9 compares the 2D and
506 mean 3D torque profiles obtained with NS CFD and the corresponding estimates obtained
507 with the VARDAR research code, a state-of-the-art BEM code developed at the University of
508 Florence [6,17-18] using the ubiquitous Leicester-Prandtl model for the finite-wing
509 correction [58]. The two BEM profiles of Fig. 9 differ in that one includes tip flow corrections
510 and the other does not. Examination of these profiles shows that the reduction of the torque
511 peak in the upwind portion of the revolution predicted by the CFD analyses is in good
512 agreement with that estimated with the simplified tip flow model included in the BEM

513 theory, and the shapes of the CFD and BEM torque profiles are in a qualitatively good
514 agreement. Conversely, the patterns of the torque curves in the downwind portion of the
515 revolution predicted by the BEM and CFD analyses are significantly different, and the torque
516 reduction due to blade finite length predicted by the BEM analysis is higher than predicted by
517 CFD. This comparative analysis highlights the potential of using CFD also for further
518 improving the predictions of low-fidelity engineering tools, which are key to Darrieus rotor
519 industrial design due to their extremely small computational requirements.

520 To provide a different quantitative perspective of the impact of tip losses, Fig. 10
521 compares the CFD and BEM profiles of mean torque coefficient per unit length. For each
522 blade height the mean value is obtained by averaging the profiles of Fig. 4(a) over one
523 revolution. The figure also reports the constant mean torque values of the 2D and 3D
524 simulations for both the CFD and BEM models. All curves are normalized with respect to the
525 mean 2D torque coefficient. One sees that the mean blade performance is almost unaffected
526 by tip-effects up to approximately 70% semispan. More specifically, it is found that tip flow
527 effects adversely affect the performance of the blade for a span length of approximately $2.6c$
528 (yellow zone in Fig. 10). In terms of aggregate data, the tip effects yield a reduction of the
529 rotor torque of 8.6% with respect to the 2D calculation with virtually infinite span. This can
530 be seen as an equivalent reduction of the actual blade's height of $0.75c$ for each half blade
531 (red colored zone in Fig. 10). Such a correction factor needs to be accounted for when
532 estimating the turbine performance by means of 2D simulations.

533 The observations above are in accordance with the findings of Li et al. [35] in terms of
534 performance drop as a function of the distance from the tip. Their experiments showed that at
535 55% semispan, corresponding to a distance of $1.0c$ from the tip, the torque peak is greatly
536 reduced. At this blade height, they found a CP reduction of 40% over the midspan value at
537 $TSR=2.2$ and 60% at $TSR=2.5$, corresponding to an equivalent reduction of the actual blade's
538 height by $1.8c$ and $2.7c$, respectively. Other analyses focused on estimating the mean power
539 reduction due to finite blade length effects through comparisons of 2D and 3D CFD analyses
540 [32,33,37,40], but their results are not directly comparable with the present study due to the
541 use of different aspect ratio, rotor solidity, TSR, airfoil geometry and number blades..
542 Overall, the equivalent height reduction can vary from $0.8c$ for a NACA 0022 three-blade
543 rotor at $TSR=1.3$ [32] up to $5c$ for a NACA 0018 two-blade rotor at $TSR=4.5$ [33].

544 To investigate in greater detail the 3D phenomena accounting for energy efficiency
545 reduction, the Mach contours and streamlines at the angular position of maximum separation
546 ($\theta=120^\circ$) are examined in Fig. 11(a). Different spanwise sections are considered to analyse
547 the flow pattern alterations from midspan to the blade tip.

548 In the central portion of the blade (from midspan to about 70% semispan) the
549 streamlines are contained in planes orthogonal to the blade axis, indicating a predominantly
550 2D flow character, and a fairly large region of separated flow in the rear of the suction side.
551 Closer to the tip (90% semispan) the downwash due to the tip flow reduces the effective AoA
552 with respect to that at midspan, and the extension of the stall region is thus reduced. The skin
553 friction lines and contours of the z velocity component (w) on the blade suction surface
554 reported in Fig. 11(b) show the extension of the region affected by downwash. Near the tip,
555 the flow on the pressure side is no longer able to follow the blade profile, and travels over the
556 tip due to the pressure difference between the pressure side and the suction side. The tip
557 vortex flow is responsible for the downwash velocity component and therefore for the
558 incidence variation along the span, in accordance with the theory of finite wings [58]. It is
559 noted that the finite wing effects occurring in Darrieus rotors are more complex than those
560 encountered in fixed finite wings. This is primarily because of the flow curvature associated
561 with the circular trajectory of the blade, and also the flow nonlinearities due to dynamic stall.

562 To quantify the impact of these effects, it is convenient to examine the curves of the
563 torque coefficient per unit length at midspan and 90% semispan (Fig. 12). The percentage
564 difference between the two curves (i.e. the torque coefficient difference between the curves at
565 each azimuthal angle divided by the revolution-averaged torque coefficient at midspan) is
566 also reported to quantify the dependence of the torque variation on the azimuthal position. A
567 notable torque reduction occurs in the interval $40^\circ < \vartheta < 130^\circ$. In addition, a large and sudden
568 torque reduction occurs towards the end of the revolution, in the interval $315^\circ < \vartheta < 340^\circ$, a
569 range in which the AoA is decreasing and goes below the value yielding stall. Also, an
570 inversion in the expected trend is noticed close to $\vartheta=150^\circ$, where the tip section performs
571 better than the midspan section: the torque of the section at 90% semispan is about 10 percent
572 higher than that at midspan. According to the finite wing theory, the lift should be in fact
573 always reduced in proximity of the tip. Therefore, the inversion at $\vartheta=150^\circ$ cannot be
574 explained with this theory alone. This occurrence and the sudden torque loss of the tip section
575 towards the end of the revolution are analysed in further detail below.

576 To investigate the origin of the sudden torque reduction at the blade tip in the interval
577 $315^\circ < \vartheta < 340^\circ$, isosurfaces of the turbulent kinetic energy field at selected azimuthal positions
578 are examined in Fig. 13. The color scale is based on the intensity of the velocity component
579 along the z-axis (w). Three azimuthal positions of the blade are considered: $\vartheta=60^\circ$, $\vartheta=180^\circ$
580 and $\vartheta=315^\circ$. During the upwind half of the revolution ($\vartheta=60^\circ$) the tip vortex is strong, since
581 the vertical component of velocity is fairly high. A high turbulence region is then generated
582 from the blade tip. At $\vartheta=180^\circ$, the region of high turbulent kinetic energy corresponding to
583 the tip vortex is increased in size and length, and is still associated with large values of w .
584 This strong vortex detaches from the blade, is convected by the wind, and is re-encountered
585 by the blade at $\vartheta=315^\circ$. The blade interaction with this vortex induces a more pronounced
586 reduction of the torque with respect to the 2D case, where this effect is absent.

587 To investigate the reasons for the higher torque of the 90% section over the midspan
588 section at $\vartheta=150^\circ$, top views of the streamlines at $\vartheta=150^\circ$ and $\vartheta=48^\circ$ are examined in Fig. 14.
589 The position $\vartheta=48^\circ$ is selected because this is the other angular position of the upwind half of
590 the revolution experiencing the same AoA of $\vartheta=150^\circ$. Streamlines on both the pressure and
591 suction sides of the blade are visualized at four different span locations. At $\vartheta=48^\circ$ the
592 downwash effect is visible: moving from midspan to the tip, the incidence of the oncoming
593 flow decreases and the air stream after the trailing edge is more aligned to the airfoil chord.
594 This phenomenon is not very pronounced due to the low loading on the blade at this angular
595 position. At $\vartheta=150^\circ$, moving from midspan to the tip, the incidence of the oncoming flow is
596 progressively reduced similarly to what seen at $\vartheta=48^\circ$. However, the flow pattern on the
597 suction side of the central portion of the blade is significantly different from that at $\vartheta=48^\circ$,
598 despite the fact that the AoA is similar in the two cases. A large separation region exists at
599 $\vartheta=150^\circ$ due to stall. Due to the finite wing length, a strong modification of this flow pattern is
600 observed moving towards the tip: from 70% semispan, the flow is attached due to lower
601 downwash-induced loading and is more aligned to the airfoil chord after the trailing edge.

602 The observations above can be explained by a combined effect of downwash and
603 dynamic stall. From $\vartheta=0^\circ$ to $\vartheta=90^\circ$ the AoA increases and stall in the central blade portion
604 occurs between $\vartheta=70^\circ$ and $\vartheta=80^\circ$. The dominant effect is that of the downwash which
605 reduces the AoA to the outer portion of the blade. When the AoA reaches its maximum
606 towards $\vartheta=90^\circ$, the central portion of the blade experiences high level of stall. From $\vartheta=90^\circ$ to
607 $\vartheta=180^\circ$ the AoA decreases but the central portion of the blade remains stalled due to delay of
608 the flow in readjusting to the decreasing incidence (a distinctive feature of dynamic stall).
609 However, the outer sections of the blade remain stall-free, and this is the reason why at
610 $\vartheta=150^\circ$ the torque of the tip sections is higher than that of the midspan section, whereas the
611 opposite is observed at $\vartheta=48^\circ$.

612 Fig. 15 presents an analysis of the same type of that of Fig. 14 for the angular positions
613 $\vartheta=210^\circ$ and $\vartheta=300^\circ$. Both positions belong to the downwind portion of the rotor trajectory
614 and are characterized by a comparable AoA. However at $\vartheta=210^\circ$ the AoA is increasing
615 whereas at $\vartheta=300^\circ$ the AoA is decreasing. One notices that the streamline pattern at $\vartheta=210^\circ$ is
616 similar to that at $\vartheta=48^\circ$. At $\vartheta=300^\circ$ the streamline patterns from midspan to tip are the same
617 as those at $\vartheta=210^\circ$. The similarity of the flow patterns at these two positions is due to the fact
618 that no stall occurs in the downwind portion of the rotor trajectory.

619 Fig. 16 depicts the blade streamlines at $\vartheta=315^\circ$, the position at which the tip vortex
620 interacts with the outboard portion of the blade in its downwind trajectory, as highlighted in
621 Fig. 13. One observes a sudden deviation of the oncoming flow in the tip region with respect
622 to the flow direction at midspan. Such deviation is due to the blade-vortex interaction, which
623 prevails over the effects due to downwash.

624 All aforementioned results can be more quantitatively described by evaluating the
625 pressure coefficient (C_p) distributions and the vorticity contours along the blade. The pressure
626 coefficient used in this study is defined by Eq. (7), where p denotes the static pressure at the
627 airfoil surface. Due to the difficulty of properly defining the actual relative wind speed at
628 each blade height, the relative flow velocity w_{th} used to calculate C_p neglects the induced
629 velocity and is computed using the vectorial sum of the absolute free-stream velocity and
630 entrainment velocity ΩR .

631 Fig. 17 reports the C_p profiles at different blade heights for three key angular positions:
632 maximum loading ($\vartheta=80^\circ$), inversion of torque of midspan and tip sections ($\vartheta=150^\circ$) and
633 maximum loading in the downwind half of the revolution ($\vartheta=240^\circ$). The objective of this
634 analysis is to highlight the impact of downwash and stall at different angular positions.

$$635 \quad C_p = \frac{P - P_\infty}{\frac{1}{2} \rho_\infty w_{th}^2} \quad (7)$$

636 At $\vartheta=80^\circ$ the blade is subject to high loading (high AoA and high relative speed). The
637 top subplot of Fig. 17 confirms that, in these conditions, 3D flow effects affect almost 40
638 percent of the blade (from the tip to 60% semispan), since moving from midspan to the tip,
639 the C_p profile at 60% already shows a slight loading reduction with respect to midspan.
640 Closer to the tip, the suction side of the blade is characterized by an almost constant pressure,
641 indicating that this blade portion generates a small lift. As a result, the torque of the tip
642 sections is substantially lower than that of the midspan section, and the torque becomes
643 negative at 97.5% midspan, as shown in Fig. 7. At $\vartheta=240^\circ$ (middle subplot of Fig. 16) the
644 AoA is high but the relative speed magnitude is lower than at $\vartheta=80^\circ$. In these conditions 3D
645 flow effects affect only the last 20 percent of the semispan (i.e. from 80% semispan to tip):
646 significant differences in the C_p profiles with respect to the midspan values are observed only
647 on the last 10 percent of the blade, where the loading becomes significantly smaller than at
648 midspan. Unlike at the two angular positions just discussed, a strong flow separation due to
649 stall occurs at $\vartheta=150^\circ$ (bottom subplot of Fig. 17). This is highlighted by the pressure profiles
650 at 0% and 60% semispan, which feature a fairly shallow slope on the suction side. In this
651 circumstance, the lower AoA at the tip sections induced by the tip vortex-related downwash
652 results in the flow past such tip sections remaining attached and these sections outperforming
653 the midspan region of the blade.

654 The evolution of the vorticity contours at different blade span heights is presented in
655 Fig. 18. In the upwind half of the revolution, the two positions $\vartheta=40^\circ$ and $\vartheta=140^\circ$ are of
656 particular interest. Although at these two positions the torque profiles along the blade are
657 comparable (see Fig. 7(a) and Fig. 7(b)), the vorticity patterns and thus the flow field are
658 remarkably different. On the other hand, moving to the downwind half of the revolution, one

659 sees that the vorticity patterns around the blade are quite similar at all azimuthal positions.
660 These patterns are in line with the previous analyses of streamlines and pressure coefficient
661 profiles.

662 Figure 19 reports the top view of the vorticity contours at four different span locations
663 at the two aforementioned azimuthal positions and highlights the vorticity differences in
664 greater detail. At $\vartheta=40^\circ$ the vorticity contours are very similar, moving from midspan to tip,
665 whereas at $\vartheta=140^\circ$ the large separation region due to stall is clearly visible along a large
666 central portion of the blade.

667

668 **4. Conclusions**

669 A 3D time-accurate Reynolds-averaged Navier-Stokes CFD analysis of an aspect ratio
670 17.5 blade rotating in Darrieus-like motion has been presented. Special attention was paid to
671 the description of 3D flow effects and their impact on the energy efficiency of Darrieus rotor
672 blades. This was accomplished also by comparative analyses of 3D and 2D CFD analyses.
673 The presented 3D CFD results were obtained with a highly refined analysis using a grid with
674 64 million elements and time-marching the flow field to a periodic state using 720 time-steps
675 per revolution. A 3D mesh sensitivity analysis was also presented. The main outcomes of the
676 analysis can be summarized as follows:

- 677 a) 3D flow effects due to finite blade length reduce the mean power of the considered
678 17.5 aspect ratio blade by 8.6 percent with respect to the torque of the
679 corresponding infinite blade. Such mean torque reduction corresponds to a
680 reduction of the effective blade length of $1.5c$ ($0.75c$ for each half blade).
- 681 b) A strong interaction between the tip-vortex released in the upwind portion of the
682 blade revolution and the blade traveling in the downwind region occurs at $\vartheta=315^\circ$,
683 and this yields an additional reduction of the outboard blade sections in this region
684 of the revolution.
- 685 c) Finite blade length effects do not modify significantly the overall shape of the blade
686 torque profile over the revolution with respect to the torque profile of the
687 corresponding infinite blade;
- 688 d) For given azimuthal position, the torque profile along the blade height varies
689 substantially from midspan to tip, and the pattern of these variations strongly
690 depends on the azimuthal position; i.e. on the magnitude of the relative velocity of
691 the oncoming flow and its local angle of attack;
- 692 e) The mean torque reduction predicted by the 3D CFD analysis and that of a state-of-
693 the-art BEM analysis using tip loss corrections is comparable, but the profiles of the
694 blade torque in the downwind portion of the revolution differ significantly. The
695 reliability of BEM analyses may be improved by using 3D CFD results to develop
696 azimuthal position-dependent tip loss corrections;
- 697 f) The 3D grid sensitivity analysis highlighted that the use of a coarser grid, with size
698 comparable to those used in most 3D Darrieus studies to date, may yield uncertainty
699 levels in the prediction of tip vortex flows, blade/wake/tip vortex interactions, and
700 dynamic stall timings and strength. All these phenomena affect torque and power
701 generation. The mean power predicted by a typical coarse grid and the fine grid of
702 this study differed by more than 3 percent. and significantly larger differences are
703 expected for multi-blade rotors due to higher number of blade/wake/tip vortex
704 encounters per revolution.

705 Future work will include investigating 3D flow effects at different tip-speed ratios,
706 particularly the lower ones, at which the impact of dynamic stall is expected to be more
707 pronounced than at the considered regime, and extending this analysis to multi-blade

708 turbines, to assess in detail all aspects of wake/blade interactions. This type of high-fidelity
709 analyses provides valuable data for validating and further improving the reliability of low-
710 fidelity tools such as BEM codes and codes based on lifting line theory and free vortex
711 transport methods. Due to their extremely high execution speeds, these engineering tools are
712 of crucial importance to improving the design of future small and large Darrieus turbines.

713

714 **Acknowledgements**

715 We acknowledge use of Hartree Centre resources in this work. The STFC Hartree
716 Centre is a research collaboratory in association with IBM providing High Performance
717 Computing platforms funded by the UK's investment in e-Infrastructure. The Centre aims to
718 develop and demonstrate next generation software, optimised to take advantage of the move
719 towards exa-scale computing. Part of the reported simulations were also performed on two
720 other clusters. One is POLARIS, part of the N8 HPC facilities provided and funded by the N8
721 consortium and EPSRC (Grant No.EP/K000225/1). The Centre is co-ordinated by the
722 Universities of Leeds and Manchester. The other resource is the HEC cluster of Lancaster
723 University, which is also kindly acknowledged. Finally, thanks are due to Prof. Ennio
724 Antonio Carnevale of the Università degli Studi di Firenze for supporting this research.

725

726 **References**

- 727 [1] Paraschivoiu I. Wind turbine design with emphasis on Darrieus concept. Polytechnic
728 International Press: Montreal (Canada), 2002.
- 729 [2] Darrieus GJM. Turbine having its rotating shaft transverse to the flow of the current.
730 US Patent No.01835018, 1931.
- 731 [3] Tjiu W, Marnoto T, Mat S, Ruslan MH, Sopian K. Darrieus vertical axis wind turbine
732 for power generation I: Assessment of Darrieus VAWT configurations. *Renewable*
733 *Energy* 2015; 75(March 2015): 50-67. DOI: 10.1016/j.renene.2014.09.038
- 734 [4] Tjiu W, Marnoto T, Mat S, Ruslan MH, Sopian K. Darrieus vertical axis wind turbine
735 for power generation II: Challenges in HAWT and the opportunity of multi-megawatt
736 Darrieus VAWT development. *Renewable Energy* 2015; 75(March 2015):560-571.
737 DOI: 10.1016/j.renene.2014.10.039
- 738 [5] Bianchini A, Ferrara G, Ferrari L. Design guidelines for H-Darrieus wind turbines:
739 Optimization of the annual energy yield. *Energy Conversion and Management*
740 2015;89:690-707. DOI: 10.1016/j.enconman.2014.10.038
- 741 [6] Bianchini A, Ferrari L, Magnani S. Energy-yield-based optimization of an H-Darrieus
742 wind turbine. *Proceedings of the ASME Turbo Expo 2012, Copenhagen (Denmark),*
743 *June 11-15, 2012.* DOI: 10.1115/GT2012-69892
- 744 [7] Balduzzi F, Bianchini A, Carnevale EA, Ferrari L, Magnani S. Feasibility analysis of a
745 Darrieus vertical-axis wind turbine installation in the rooftop of a building. *Applied*
746 *Energy* 2012; 97: 921–929. DOI: 10.1016/j.apenergy.2011.12.008
- 747 [8] Mohamed MH. Aero-acoustics noise evaluation of H-rotor Darrieus wind turbines.
748 *Energy* 2014; 65(1): 596-604. DOI: 10.1016/j.energy.2013.11.031.
- 749 [9] Bianchini A, Ferrara G, Ferrari L, Magnani S. An improved model for the performance
750 estimation of an H-Darrieus wind turbine in skewed flow. *Wind Engineering* 2012;
751 36(6): 667-686. DOI: 10.1260/0309-524X.36.6.667

- 752 [10] Bausas MD, Danao LAM. The aerodynamics of a camber-bladed vertical axis wind
753 turbine in unsteady wind. *Energy* 2015; 93: 1155-1164. DOI:
754 10.1016/j.energy.2015.09.120
- 755 [11] Danao LA, Edwards J, Eboibi O, Howell R. A numerical investigation into the
756 influence of unsteady wind on the performance and aerodynamics of a vertical axis
757 wind turbine. *Applied Energy* 2014; 116: 111-124. DOI:
758 10.1016/j.apenergy.2013.11.045
- 759 [12] Wekesa DW, Wang C, Wei Y, Zhu E. Experimental and numerical study of turbulence
760 effect on aerodynamic performance of a small-scale vertical axis wind turbine. *Journal*
761 *of Wind Engineering and Industrial Aerodynamics* 2016; 157: 1-14. DOI:
762 10.1016/j.jweia.2016.07.018
- 763 [13] Mertens S. *Wind Energy in the Built Environment*. Multi-Science: Brentwood (UK),
764 2006.
- 765 [14] Borg M, Collu M, Brennan FP. Offshore floating vertical axis wind turbines:
766 advantages, disadvantages, and dynamics modelling state of the art. *Marine & Offshore*
767 *Renewable Energy Congress*, London (UK), 26-27 September, 2012.
- 768 [15] Brahimi M, Allet A, Paraschivoiu I. Aerodynamic analysis models for vertical-axis
769 wind turbines. *International Journal of Rotating Machinery* 1995; 2(1): 15-21. DOI:
770 10.1155/S1023621X95000169
- 771 [16] Paraschivoiu I, Delclaux F. Double Multiple Streamtube Model with Recent
772 Improvements. *Journal of Energy* 1983, 7(3), pp. 250-255.
- 773 [17] Bianchini A, Ferrari L, Carnevale EA. A model to account for the Virtual Camber
774 Effect in the Performance Prediction of an H-Darrieus VAWT Using the Momentum
775 Models. *Wind Engineering* 2011; 35(4): 465-482. DOI: 10.1260/0309-524X.35.4.465
- 776 [18] Marten D, Bianchini A, Pechlivanoglou G, Balduzzi F, Nayeri CN, Ferrara G,
777 Paschereit CO, Ferrari L. Effects of airfoil's polar data in the stall region on the
778 estimation of Darrieus wind turbines performance. *J. of Engineering for Gas Turbines*
779 *and Power* 2016; 139(2): 022606-022606-9. DOI: 10.1115/1.4034326.
- 780 [19] Marten D, Lennie M, Pechlivanoglou G, Nayeri CD, Paschereit CO. Implementation,
781 Optimization and Validation of a Nonlinear Lifting Line Free Vortex Wake Module
782 within the Wind Turbine Simulation Code QBlade. *Proc. of the ASME Turbo Expo*
783 *2015, Montréal, Canada, June 15-19, 2015*.
- 784 [20] Deglaire P. *Analytical Aerodynamic Simulation Tools for Vertical Axis Wind*
785 *Turbines*. Digital Comprehensive Summaries of Uppsala Dissertations from the Faculty
786 of Science and Technology 2010, 704, ISSN 1651-6214.
- 787 [21] Amet E, Maitre T, Pellone C, Achard JL. 2D Numerical Simulations of Blade-Vortex
788 Interaction in a Darrieus Turbine. *Journal of Fluids Engineering* 2009; 131: 111103.1-
789 111103.15. DOI: 10.1115/1.4000258
- 790 [22] Simao-Ferreira C, van Zuijlen A, Bijl H, van Bussel G, van Kuik G. Simulating
791 dynamic stall on a two-dimensional vertical-axis wind turbine: verification and
792 validation with particle image velocimetry data. *Wind Energy* 2010; 13: 1-17. DOI:
793 10.1002/we.330

- 794 [23] Salvatore F, Bernardini M, Botti M. GPU accelerated flow solver for direct numerical
795 simulation of turbulent flows. *Journal of Computational Physics* 2013; 235: 129-142.
796 DOI: 10.1016/j.jcp.2012.10.012
- 797 [24] Raciti Castelli M, Englaro A, Benini E. The Darrieus wind turbine: Proposal for a new
798 performance prediction model based on CFD. *Energy* 2011; 36: 4919-4934. DOI:
799 10.1016/j.energy.2011.05.036
- 800 [25] Balduzzi F, Bianchini A, Maleci R, Ferrara G, Ferrari L. Critical issues in the CFD
801 simulation of Darrieus wind turbines. *Renewable Energy* 2016; 85(01): 419-435. DOI:
802 10.1016/j.renene.2015.06.048
- 803 [26] Bianchini A, Balduzzi F, Ferrara G, Ferrari L. Aerodynamics of Darrieus Wind
804 Turbines Airfoils: The Impact of Pitching Moment. *J. Eng. Gas Turbines Power*
805 2016;139(4):042602-042602-12. DOI:10.1115/1.4034940
- 806 [27] Rainbird J, Bianchini A, Balduzzi F, Peiro J, Graham JMR, Ferrara G, Ferrari L. On the
807 Influence of Virtual Camber Effect on Airfoil Polars for Use in Simulations of Darrieus
808 Wind Turbines. *Energy Conversion and Management* 2015;106:373-384. DOI:
809 10.1016/j.enconman.2015.09.053
- 810 [28] Bianchini A, Balduzzi F, Ferrara G, Ferrari L. Virtual incidence effect on rotating
811 airfoils in Darrieus wind turbines. *Energy Conversion and Management* 2016;111(1
812 March 2016):329-338. DOI: 10.1016/j.enconman.2015.12.056
- 813 [29] Bausasa MD, Danao LAM. The aerodynamics of a camber-bladed vertical axis wind
814 turbine in unsteady wind. *Energy* 2015;93(Part 1, 15 December 2015):1155–1164.
815 DOI: 10.1016/j.energy.2015.09.120
- 816 [30] Asra MT, Nezhad EZ, Mustapha F, Surjatin Wiriadidjajac. Study on start-up
817 characteristics of H-Darrieus vertical axis wind turbines comprising NACA 4-digit
818 series blade airfoils. *Energy* 2016;112(1 October 2016):528–537. DOI:
819 10.1016/j.energy.2016.06.059
- 820 [31] Zuo W, Wang X, Kang S. Numerical simulations on the wake effect of H-type vertical
821 axis wind turbines. *Energy* 2016;104(1 June 2016):295–307. DOI:
822 10.1016/j.energy.2016.02.127
- 823 [32] Howell R, Qin N, Edwards J, Durrani N. Wind tunnel and numerical study of a small
824 vertical axis wind turbine. *Renewable Energy* 2010; 35: 412-422. DOI:
825 10.1016/j.renene.2009.07.025
- 826 [33] Lam HF, Peng HY. Study of wake characteristics of a vertical axis wind turbine by
827 two- and three-dimensional computational fluid dynamics simulations. *Renewable*
828 *Energy* 2016; 90(May 2016): 386-398. DOI: 10.1016/j.renene.2016.01.011
- 829 [34] Yakhot V, Orszag SA, Thangam S, Gatski TB, Speziale CG. Development of
830 turbulence models for shear flows by a double expansion technique. *Physics of Fluids*
831 1992;4(7):1510-1525.
- 832 [35] Li Q, Maeda T, Kamada Y, Murata J, Kawabata T, Shimizu K, Ogasawara T, Nakai A,
833 Kasuya T. Wind tunnel and numerical study of a straight-bladed vertical axis wind
834 turbine in three-dimensional analysis (Part I: For predicting aerodynamic loads and
835 performance). *Energy* 2016; 106(1 July 2016):443–452. DOI:
836 10.1016/j.energy.2016.03.089

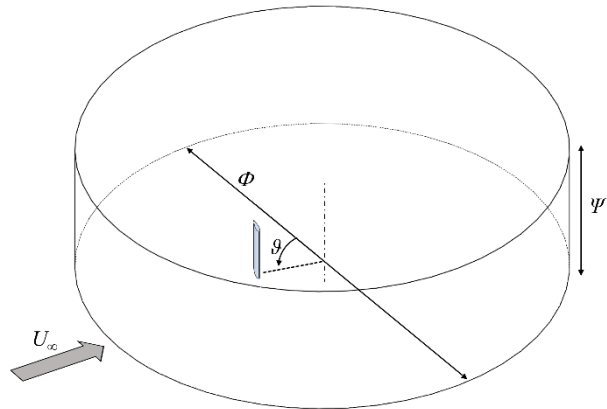
- 837 [36] Menter FR. Two-equation Turbulence-models for Engineering Applications. AIAA
838 Journal 1994; 32(8): 1598-1605. DOI: 10.2514/3.12149
- 839 [37] Gosselin R, Dumas G, Boudreau M. Parametric study of H-Darrieus vertical-axis
840 turbines using uRANS simulations. Proc. of the 21st Annual Conference of the CFD
841 Society of Canada, May 6-9, Sherbrooke (Canada), 2013
- 842 [38] Joo S, Choi H, Lee J. Aerodynamic characteristics of two-bladed H-Darrieus at various
843 solidities and rotating speeds. Energy 2015;90(Part 1 - October 2015):439–451. DOI:
844 10.1016/j.energy.2015.07.051
- 845 [39] Li Q, Maeda T, Kamada Y, Murata J, Kawabata T, Shimizu K, Ogasawara T, Nakai A,
846 Kasuya T. Wind tunnel and numerical study of a straight-bladed Vertical Axis Wind
847 Turbine in three-dimensional analysis (Part II: For predicting flow field and
848 performance). Energy 2016; 104(1 June 2016):295-307. DOI:
849 10.1016/j.energy.2016.03.129
- 850 [40] Alaimo A, Esposito A, Messineo A, Orlando C, Tumino D. 3D CFD Analysis of a
851 Vertical Axis Wind Turbine. Energies 2015; 8: 3013-3033. DOI: 10.3390/en8043013
- 852 [41] De Marco A, Coiro DP, Cucco D, Nicolosi F. A Numerical Study on a Vertical-Axis
853 Wind Turbine with Inclined Arms. International Journal of Aerospace Engineering
854 2014; 2014: 1-14. DOI: 10.1155/2014/180498
- 855 [42] Zamani M, Nazari S, Moshizi SA, Maghrebi MJ. Three dimensional simulation of J-
856 shaped Darrieus vertical axis wind turbine. Energy 2016;116(Part 1 - 1 December
857 2016):1243–1255. DOI: 10.1016/j.energy.2016.10.031
- 858 [43] Orlandi A, Collu M, Zanforlin S, Shires A. 3D URANS analysis of a vertical axis wind
859 turbine in skewed flows. Journal of Wind Engineering and Industrial Aerodynamics
860 2015; 147(December 2015): 77-84. DOI: 10.1016/j.jweia.2015.09.010
- 861 [44] Elkhoury M, Kiwata T, Aoun E. Experimental and numerical investigation of a three-
862 dimensional vertical-axis wind turbine with variable-pitch. J. Wind Eng. Ind. Aerodyn.
863 2015;139:111–123. DOI: 10.1016/j.jweia.2015.01.004
- 864 [45] Balduzzi F, Bianchini A, Ferrara G, Ferrari L. Dimensionless numbers for the
865 assessment of mesh and timestep requirements in CFD simulations of Darrieus wind
866 turbines. Energy 2016;97(15 February 2016):246-261. DOI:
867 10.1016/j.energy.2015.12.111
- 868 [46] Almohammadi KM, Ingham DB, Ma L, Pourkashan M. Computational fluid dynamics
869 (CFD) mesh independency techniques for a straight blade vertical axis wind turbine.
870 Energy 2013; 58(1 September 2013): 483-493. DOI: 10.1016/j.energy.2013.06.012
- 871 [47] Daróczy L, Janiga G, Petrasch K, Webner M, Thévenin D. Comparative analysis of
872 turbulence models for the aerodynamic simulation of H-Darrieus rotors. Energy 2015;
873 90(1 October 2015): 680-690. DOI: 10.1016/j.energy.2015.07.102
- 874 [48] Campobasso MS, Piskopakis A, Drofelnik J, Jackson A. Turbulent Navier-Stokes
875 Analysis of an Oscillating Wing in a Power Extraction Regime Using the Shear Stress
876 Transport Turbulence Model. Computers and Fluids 2013; 88: 136-155. DOI:
877 10.1016/j.compfluid.2013.08.016
- 878 [49] Drofelnik J and Campobasso MS, Comparative Turbulent Three-Dimensional Navier-
879 Stokes Hydrodynamic Analysis and Performance Assessment of Oscillating Wings for

- 880 Renewable Energy Applications, International Journal of Marine Energy, Vol. 16,
881 2016, pp. 100-115
- 882 [50] Campobasso MS, Gigante F, Drofelnik J. Turbulent Unsteady Flow Analysis of
883 Horizontal Axis Wind Turbine Airfoil Aerodynamics Based on the Harmonic Balance
884 Reynolds-Averaged Navier-Stokes Equations. ASME paper GT2014-25559, Proc. of
885 the ASME Turbo Expo 2014, Düsseldorf (Germany), 2014. DOI:10.1115/GT2014-
886 25559.
- 887 [51] Campobasso MS, Drofelnik J, Gigante F, Comparative Assessment of the Harmonic
888 Balance Navier-Stokes Technology for Horizontal and Vertical Axis Wind Turbine
889 Aerodynamics, Computers and Fluids, Vol. 136, 2016, pp. 354-370.
- 890 [52] Campobasso MS, Baba-Ahmadi MH. Analysis of Unsteady Flows Past Horizontal Axis
891 Wind Turbine Airfoils Based on Harmonic Balance Compressible Navier-Stokes
892 Equations with Low-Speed Preconditioning. ASME Journal of Turbomachinery 2012;
893 134(6): 061020-1-13. DOI: 10.1115/1.4006293.
- 894 [53] Balduzzi F, Bianchini A, Gigante FA, Ferrara G, Campobasso MS, Ferrari L.
895 Parametric and Comparative Assessment of Navier-Stokes CFD Methodologies for
896 Darrieus Wind Turbine Performance Analysis. Proc. of the ASME Turbo Expo 2015,
897 Montreal, Canada, June 15-19, 2015. DOI: 10.1115/GT2015-42663
- 898 [54] Dossena V, Persico G, Paradiso B, Battisti L, Dell'Anna S, Brighenti A, Benini E. An
899 Experimental Study of the Aerodynamics and Performance of a Vertical Axis Wind
900 Turbine in a Confined and Non-Confined Environment. Proc. of the ASME Turbo
901 Expo 2015, Montreal, Canada, June 15-19, 2015
- 902 [55] Jameson A, Baker TJ. Solution of the Euler equations for complex configurations.
903 AIAA paper 83-1929, July 1983. 6th AIAA computational fluid dynamics conference,
904 Danvers, Massachusetts.
- 905 [56] Balduzzi, F., Bianchini, A., Marten, D., Drofelnik, J., Pechlivanoglou, G., Nayeri, C.N.,
906 Ferrara, G., Paschereit, C.O., Campobasso M.S. and Ferrari, L., 2017, "Three-
907 dimensional aerodynamic analysis of a Darrieus wind turbine blade using
908 computational fluid dynamics and lifting line theory", Proc. of the ASME Turbo Expo
909 2017, Charlotte, USA, June 26-30, 2017
- 910 [57] <http://community.hartree.stfc.ac.uk/wiki/site/admin/resources.html>, last
911 10/05/2016.
- 912 [58] Abbott IH, Von Doenhoff AE. Theory of Wing Sections. New York, USA: Dover
913 Publications Inc.; 1959.

914

FIGURES

915

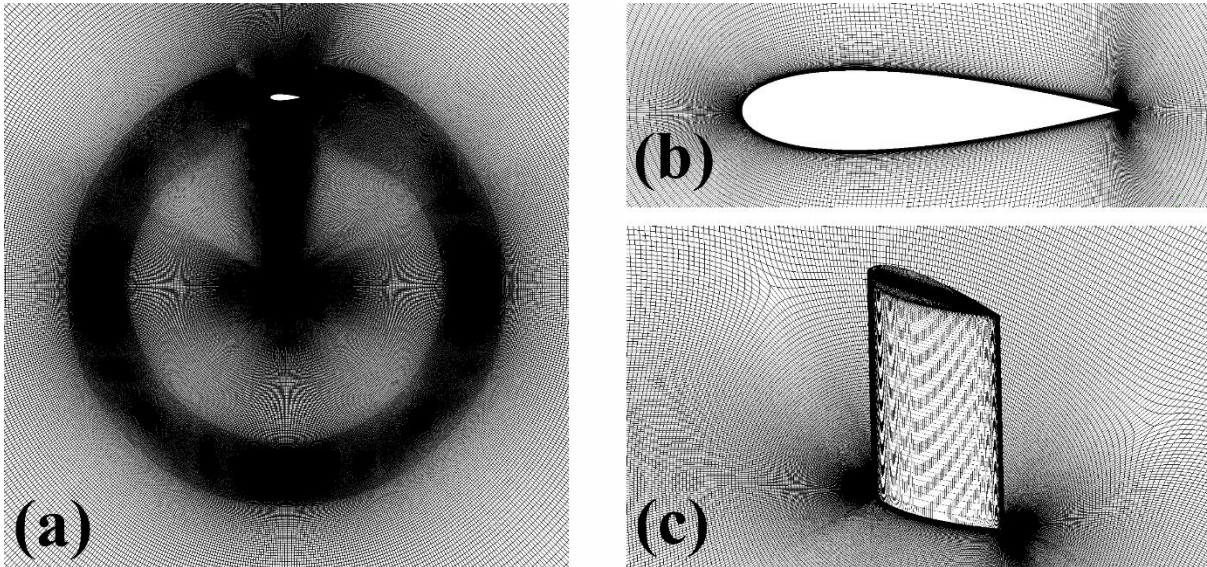


916

917

918

Figure 1 - Computational domain.

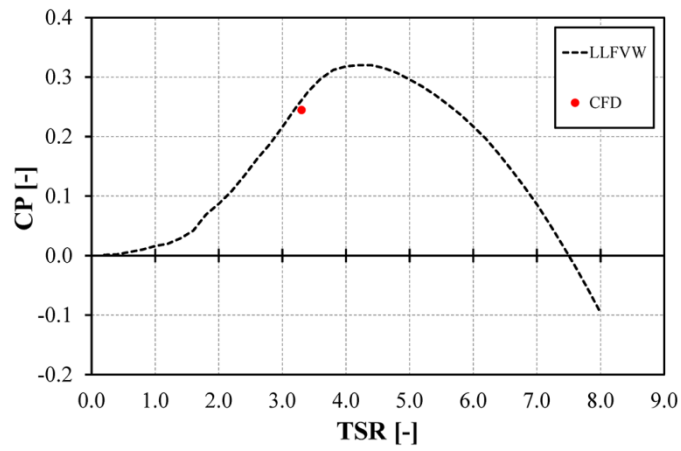


919

920

921

Figure 2 - Some details of the computational mesh.



922

923

924

Figure 3 - Attended power curve of the 1-blade model.

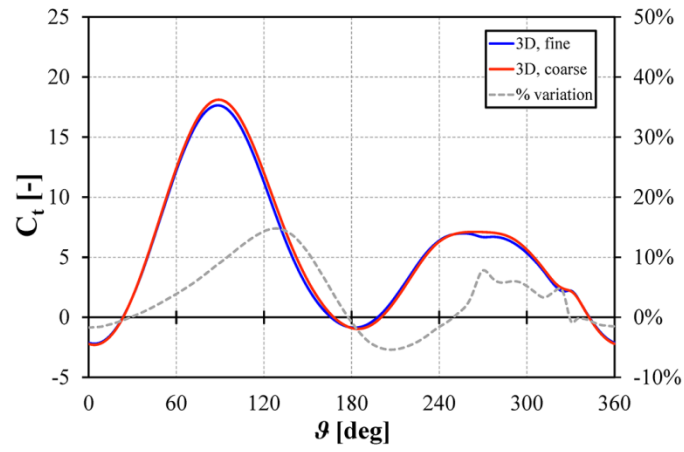


Figure 4 - Differences in the torque profile between the selected mesh and a coarser one.

925
926
927

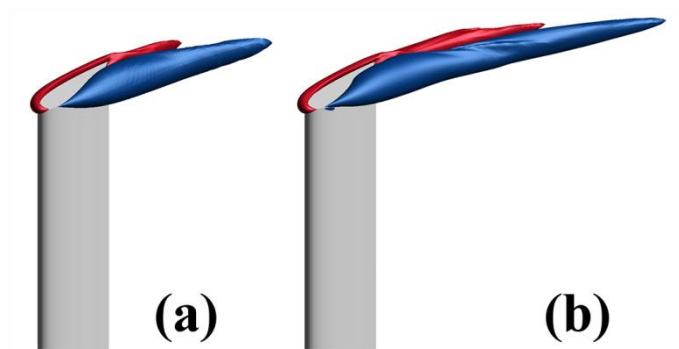
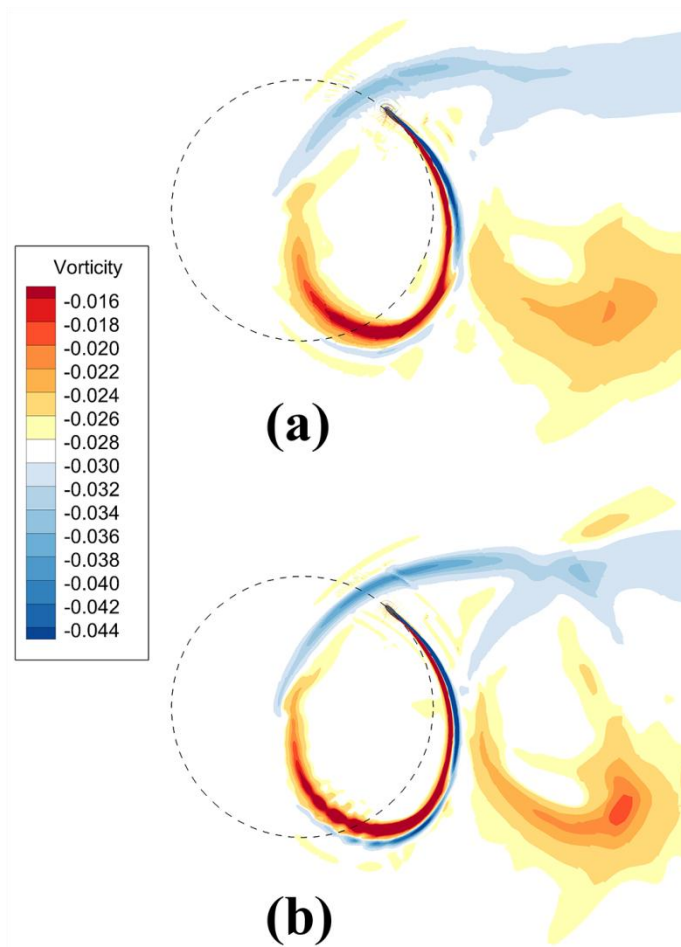


Figure 5 – Tip vortices generated at $\theta=80^\circ$: (a) coarse mesh; (b) selected mesh.

928
929
930



931
932
933

Figure 6 - Vorticity contours at midspan at $\beta=315^\circ$: (a) coarse mesh; (b) selected mesh.

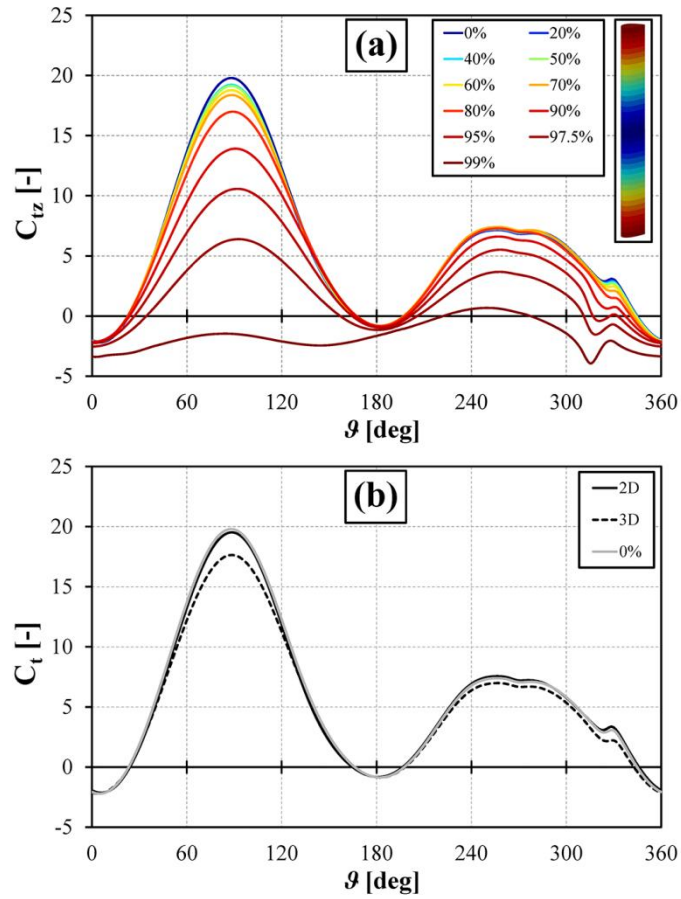


Figure 7 - Torque coefficient vs azimuthal angle: (a) variation at different span lengths; (b) 2D simulations compared to the 3D profile at midspan and average 3D profile.

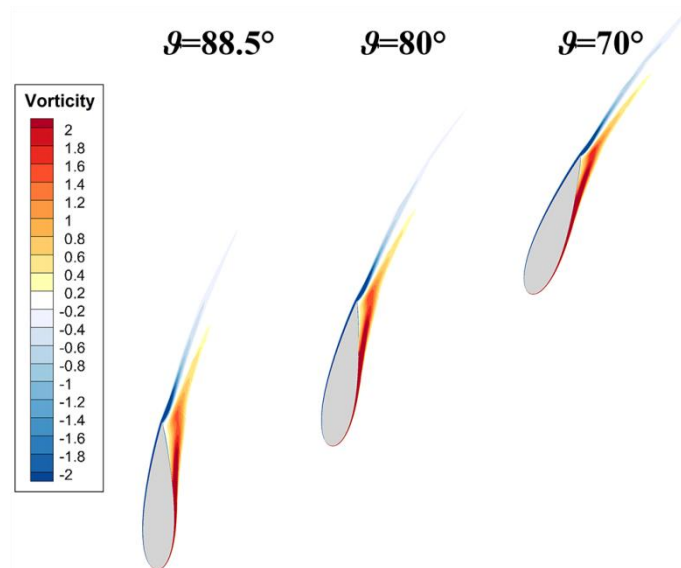
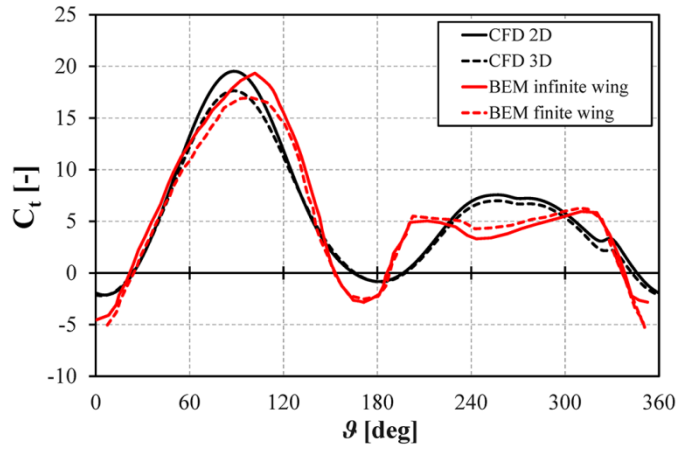


Figure 8 - Vorticity contours at midspan: $\vartheta=70^\circ$, $\vartheta=80^\circ$ and $\vartheta=88.5^\circ$.

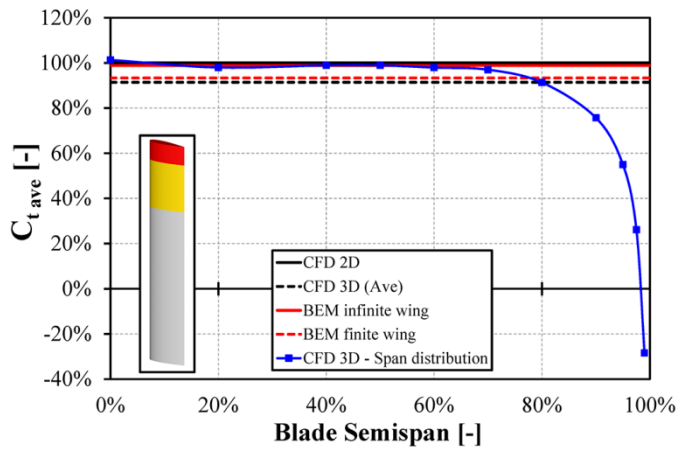
934
935
936
937

938
939
940



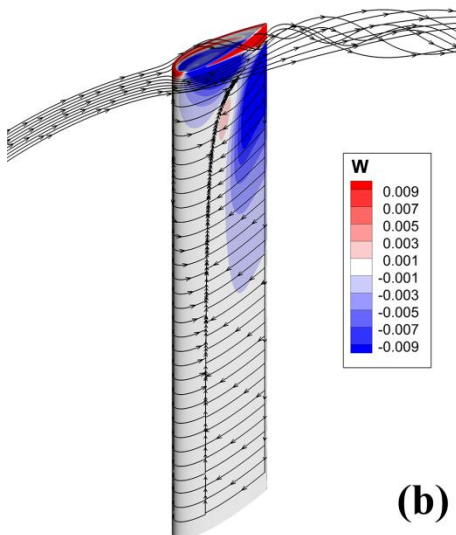
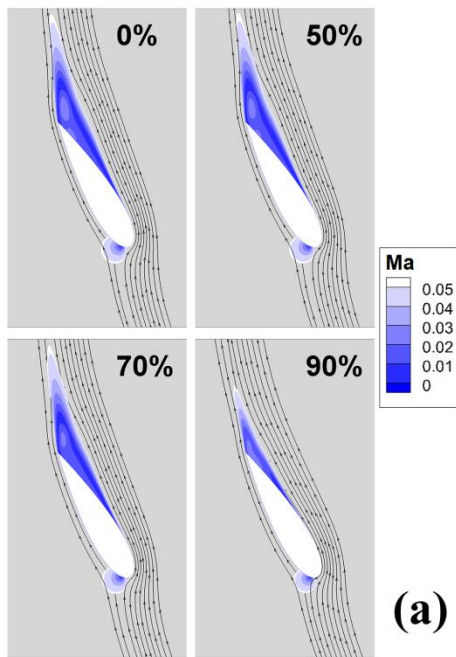
941
942
943
944

Figure 9 - Torque coefficient profiles: 2D and 3D CFD data vs. BEM simulations either including or neglecting the finite-wind effects.

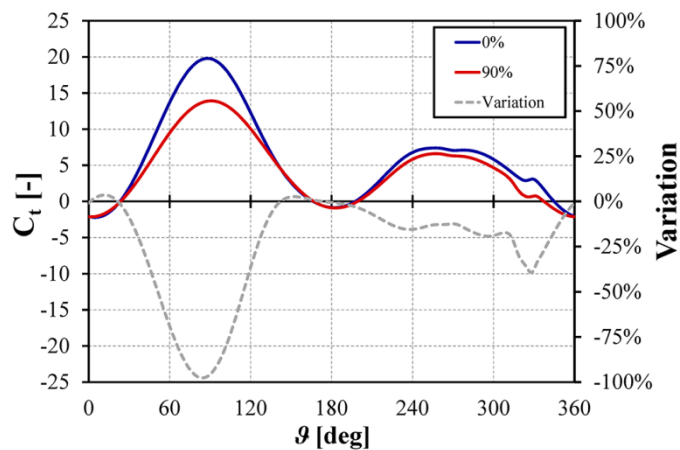


945
946
947

Figure 10 - Torque coefficient distribution along the semispan.

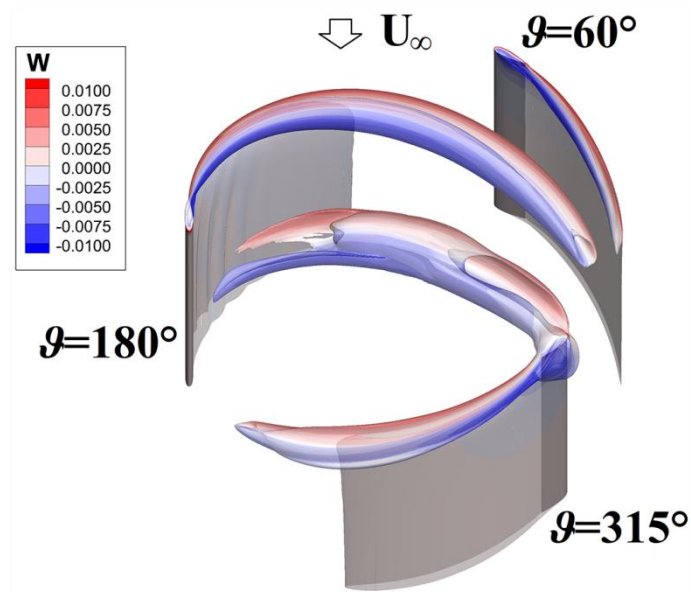


948 **Figure 11 – Downwash effect at $\beta=120^\circ$: (a) Mach contours and streamlines at different semispan**
 949 **locations; (b) flow streamlines in the tip region, skin friction lines and z velocity component on the blade**
 950 **suction surface.**
 951
 952



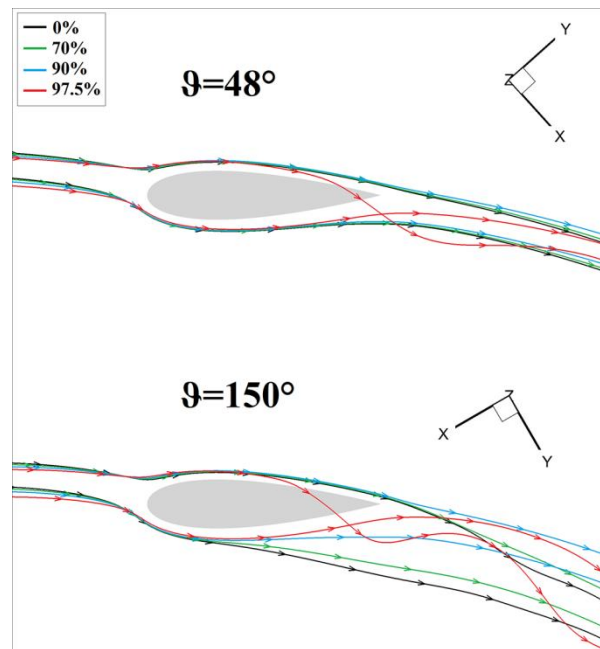
953 **Figure 12 - Comparison of torque coefficient curves at 0 and 90 percent semispan.**
 954

955



956
957
958

Figure 13 - Isosurfaces of turbulent kinetic energy k colored with the contour of w .



959
960

Figure 14- Streamlines at different span lengths: $\vartheta=48^\circ$ and $\vartheta=150^\circ$.

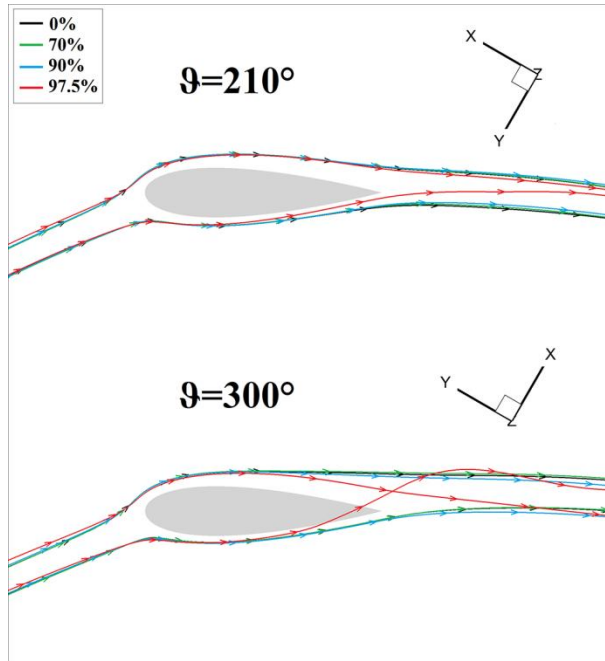


Figure 15 - Streamlines at different span lengths: $\vartheta=210^\circ$ and $\vartheta=300^\circ$.

961
962
963

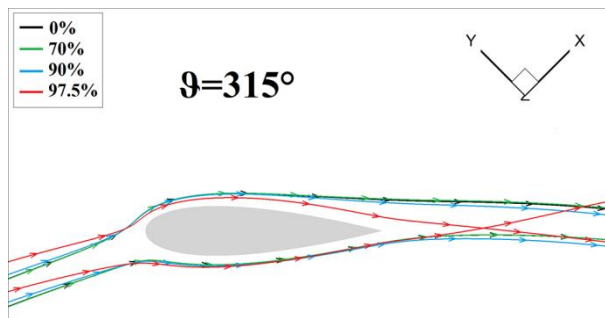


Figure 16 - Streamlines at different span lengths: $\vartheta=315^\circ$.

964
965
966

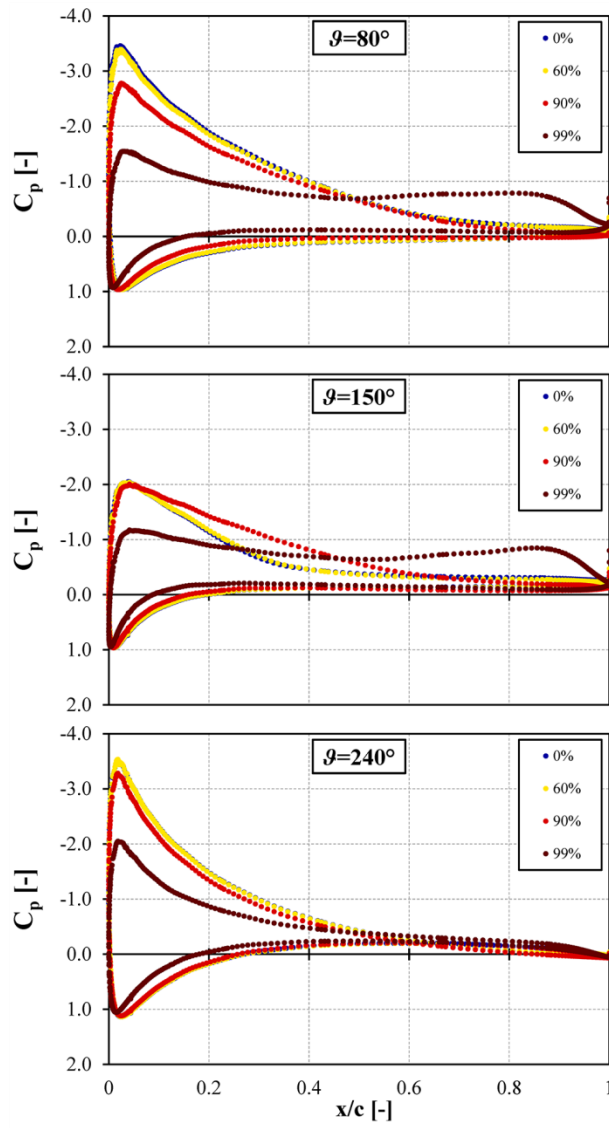


Figure 17 - Pressure coefficient profiles at different span lengths: $\vartheta=80^\circ$, $\vartheta=150^\circ$ and $\vartheta=240^\circ$.

967
968
969

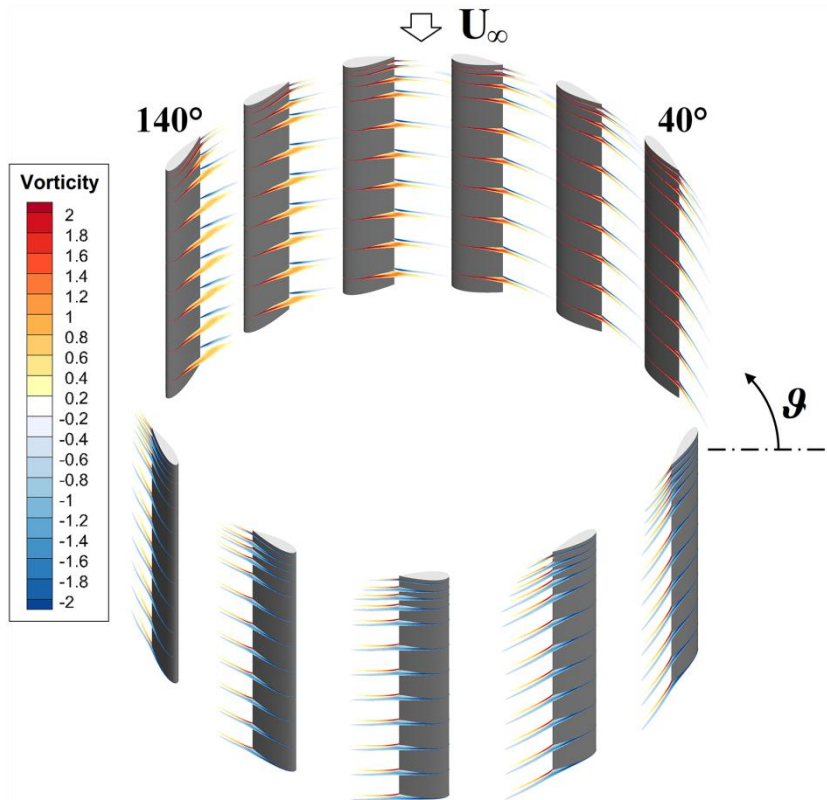
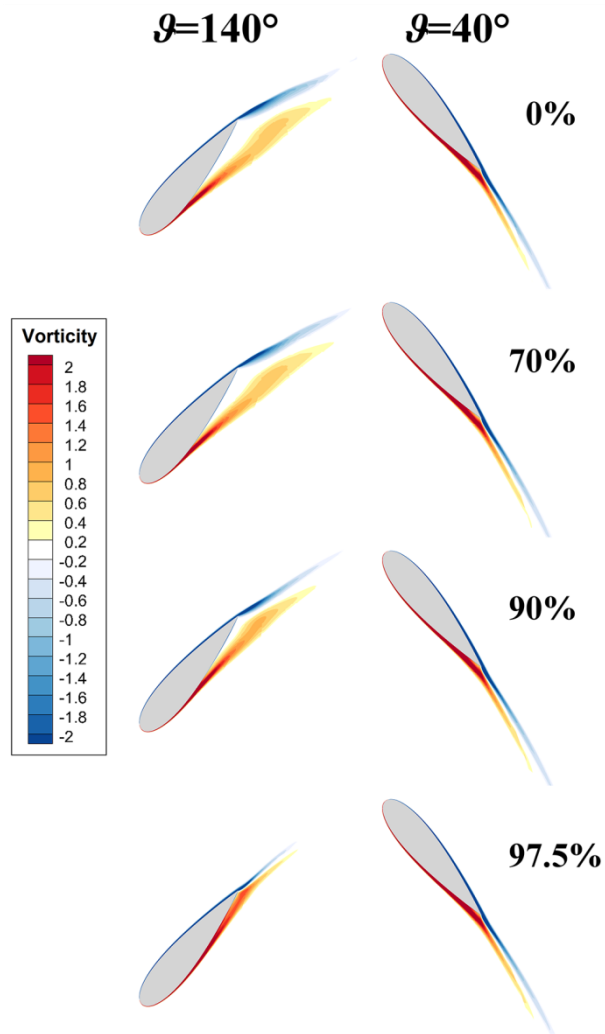


Figure 18 - Vorticity contours at different span lengths during the revolution.

970
971
972



973
974

Figure 19 - Vorticity contours at different semispan locations: $\beta=40^\circ$ and $\beta=140^\circ$.